EXPERIMENTAL INVESTIGATION OF ULTRAWIDEBAND WIRELESS

SYSTEMS: WAVEFORM GENERATION, PROPAGATION ESTIMATION, AND

DISPERSION COMPENSATION


A  Dissertation

Submitted to the Faculty

of

Purdue University

by

Amir Dezfooliyan


In Partial Fulfillment of the

Requirements for the Degree

of

Doctor of Philosophy


December 2013

Purdue University

West Lafayette, Indiana

To my family

ACKNOWLEDGMENTS

TABLE OF CONTENTS

# LIST OF TABLES

LIST OF FIGURES

ABSTRACT

Dezfooliyan, Amir. Ph. D., Purdue University, December 2013. Experimental Investigation of Ultrawideband Wireless Systems: Waveform Generation, Propagation Estimation, and Dispersion Compensation. Major Professor: Andrew M. Weiner.

Ultrawideband (UWB) is an emerging technology for the future high-speed wireless communication systems. Although this technology offers several unique advantages like robustness to fading, large channel capacity and strong anti-jamming ability, there are a number of practical challenges which are topics of current research. One key challenge is the increased multipath dispersion which results because of the fine temporal resolution. The received response consists of different components, which have certain delays and attenuations due to the paths they took in their propagation from the transmitter to the receiver. Although such challenges have been investigated to some extent, they have not been fully explored in connection with sophisticated transmit beamforming techniques in realistic multipath environments.

The work presented here spans three main aspects of UWB systems including waveform generation, propagation estimation, and dispersion compensation. We assess the accuracy of the measured impulse responses extracted from the spread spectrum channel sounding over a frequency band spanning 2-12 GHz. Based on the measured responses, different transmit beamforming techniques are investigated to achieve high-speed data transmission in rich multipath channels. We extend our work to multiple antenna systems and implement the first experimental test-bed to investigate practical challenges such as imperfect channel estimation or coherency between the multiple transmitters over the full UWB band. Finally, we introduce a new microwave photonic arbitrary waveform generation technique to demonstrate the first optical-wireless transmitter system for both characterizing channel dispersion and generating predistorted waveforms to achieve spatio-temporal focusing through the multipath channels.

# 1. INTRODUCTION

Ultrawideband (UWB) is an emerging technology for short range, high speed wireless communication which has gained great interest from academia and industry especially in the past 10 years [1]. Historically, UWB has been used as a military tool for radar, sensing and communications. In 2002, the Federal Communications Commission (FCC) in the United States issued new frequency regulations that allow UWB for different applications such as radar and radio communications. They allocated 7.5 GHz spectrum band between 3.1 and 10.6 GHz for UWB communications [2]. Due to the large frequency bandwidth, UWB systems have several unique advantages over the conventional narrow band systems which can be listed as:

- *High data rates:* This is perhaps the most compelling benefit of the UWB systems. The capacity of a given radio frequency (RF) link grows linearly with increasing bandwidth [3]. UWB radio technique can support data rate transmissions which cannot be offered by the narrow band systems [4].

- *Multipath immunity and fading robustness:* Temporal resolution of the UWB systems, which is inversely proportional to the bandwidth of the transmitted signals, is extraordinary fine. This provides the capability to resolve most of the multipath components (MPCs) incident at the receiver. Large frequency bandwidth also offers a huge inherent frequency diversity which makes UWB systems immune to multipath fading.

- *High precision for location and ranging applications:* UWB systems have good temporal resolutions which potentially allow sub-centimeter resolutions in ranging applications such as rescue operation or mining industry [5].

- *Potentially low complexity:* UWB systems offers low complexity advantage due to their baseband nature which excludes the necessity of RF mixing stage which was required for narrow band systems [1] .

Although UWB offers several unique advantages for the future high-speed communication systems, there are a number of practical challenges which are topics of current research. One key challenge is the increased multipath dispersion which results because of the fine temporal resolution. The received response consists of different components, which have certain delays and attenuations due to the paths they took in their propagation from the transmitter to the receiver, Fig 1.1. Unless compensated, multipath distortion can severely limit data rate in a communication system. Although such effects have been investigated to some extent, they have not been fully explored in connection with sophisticated transmit beamforming techniques in realistic multipath environments.

Another key challenge is the generation and distribution of ultrawide waveforms due to the restricted RF bandwidth available from current electronic equipment. Despite the advancement of technology in electronic arbitrary waveform generators (AWG), generation of arbitrary waveforms over the whole UWB band still is a challenge. Before 2007, electronic AWGs were mainly limited to the frequencies bellow 3 GHz which are completely out of the 3.1-10.6 GHz band. As a result, majority of the previous UWB
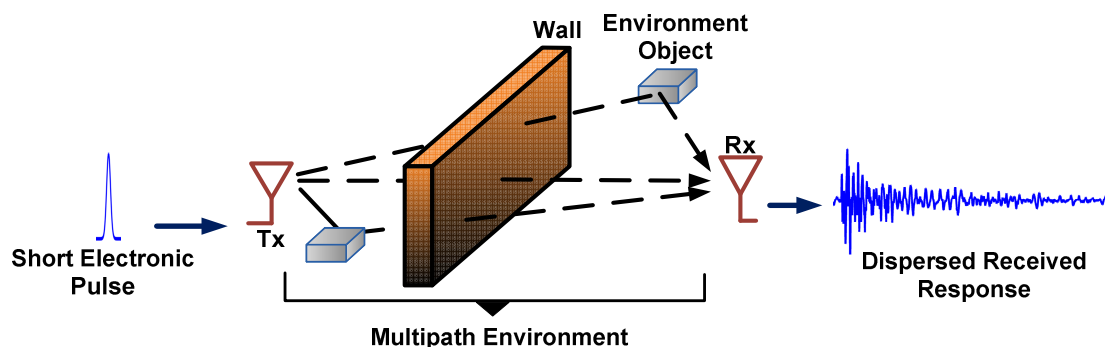


Fig. 1.1: Multipath in ultrawideband wireless systems. The transmitted signals from the transmitter (Tx) reach the receivers via different sets of scattering paths. As a result, the received responses from a short pulse excitation consist of a large multiplicity of multipath components.

works are based on simulations which do not address the practical challenges. A few other researchers who have experimentally studied UWB communication systems either cover a small portion of the 3.1-10.6 GHz [6, 7] or are completely of this band [8, 9].

The lack of comprehensive experimental measurement over UWB channels has motivated us to conduct a series of experimental studies on UWB channels. This dissertation covers numerous aspects including UWB waveform generation, propagation estimation, multipath suppression and data communication.

## 1.1 Organization of the Dissertation with Summary of our Contributions

Characterizing the wideband propagation channel is important for radio system design and performance analysis in general, and characterization of UWB channels in particular is a topic of current research. Chapter 2 covers spread spectrum sounding experiments for indoor wireless channel over a frequency band spanning 2-12 GHz, which exceeds the full FCC UWB band. Experiments were carried out for directional spiral antennas in line-of-sight (LOS) and omni-directional biconical antennas in non-line-of-sight (NLOS) environments, in the latter case with up to 15 m antenna separation. For biconical antennas, channel multipath dispersion is the main reason for the delay spreads, while for spirals, frequency-dependent delays of the antennas modify signals upon radiation and reception. A special emphasis of this chapter is to assess the accuracy of the measured impulse responses extracted from the received waveforms by deconvolution in a typical indoor environment. In one scheme to assess accuracy, impulse responses obtained using different spread spectrum waveforms are compared; independent measurements show excellent agreement, with correlation coefficients about 0.99. In a second assessment approach, accuracy is tested by performing time reversal experiments based on the measured channel impulse response. Correlation coefficients between experimental and theoretical time-reversal traces are on the order of 0.98, which further confirms highly accurate measurements.

In chapter 3, we employ the spread spectrum channel sounding to investigate and compare impulse response (IR) and time reversal (TR) beamforming characteristics for omni-directional biconical and directional spiral antennas over realistic indoor

ultrawideband channels in both LOS and NLOS environments. We discuss the effects of channel multipath dispersion and antenna frequency-dependant delay distortions on the received responses in both time and frequency domains. The effectiveness of TR for waveform compression is characterized by computing root mean square delay spread and peak-to-average power ratio. Our study suggests that the effectiveness of time reversal is subject to a trade-off between competing effects – namely, compensation of spectral phase variation (which leads to compression) and aggravation of spectral amplitude structure (which opposes compression). Although TR is a powerful technique for compensation of phase distortions associated with broadband frequency-independent antennas (as shown in LOS experiments with spiral antennas), it shows only modest performance in compressing time spread associated with multipath delays.

In chapter 4, we introduce Phase Compensation (PC) beamforming as a solution to suppress multipath distortion in UWB systems, a topic which to the best of our knowledge has not been studied in the literature on UWB communications. Our emphasis is to assess the capabilities of PC compared to TR over single-input single-output UWB channels regarding multipath suppression, channel hardening, noise sensitivity and high-speed data transmission. Experiments were carried out for PC and TR prefilters in both LOS and NLOS environments. The multipath compression effectiveness is characterized by computing the root mean square delay spread and peak-to-average power ratio for actual measured channels and for the IEEE 802.15.4(a) UWB model. Our study suggests PC outperforms TR considerably in mitigating the multipath channel dispersion. Bit-Error-Rate (BER) curves have been simulated for data rates in the range of 125-4000 Mbps based on the measured channel responses. The BER simulations suggest that while the TR performance is prohibitively saturated by its residual intersymbol interference for data rates of 500 Mbps and above (especially in NLOS), PC can be used for high-speed data transmissions as fast as 2 Gbps in both LOS and NLOS environments.

In chapter 5, we extend our work to multiple antenna systems and introduce an experimental setup to study transmit beamforming over multiple-input single-output configurations. This setup can be used to investigate practical issues which are not usually addressed in simulation models, such as imperfect channel estimation, coherency

between the multiple transmitters, or unwanted antenna couplings. Our implementation is based on the use of optical delay lines to apply appropriate time shifts to the output of an electrical AWG. We assess the experimental accuracy of our setup over a 4×1 MISO system using time reversal beamforming.

In chapter 6, in contrast to the previous chapters in which electronic devices were used to synthesize arbitrary RF waveforms, we generate the required UWB signals using photonic approaches. Photonic AWG provides several unique opportunities such as ultra-broad bandwidth and cost-efficiency compared to the electronic devices. We introduce a new RF photonic AWG method which removes previous restrictions and achieves high fidelity waveforms with radically increased time bandwidth product. The unprecedented instantaneous RF bandwidth available from our technique offers potentials for new horizons in areas such as chirped radar, high-speed covert wireless, and RF sensing. We employ our proposed technique to demonstrate space-time compression of ultrabroadband wireless signals over a three octave frequency range of 2 to 18 GHz through dispersive antennas and highly scattering multipath channels. To the best of our knowledge, this is the first experimental report that explores an RF-photonic transmitter to both characterize channel dispersions in real wireless environments and generate predistorted waveforms to achieve focusing through the multipath channels.

Finally, in chapter 7, we summarize our work and present future research directions.

# 2. EVALUATION OF TIME DOMAIN PROPAGATION MEASUREMENTS OF UWB SYSTEMS USING SPREAD SPECTRUM CHANNEL SOUNDING

## 2.1. Introduction

Characterizing the wideband propagation channel is important for radio system design and performance analysis in general, and characterization of ultrawideband channels in particular, is a topic of current interest [10]. UWB comes with several unique advantages (i.e. multipath fading robustness [11], and ultra high range resolution for radar applications [12]), and understanding the propagation channel is prerequisite to evaluating any UWB system.

In general, there are two possible methods for wideband channel sounding and propagation measurements: frequency domain and time domain. Frequency domain measurements rely on the utilization of a Vector Network Analyzer (VNA) which controls a synthesized frequency sweeper. The sweeper excites the channel by sinusoidal waveforms at different frequencies and records the frequency dependent S-parameter $S_{12}(f)$, which provides an estimate of the channel transfer function $H(f)$. The impulse response $h(t)$ can be calculated by taking Inverse Fourier Transform of $H(f)$. While the frequency domain approach can be used to characterize channel responses over a large bandwidth, the sweep time of the VNA ranges typically from several seconds to several minutes, depending on many factors like measurement bandwidth, speed of the synthesizer, and bandwidth of the IF filter [13, 14]. Although this suffices for time invariant channels in which the transmitter and the receiver are static, the sweep time of a VNA is too slow to handle fast time variant channels [10]. Another drawback is that complete channel characterization requires measurements of phase as well as magnitude, which in turn necessitates simultaneous connection of the VNA to both the transmitter

(Tx) and the receiver (Rx). Usually this requires a high quality doubly shielded RF cable which is a major limitation for long distance measurements. In one recent example, Pagani and Pajusco [15] used a VNA to cover the full 3.1-10.6GHz UWB band in LOS as well as NLOS environments up to 20m of Tx-Rx separation. Most other examples report measurements at less than 10m of antenna separation or cover less than the full FCC UWB band [16, 17].

Time domain measurements provide a more direct characterization approach. In the simplest case, channels are excited by a short pulse and impulse responses are sampled at the receiver end by an oscilloscope. The chief limitation of this technique is that generating ultrashort, low ringing pulses with sufficient power to measure high attenuation channels is difficult. Received responses in this method are the convolution of a channel response and a probing pulse. Deconvolution can be applied to generalize the result; however, care is required to avoid numerical instabilities [18, 19]. UWB channel measurements by using short pulses have been presented in [20-22]. In [21], Wireless Personal Area Network (WPAN) was studied over the frequency band of 3.1-10.6 GHz by probing the channel with narrow pulses ~50 ps in duration. Measurements were conducted at short distances only up to 135 cm for both LOS and NLOS scenarios. In [22], indoor UWB channels were characterized for both LOS and NLOS cases by using a Gaussian-like waveform with approximately 7 volt amplitude peak. Although the pulse width is reported as less than 100 ps, no information is provided about the achieved measurement bandwidth as affected by increasing Tx-Rx propagation distances. In general, path loss is expected to be frequency dependent; and measurement of the channel response at high frequencies degrades as the distance between antennas increases.

Another time domain approach for measuring the impulse response of the propagation channel exploits spread spectrum sounders. This method has its roots in chirped radar technology, in which spread spectrum transmit signals, coupled with pulse compression at the receiver, circumvent the trade-off between transmit energy and range [23, 24]. In this method channels are probed by a wideband signal such as PN or multi-carrier spread spectrum waveforms [25-27]. These signals have low peak-to-average ratio, and higher levels of total transmitted power compared to ultrashort pulses, which

results in higher dynamic range. The autocorrelation of these wideband signals can ideally approach a Dirac Delta Function with very low sidelobes [28-30]. In a number of papers in the UWB literature, the channel response has been obtained by calculating the cross-correlation of the waveform measured at the receiver with the transmitted waveform. For example, Durantini et al [31, 32] used a carrier at 4.78 GHz modulated by a PN-sequence to perform channel measurements over a 3.6 – 6 GHz frequency band for distances ranging between 4-7.5 m for NLOS channels and 1-11 m for LOS channels. In [33], a transceiver setup based on SiGe-circuits is reported to generate periodic m-sequence waveforms covering a baseband frequency range of approximately 0-5 GHz, which can be up converted to cover either the UWB band or for coverage in the 60 GHz band. Receiver consists of a down-convertor, a track-and-hold circuit, and an analog to digital convertor (ADC) which uses periodic sub-sampling at a rate below Nyquist. To achieve accurate sub-sampling and also up/down-conversion, careful synchronization is required. This transceiver is commercially available as a robust box in [34].

In this chapter, we perform spread spectrum channel sounding using signals from an arbitrary waveform generator (AWG). The AWG not only provides sufficient bandwidth for channel characterization over a frequency band spanning 2-12 GHz, which exceeds the full FCC UWB band, but also provides the flexibility to choose different spread spectrum waveforms for sounding. This allows us to assess the accuracy of our channel measurements to an extent which, to the best of our knowledge, has not previously been reported in the UWB literature.

Experiments were carried out indoors, both for directional antennas in line-of-sight (LOS) environments and omni-directional antennas in non-line-of-sight (NLOS) environments, in the latter case with up to 15 m antenna separation. Because of the practical difficulty of producing sounding signals with an ideal delta function autocorrelation, equivalent to a white power spectrum, it is important to account for the source spectrum in extracting the system impulse response. Because our experiments achieve good SNR over the full measurement band, we are able to employ a simple deconvolution procedure to accurately extract the impulse response. A special emphasis of our work is to assess the accuracy of our time domain measurements in typical indoor

environments. Both spiral and biconical antennas (arranged in either co-polarized or cross-polarized orientation) are considered. In one scheme to assess the accuracy of our measurements, we compare channel responses obtained using two different common spread spectrum waveforms, PN sequences and chirp signals. We show despite their well known different characteristics [35], under our channel environments, independent measurements show excellent agreement, with correlation coefficients about 0.99. In a second assessment approach, accuracy is tested by performing time reversal (TR) [7, 9, 36] experiments based on the measured channel impulse response. Here the time reversal experimental results are compared with the simulation trace that shows what should ideally be measured at the receiver in the time reversal experiment if there is no noise and if our impulse response measurements are perfectly accurate. Here the correlation coefficients between experimental and theoretical time-reversal traces are on the order of 0.98, which further confirms measurement accuracy. To the best of our knowledge, this is the first experimental report of TR over the whole UWB FCC mask. Other experimental TR literatures either cover a small portion of the UWB [7], or are completely out of the main UWB band (3.1-10.6 GHz) [9].

We note that in general, path loss is frequency dependent and high frequencies experience more attenuation than low frequencies, especially in NLOS environments [37]. Therefore, exciting the channel by a waveform covering a specified frequency band does not guarantee signal-to-noise sufficient to measure the channel response over the entire band. In this chapter we make a point to report power spectra not only of transmitted channel sounding signals, but also of the resulting signals measured at the receiver. In contrast to many time domain channel response measurements reported in the literature, this practice helps to more fully specify the band over which impulse responses are characterized.

In many of our experiments, we introduce a simple optical fiber link to achieve synchronization between transmitter and receiver. This facilitates achieving high quality synchronization, even in NLOS cases with transmitter and receiver placed in different rooms with up to 15 meters of separation.

This chapter is organized as follows. Section 2.2 provides details of the physical measurement setup. Section 2.3 describes our measurement methodology, including the characteristics of the transmitted sounding signals and the processing algorithm employed to extract the impulse responses. Examples of measurement results are reported in section 2.4, both for spiral and omni-directional antennas.

## 2.2. Experimental Setup

Fig. 2.1 shows a block diagram of the measurement system. The main components of the transmitter block are an arbitrary waveform generator (AWG), ultrabroadband amplifier, and the transmitting antenna. We used our Tektronix AWG 7122B in interleaving, zeroing-on mode, which provides the maximum available bandwidth. In interleaving mode, signals from two 12GS/s D/A channels are offset in time by half of the sampling period and passively combined to reach a maximum sampling rate of 24GS/s. Interleaving also permits two modes of operation, zeroing on and zeroing off, which determine how individual samples are handled. In zeroing-off mode, the two D/A channels provide non-return-to-zero waveforms which are summed together. With zeroing on, each waveform is brought to zero before the next sample, and the output signal is the summation of the two waveforms with zero gaps between samples. Zeroing on has higher frequency response in comparison with zeroing off, but the maximum
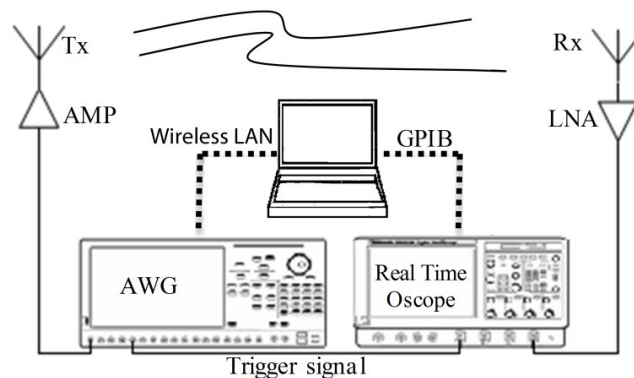


Fig. 2.1: Block diagram of the measurement system

output amplitude is reduced from 1 $V_{P-P}$ to 0.5 $V_{P-P}$. The AWG in interleaving, zeroing-on mode has an effective RF bandwidth (-6dB) of 9.6GHz, with a rise and fall time (20% to 80%) of 35ps. The output of the AWG is amplified by an ultrabroadband amplifier (Picosecond Pulse Labs 5828A) with 10dB gain, 6 dB noise figure, 12 dBm maximum output power and 14 GHz bandwidth. We have used two different antennas in our experiments: Directional Archimedean spiral antennas (NURAD 9C41600, 2-18 GHz), which are strongly dispersive and have circular polarization, and wideband omni-directional antennas (ELECTRO - METRICS EM-6865, 2-18 GHz) which have vertical polarization and uniform radiation pattern in the azimuth plane. The EM-6865 is composed of two brass biconical elements which are connected point-to-point and make up an antenna element shaped like a vertical infinity symbol.

The received response of the Rx antenna is passed through a Low Noise Amplifier (LNA) (B&Z Technologies, BZP120UD1). The selected LNA has a flat frequency response over 0.1-20 GHz, a 2.2 dB noise figure and a minimum 31 dB gain. Depending on the Tx-Rx distance, antenna type (directional or omni-directional) and environment (LOS/NLOS), channel loss varies significantly, and for some experiments we choose to add up to two more amplifiers on the receiver side. These amplifiers are identical to the ultrabroadband amplifier used on the transmitter side. Such additional amplification is particularly important for receiving high RF frequencies which experience more attenuation. In cascading amplifiers it is important to avoid amplifier saturation, which in our experiments arises due to interference from Wi-Fi wireless signals with frequency of 2.44GHz. Hence, when extra amplifiers are used at the Rx, a high pass filter is used after the LNA. This filter (Mini-Circuits, VHF-3100+) has approximately constant transmission over the 3-11.5GHz band and roughly 43dB insertion loss at 2.44GHz, which is sufficient to avoid saturation due to Wi-Fi signals.

The received signal after amplification is directly connected to the real-time oscilloscope (Digital Serial Analyzer, Tektronix DSA 72004B) with 20 GHz analog bandwidth and maximum real-time sampling rate of 50 GS/s. The "average" data acquisition mode, in which we average over 256 measurements, is used to reduce additive noise. The data acquisition time is approximately 400 ms, dominated by

oscilloscope dead-time between successive measurements in averaging mode. The oscilloscope is triggered by one of the AWG's digital "marker" outputs which is synchronized with the transmitted waveform with timing jitter below 30 ps and a rise/fall time (20% to 80%) specified to be 45 ps. For short Tx-Rx distances ( ≤6m), the trigger signal is sent to the oscilloscope by a coaxial cable. As the distance between antennas increases, particularly for NLOS environment where we have to pass the cable through the doors, the loss and dispersion in the cable results in higher jitter [22]. To solve this problem, we use a single-mode optical fiber link (0.2 dB/km optical loss [38]) to transfer the trigger signal. A continuous-wave (CW) optical signal at 1.55μm wavelength from a tunable laser (Agilent 81689A) is directed into a commercial lithium niobate intensity modulator (IM) with DC electrical bias adjusted for roughly 50% transmission and with an amplified version of the AWG marker signal connected to the RF input of the IM. This creates an optical intensity modulation that mirrors the electrical marker signal [38]. The modulated optical signal is connected through fiber to a high speed photodetector (THORLABS DET01CFC, 2 GHz RF bandwidth) which provides the high speed electrical signal for triggering the oscilloscope. Signals recorded by the oscilloscope are stored on a personal computer using a GPIB interface. For NLOS experiments the operator is typically positioned in the same room as the Rx.  The AWG is controlled remotely over a wireless local area network.

Measurements have been carried out in the subbasement of the MSEE building at Purdue University. Channel propagation is studied in different locations for omni-directional and spiral antennas to prove the accuracy of our measurements in several independent experiments. For omni-directional case, we measured LOS and NLOS scenarios. LOS experiments were conducted in a large laboratory (15 m ×10 m) which contains metallic desks, cabinets, computers and scattering objects of different sizes. For NLOS measurements, we placed the transmitter in the laboratory and the receiver in an office across from the laboratory, and there are two cement walls and a hallway in the direct path of the Rx-Tx antennas. As we mentioned, the omni-directional antenna has vertical polarization and uniform radiation in the azimuth plane. We conducted our measurements in two different co-polar and cross-polar topologies for omni-directional

antennas. In co-polar experiments, both the Tx and Rx have the same vertical polarization, while in cross-polar measurements, the Tx and Rx have different polarization directions (we rotated the Rx antenna $90^{o}$ degrees to have horizontal polarization). For spiral antennas, different situations were studied, including LOS, NLOS in the same room by pointing antennas to different directions, and NLOS by placing antennas in different rooms. In this chapter, we present our channel measurement method in detail for the LOS spiral and NLOS co-polar omni-directional cases. We have chosen these two examples because different physical interactions are mainly involved in these two experiments. In the NLOS omni-directional case, the transmitted signals from the Tx can be propagated in all directions and reach the Rx via different paths and interactions (e.g. reflection, diffraction or scattering). The received response in this experiment mainly consists of different components which have certain delays and attenuations due to the paths they took in their propagations from the Tx to the Rx. In the LOS spiral experiment, antenna distortions, especially dispersion, affect the received response, and the measured impulse response is mainly antennas' dispersion. In addition to the results of these two specific scenarios which are presented in detail, the accuracy of measurement performed in several other scenarios is tabulated in Table 2.1, which is discussed later.

## 2.3. Measurement Method

### 2.3.1. Probe Signals

We used PN sequences and chirp signals for channel sounding and studying accuracy of our measurements. PN sequence can be easily generated by a switching circuit (e.g. SiGe circuits [33]) and is the most common waveform used in spread spectrum channel sounding. In the experiments here, we used the AWG to generate a maximal length PN sequence with 2047 chips and a 24GHz chip rate, corresponding to a waveform duration of ~85.3ns. The chirp signal used in our experiments is a linear swept-frequency sinusoid whose frequency increases in time (up-chirp) from 0 to 12 GHz over the same 85.3ns time aperture used for the PN-sequence. In both cases the AWG is
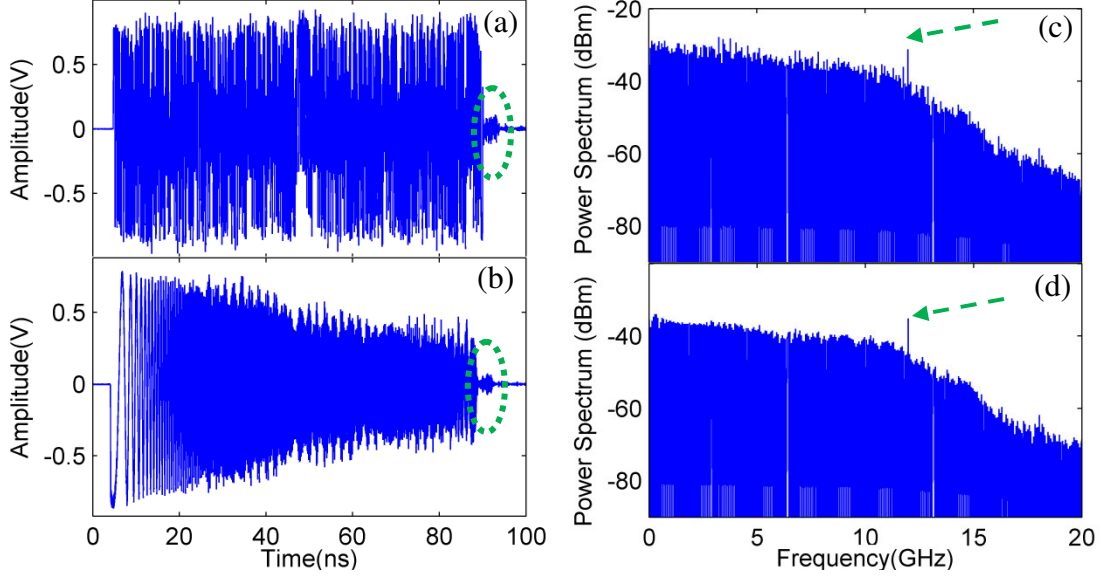
Fig. 2.2: (a), (b) Generated PN and chirp signals in time domain, respectively. Both the PN and chirp waveforms have a nominal duration of 85.3 ns. (c), (d) RF power spectra of the generated PN and chirp signals, respectively. Resolution bandwidth of spectrum analyzer is 100 KHz. Both signals are defined over the frequency range of 0-12 GHz. Indicated parts by ellipsoids show extra features produced by AWG due to RF reflections in interleaving zeroing mode. The RF spectra also exhibit a spur at 12 GHz, equal to the individual channel sample rate of the AWG. These spurs are shown by arrows.

programmed to generate the selected waveforms periodically at 2.4 MHz repetition rate to support averaging. Received waveforms are recorded with 20 ps sampling resolution over a sufficiently long time window (400 ns) to include all multipath components. This corresponds to 20,000 data points per waveform, which can be easily stored in our real-time oscilloscope with memory length of 250 Megasamples.

Figures 2.2 (a)-(b) show generated PN and chirp waveforms after amplification by the Tx ("ultrabroadband") amplifier and direct connection to the oscilloscope through a DC-18 GHz triple shielded coaxial cable. Fig. 2.2(b) shows the chirp waveform rolls off in time and its amplitude decreases. This can be explained by considering time-frequency characteristics of our chirp signals, for which the frequency increases linearly with time. Due to the frequency response of the AWG, the later, high frequency components of the signal are generated with lower amplitude than the earlier, low frequency components. Hence, the roll-off in time simply reflects the frequency response of the AWG generating
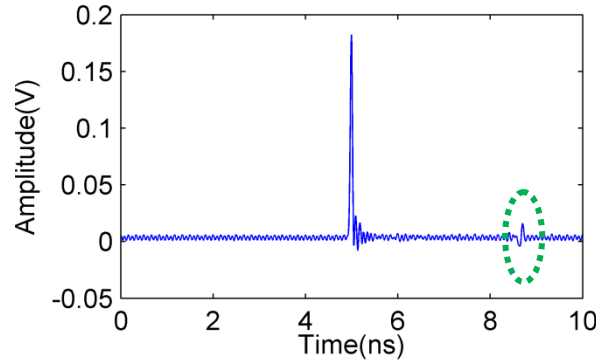
Fig 2.3: Impulse signal generated by AWG with the minimum possible rise time (FWHM is ~50 ps). The indicated part by the ellipse shows the extra feature produced by AWG due to RF reflections in interleaving zeroing mode.

the chirped signal. In contrast, for the PN signal high and low frequencies are present concurrently, and such gradual roll-off in time is not observed. Figures 2.2(c)-(d) display the RF spectra of the amplified transmit waveforms, measured by an RF spectrum analyzer set for 100 KHz resolution bandwidth. Here the high frequency rolloff of the AWG is apparent for both waveforms. The RF spectra also exhibit a spur at 12 GHz, equal to the individual channel sample rate of the AWG. These spurs may arise to differences in the amplitudes of the individual AWG channels or due to inaccuracy in the time offset of the interleaved channels. Finally, the sections of the waveforms indicated by ellipses in Figs. 2.2(a)-(b) highlight an additional nonideal feature present in the AWG output, namely an echo with approximately 4ns delay that arises in interleaving mode due to an RF reflection. This replica is more obvious when the AWG is set to generate an impulse of minimum (~50 ps) duration (Fig. 2.3).

### 2.3.2. Data Processing and Analysis

Figure 2.4 shows a block diagram of the experimental setup used for extracting the impulse response of the system from the received waveform. Figure 2.4(a) portrays a calibration measurement in which the sounding waveform is recorded without wireless transmission, and Fig. 2.4(b) portrays the measurement in which antennas, corresponding amplifiers, and the channel itself are all now included. Equations (2.1)-(2.2) below
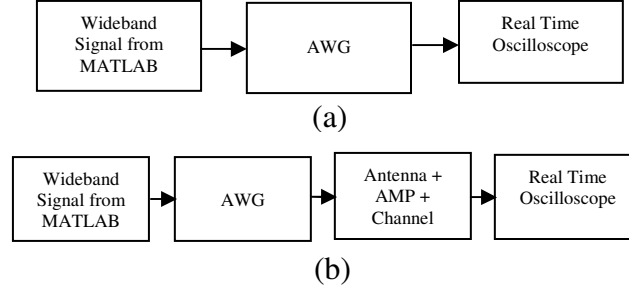
Fig 2.4: Block diagram of the experimental setups. (a) AWG is programmed by the wideband signal and its output is connected to the real time oscilloscope. (b) Channels are excited by the AWG output. Impulse responses of the antennas, amplifiers and channel are included in addition to part (a).

provide a frequency domain description of the calibration and channel measurements portrayed by Figs. 2.4 (a) and (b), respectively.

$$Y_{Trans}(\omega) = E_{Wideband}(\omega) H_{AWG}(\omega) H_{Oscope}(\omega) \tag{2.1}$$

$$Y_{Rec}(\omega) = E_{Wideband}(\omega) H_{AWG}(\omega) H_{Sys}(\omega) H_{Oscope}(\omega) \tag{2.2}$$

Where $H_{AWG}$ and $H_{Oscope}$ are, respectively, the frequency response of AWG and oscilloscope, and $H_{Sys}$ is the frequency response of the antennas, amplifiers, channel and the high-pass filter (if used in our system). $E_{Wideband}$ denotes the ideal spread spectrum (PN or chirp) signal generated by MATLAB in frequency domain, $Y_{Trans}$ is the output of AWG connected by a short RF cable to the oscilloscope, and $Y_{Rec}$ includes channel, antennas, amplifiers and the high-pass filter (if used in our system) in addition to $Y_{Trans}$. To extract $H_{Sys}(\omega)$ from $Y_{Rec}$, different approaches can be employed [26, 27]. Here we compare two simple approaches, one of which takes into account the spectral characteristics of the sounding waveform and one of which does not. Although both of the methods we consider are well known [26, 39], we discuss our specific implementation in detail so that interested readers can replicate our measurements if desired.

For ideal spread spectrum signals with a pulse-like autocorrelation, the unbiased impulse response can be derived from the cross-correlation of the received response with the transmitted signal. This approach, which has been used in a number of spread

spectrum channel sounding papers [31-33], is expressed mathematically, in time and frequency domains respectively, as:

$$h_{Sys}^{XC}(t) = y_{Rec}(t) * y_{Trans}^{*}(-t) \tag{2.3}$$

$$H_{Sys}^{XC}(\omega) = Y_{Rec}(\omega) Y_{Trans}^{*}(\omega) = \left| E_{Wideband}(\omega) H_{AWG}(\omega) H_{Oscope}(\omega) \right|^{2} H_{Sys}(\omega) \tag{2.4}$$

Where * denotes the convolution operation; and $y_{Rec}$, $y_{Trans}$ and $h_{Sys}^{XC}$ are the impulse responses related to $Y_{Rec}$, $Y_{Trans}$ and $H_{Sys}^{XC}$ by Inverse Fourier Transform (IFT). In our notation, $H_{Sys}^{XC}(\omega)$ and $h_{Sys}^{XC}(t)$, respectively, refer to estimates of the frequency response and impulse response of the channel, antennas and amplifiers obtained via cross-correlation processing. In (2.3), although $y_{Trans}$ and $h_{Sys}^{XC}$ are real since we are considering them to be baseband signals, we retain the complex conjugate so that (2.3) is also applicable to the case where $y_{Trans}$ and $h_{Sys}^{XC}$ are considered as envelope functions with an assumed carrier.

In this approach only the spectral phase of the sounding signal ($Y_{Trans}$) is compensated; its frequency dependent magnitude still contributes to the final estimation of the system transfer function (e.g., neither the high-frequency roll-off of the AWG response, nor other irregularities in the power spectrum due to the echo in the AWG response, are compensated). As a result, when the transmitted spread spectrum signal is not white (autocorrelation is not a delta function) [25, 28], an unbiased estimation cannot be achieved using just (2.3) and (2.4). These power spectrum imperfections can easily occur in practical measurement system involving ultrawide bandwidths [31-33]. To illustrate, examples of our experimental autocorrelations are shown in Fig. 2.5 for PN and chirp transmit signals ($y_{Trans}$). For example, due to RF reflections internal to the AWG, the autocorrelations of both transmitted signals have unwanted peaks at approximately ±4 ns of the main peak. Also, although the autocorrelations of ideal, periodically repeated PN-sequences (known as periodic autocorrelation) are known to have an ideal pulse like property [28], the autocorrelation of the single period of a PN-sequence which is used in
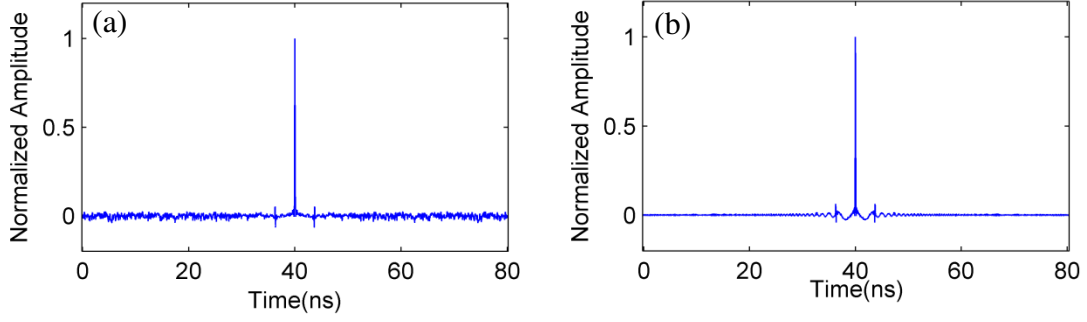
Fig 2.5: Autocorrelation of (a) PN (b) chirp. Extra replicas at ~4 ns of the main peak are due to AWG RF reflections.

our experiments, exhibits significant low level structure outside of the main peak [31]. On the other hand, the sidelobes of the autocorrelation of single frame chirp signals behave like a Sinc function [29] and have comparable quality to the sidelobes of periodic autocorrelation.  As a result, the autocorrelations computed from our experimentally measured transmit signals are significantly cleaner for the chirp waveform than for the PN waveform, though neither is ideal.  Because of such practical issues, the quality of impulse responses computed via (2.3) and (2.4) will be compromised, since the nonideal autocorrelation and power spectrum of the sounding waveform are not taken into account.

A simple approach that does take into account the full source characteristics is deconvolution [26, 27]. The deconvolution operation can be performed either in the time [18, 19] or frequency domain; here we operate in the frequency domain by the application of the Fast Fourier Transform. Symbolically, we can write:

$$H_{Sys}(\omega) = \frac{Y_{Rec}(\omega)}{Y_{Trans}(\omega)} \tag{2.5}$$

$h_{Sys}(t)$ can be computed from $H_{Sys}(\omega)$ by inverse transform:

$$h_{Sys}(t) = \frac{1}{2\pi} \int_{-\infty}^{+\infty} H_{Sys}(\omega) e^{j\omega t} d\omega \tag{2.6}$$

We use the notation $H_{Sys}(\omega)$ and $h_{Sys}(t)$, without superscript, to refer to estimates of the frequency response and impulse response, respectively, obtained via the deconvolution method, which we use throughout the rest of this chapter unless otherwise

noted. Although (2.5) and (2.6) are simple, they are computationally unstable around the zeros of $Y_{Trans}$ and mathematically classified as an ill-posed problem. In general, these equations are extremely sensitive to the presence of noise, and the transmitted signals, $Y_{Trans}$ ,should maintain a good SNR over the desired spectral range. In our experiments, as the transmitted signals cover frequency range up to 12GHz, we resample the recorded data at 24 GHz, and apply (2.5) to the resampled data. Because the transmitted signals have good frequency content up to 12 GHz (see Fig. 2.2 (c)-(d)), we did not face instability problems in our computations. By implementing deconvolution in (2.5), modulations of the transmitted power spectrum due to system imperfections are taken out which ideally results in an unbiased estimation of the system impulse response.

For each antenna placement, we have also implemented the time reversal technique [9, 36]. Our experimental procedure consists of resampling the obtained channel impulse response at 24 GHz, inverting the result in time, and programming this directly onto the AWG. This signal is then transmitted, and the new waveform measured at the receiver is recorded using the oscilloscope. We compare this result with the simulated signal which is the autocorrelation of the measured channel impulse response convolved with the impulse response of AWG and oscilloscope:

$$y_{TR}\left(t\right) = h_{Sys}\left(-t\right) * h_{Sys}\left(t\right) * h_{AWG}\left(t\right) * h_{Oscope}\left(t\right) \tag{2.7}$$

For these simulations we measured the impulse response of AWG and oscilloscope by dividing the spectral amplitude of the chirp signal recorded at the output of the AWG, $Y_{Trans}(\omega)$, by the spectral amplitude of the ideal chirp waveform, $E_{Wideband}(\omega)$ . This yields a better signal-to-noise ratio in comparison with the direct impulse response measurement showed in Fig. 2.3. This simulation approach shows what should ideally be measured at the receiver in time reversal experiments if there is no noise and if our channel measurements are perfectly accurate. Comparing this form of simulation with the time reversal experiment provides an additional check on the accuracy of the estimated channel impulse responses. Results for two different antenna types and propagation scenarios are discussed in section 2.4.
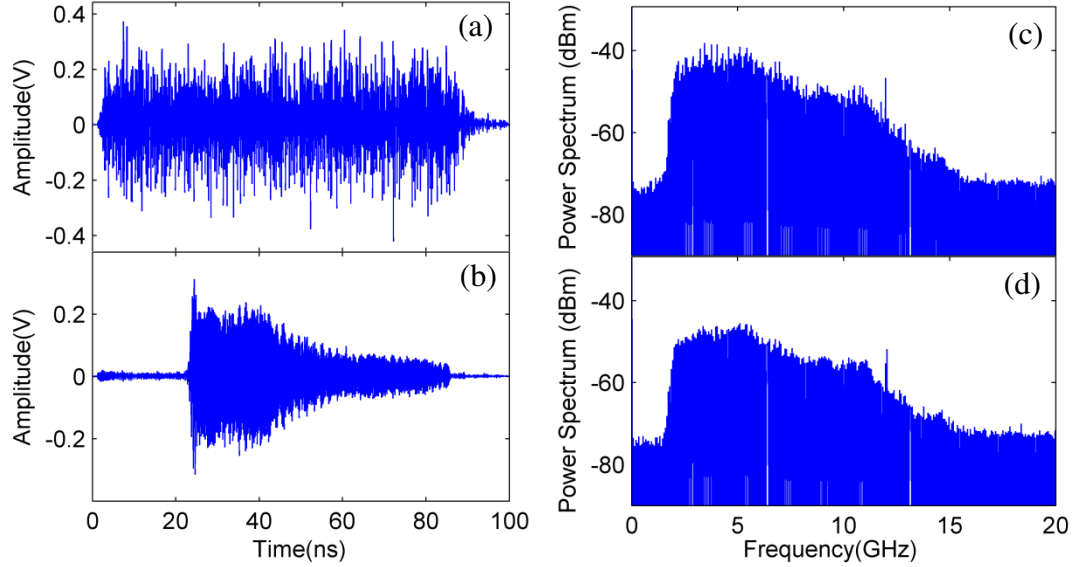
Fig. 2.6: Received responses from (a) PN (b) chirp. Time durations of the chirp and PN responses are ~64 ns and ~94 ns, respectively. (c) RF power spectrum of the received response from PN excitation (d) RF power spectrum of the received response from chirp excitation.

## 2.4. Impulse Response Measurements

### 2.4.1. Directional Spiral Antenna

We first measure impulse response for two spiral antennas in LOS situation which mainly includes antennas' dispersion effects. The dispersive pulse response of these spiral antennas was previously studied in [40, 41], where pulses of variable bandwidth and center frequency obtained from a photonic waveform generator were used for antenna excitation. In the experiments here, the height of the antennas is 1.8m and their distance is 3m to satisfy far-field conditions. Because path loss is small in this measurement, we placed just one LNA in the receiver side, in addition to the ultra-broad band AMP which we have used on the Tx side in all our experiments.

Fig. 2.6 (a)-(b) are the received responses from PN and chirp excitations in time domain. As we mentioned, nominal duration of the probing PN and Chirp signals are 85.3ns. Fig. 2.6 (b) shows the received response of chirp excitation is shorter than the PN response and the transmitted signal length. This again can be explained by considering
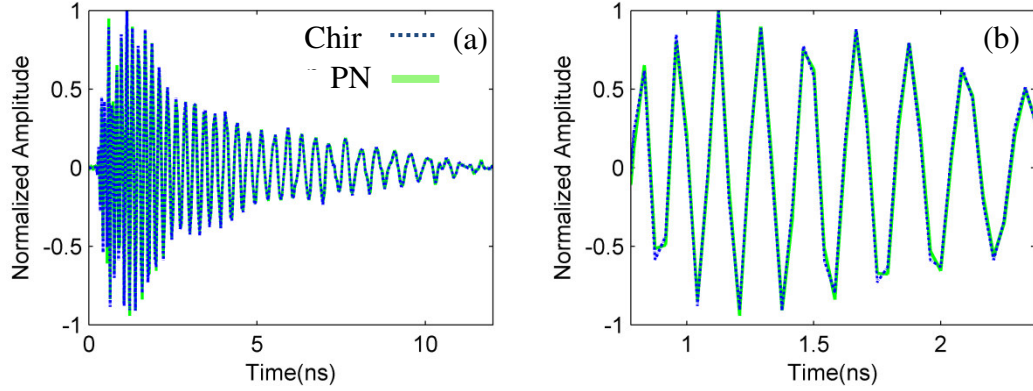
Fig 2.7: Experiments using spiral antennas in a LOS topology (a) The dotted and continuous curves are calculated impulse responses of chirp and PN excitations, respectively. (b) Zoom in on (a) to better show the agreement between two measurements.

(up to 2GHz) are filtered out, and therefore the exciting signal becomes shorter than 85.3ns. On the other hand, our spiral antennas have a strong down-chirp impulse response, while the signal generated by the AWG is an up-chirp waveform. Propagation of this up-chirp waveform through a down-chirp antenna introduces partial time domain compression [40, 41]. These two effects together result in a shorter response compared to the PN excitation experiment. In PN signals, high and low frequencies are present concurrently and transmitting this signal from antenna does not reduce the signal length in the time domain. Fig. 2.6 (c)-(d) show RF power spectra of the received response by using Spectrum analyzer, 33 KHz bandwidth resolution. It is evident our measurement frequency range is ~2-12 GHz. Power spectrum increases from ~2GHz up to ~5GHz then decreases fast from ~5 GHz to ~8GHz and after this point is approximately constant up to 12 GHz. Comparing Fig. 2.6(c)-(d) with Fig. 2.6 (c)-(d) shows spiral antennas introduce ~8dB more loss in frequencies around 10 GHz in comparison with the maximum frequency response around 5 GHz. These results are exactly consistent with the predicted power spectrum shape in [40, 41] which used the same pair of spiral antennas.

Calculated impulse response from chirp and PN excitations based on (2.5) are compared in Fig. 2.7. The agreement between the two curves is excellent. By looking at Fig. 2.7(b) which is zoom in version of Fig. 2.7(a), we can see they match peak for peak and there is at most a few percent difference between them. In order to evaluate
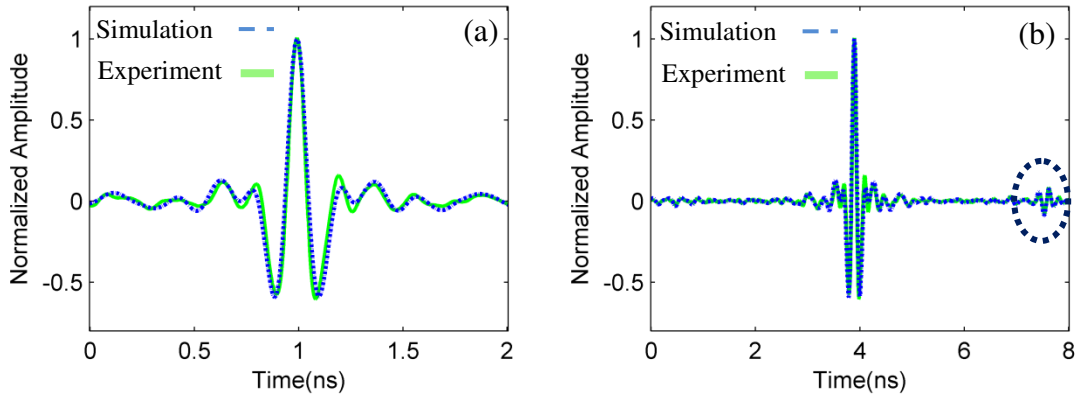
Fig 2.8: Comparison between Time Reversal experiment and simulation for LOS spiral antennas over two time windows. The part indicated by the ellipse corresponds to the echo in the AWG response.

time-frequency characteristics of chirp signals. When this signal is transmitted through the antenna (which has frequency response from 2-18GHz), the beginnings of the pulse similarities between these results, it is useful to calculate the correlation coefficient. For two variables *X* and *Y*, the correlation coefficient is defined as:

$$\rho = \frac{E[XY] - \overline{X}\,\overline{Y}}{\sigma_X \sigma_Y} \tag{2.8}$$

Where *E* is the expected value, σ is the standard deviation. Ideally, in the case of *X=Y*, the correlation coefficient is equal to 1. So, when ρ is close to 1, there is a strong correlation between *X* and *Y*. In our LOS spiral antenna experiment, the correlation coefficient between two calculated impulse responses is 0.997. These results show that calculated impulse response is independent of the transmitted signals, and measurement errors are very small.

Time Reversal results for the LOS spiral antennas, in this case using the impulse response estimated based on the chirped sounding waveform, are presented in Fig. 2.8. Experimental measurements and simulation results are very close. Full width half maximum (FWHM) durations of simulated and experimental TR peaks are both ~50ps, which is equal to the FWHM of the minimum pulse that can be generated by the AWG. Fig. 2.8(b) shows this result over a longer time window. Both experiment and  simulation
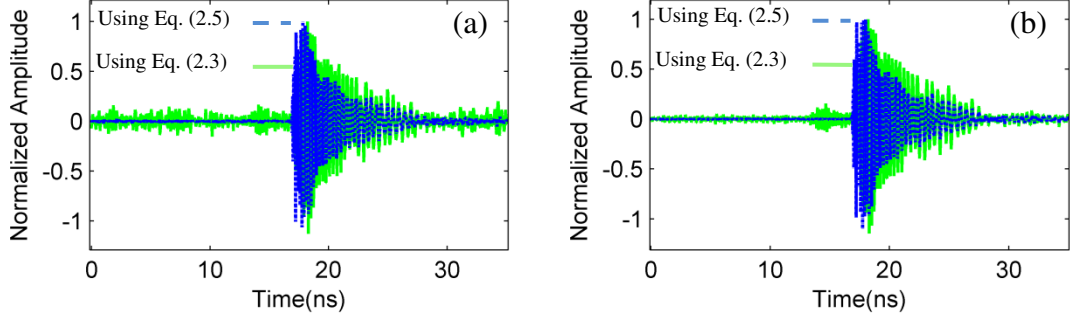
Fig. 2.9: Comparison between impulse responses calculated via (2.3) and via (2.5) for spiral antennas in a LOS topology. (a) PN excitation (b) chirp excitation.

show an extra feature at ~4 ns after the main peak. This can be explained by looking at the TR simulation equation. In (2.7), $h_{Sys}(-t)*h_{Sys}(t)$ is a symmetric signal which based on our method is independent of the AWG impulse response, but when this part is convolved with $h_{AWG}(t)*h_{Oscope}(t)$, the extra replica appears after the main peak due to the RF reflection in the AWG. As we discussed in (2.7), the agreement between the simulation and experimental TR results shows our accuracy in measuring the impulse response of the channel, antenna and AWG. The correlation coefficient between simulated and experimental TR traces is 0.974, which shows remarkable similarity between the two data sets. We also performed TR using the impulse response measured by PN excitation, and the result is essentially indistinguishable from the TR experiment using the channel response measured by chirped excitation.

To show the importance of accounting for the actual source power spectrum in computing the actual system impulse response, Fig. 2.9 compares results computed on the basis of (2.4) with those computed on the basis of (2.5). The results are clearly different. Furthermore, the calculated responses via (2.4) evidently depend on the excitation signal. The impulse response using the PN waveform and (2.4) is noisier than that using chirped excitation. As mentioned earlier, the autocorrelation of our experimental PN sequence has noise-like sidelobes; while the autocorrelation of our chirp signals behaves like a Sinc function. Because (2.4) does not fully account for imperfections of practical ultrawideband sounding waveforms, estimation of impulse responses is degraded. Conversely, because (2.5) does account for such imperfections,

extraction of the impulse response is more robust against waveform variations, provided that sufficient SNR is maintained.

We repeated the same procedure in different locations and environments with spiral antennas to study the accuracy of our measurements in several independent experiments. For example, in a NLOS scenario, we placed the antennas in different rooms and aligned them for the maximum reception. The correlation coefficient between the measured impulse responses of PN and chirp excitations in this case is 0.9953. This value for the simulation and experimental TR is 0.9766 which proves remarkable measurement accuracy even in NLOS scenarios.

### 2.4.2. Omni-directional Antenna

Omni-directional antennas are the most common and appropriate antennas for wireless communication applications. NLOS channel responses for omni-directional antennas have been studied by using frequency domain channel sounding in different literatures [13, 15, 17]. Studying channel characterizations by employing pulse excitation is extremely difficult due to high channel attenuations in these scenarios. In this section, we explain NLOS co-polar channel measurement over the entire UWB frequency range for omni-directional antennas by using our spread spectrum sounding technique. Antennas are located ~15 m far apart, with two cement walls in their direct path, which result in high losses especially for high frequencies. To receive high frequency components and cover the full UWB frequency range, we used 51dB gain amplification on the receiver's side. The main limitation of cascading amplifiers is the saturation effect in the final stages. Wi-Fi wireless signal is the major interference in most residential environments, with a frequency around 2.44 GHz. As explained earlier, instead of turning off the Wi-Fi transmitters, we used a high pass filter (~3-11.5 GHz) which suppresses Wi-Fi signals by 43 dB. Figure 2.10 shows the power spectrum of the channel excitation by the PN signal, and also the noise level when the transmitter is turned off. In these measurements, the spectrum resolution bandwidth is set to 33 KHz. It can be seen with this resolution bandwidth, the noise level is about -65 dBm which is equivalent to the noise power spectral density of -110 dBm/Hz. High UWB frequency components
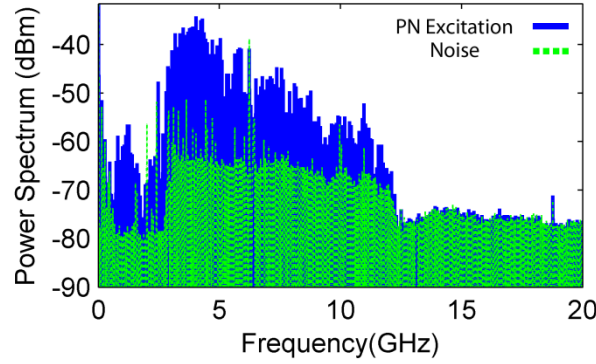
Fig. 2.10: Experiment using omni-directional antennas in a NLOS environment. RF power spectrum at the receiver, after high pass filter and cascaded amplifiers. The continuous plot shows spectrum for PN excitation, and the dotted one is the noise power when the transmitter is turned off.
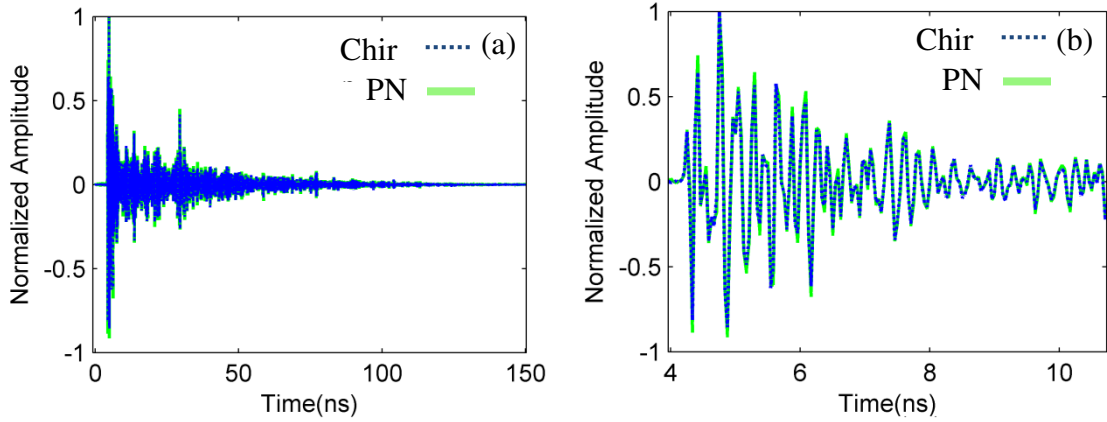


Fig. 2.11: Experiments using omni-directional antennas in a NLOS environment. (a) The dotted and continuous curves are calculated impulse responses using chirp and PN excitations, respectively. (b) Zoom in on (a) to better show the agreement between two measurements.

experience ~25 dB more loss than low frequency components around 3.1 GHz. In contrast, this frequency dependence in LOS measurements (~3m propagation distance) with the same omni-directional antennas is about 7dB. The extra loss for high frequency components in the NLOS case is the result of passing signals through walls. In [37], experimental results show there is ~10 dB loss difference between 3 GHz and 10 GHz when signals propagate through a single indoor cement wall.

Figure 2.11 shows calculated impulse response for PN and chirp excitations using (2.5). Again, we can see the agreement between the results is remarkable and by eye is almost perfect. Again this confirms that our channel measurement is independent of the exciting signal. The correlation coefficient between these two responses is 0.991 which shows strong correlation between the two data sets.

The simulation and experiment of Time Reversal Technique, using the impulse response estimated using chirped waveform excitation, are compared in Fig. 2.12. Fig. 2.12(a) shows the main peak of the TR over a ~6 ns time window. The correlation coefficient between these two data sets over 50ns time range, which covers the main sidelobes of the TR response, is 0.978. In Fig 2.12(b), we zoom in on the sidelobes of the TR response close to the main peak. Some parts of the main peak can be seen on the left side of this figure, to show the agreement between simulation and experimental results on this part of the TR. Again simulated and experimental traces curves agree quite well, which again proves that we have a very small error in estimating the physical response of our system, even in NLOS environments.

We also investigated impulse response measurements in other scenarios to study the repeatability and accuracy of the deconvolution method. Table 2.1 shows correlation coefficients for impulse responses measured by PN and chirp excitations, and also for simulation and experimental TRs based on chirp experiments. LOS and NLOS
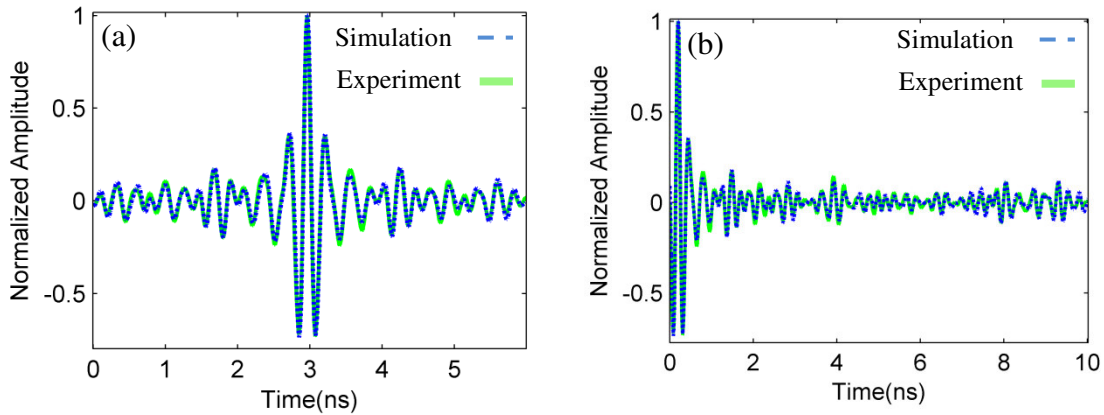


Fig. 2.12: Comparison between simulation and experimental Time Reversal Technique for omni-directional co-polar NLOS environment. (a) main peak of the TR response. (b) ~10ns region of the TR signal following the main peak. Some parts of the peak signal can be seen on the left side of this figure.

Table 2.1: Correlation coefficients for impulse responses measured by PN and chirp excitations, and also for simulation and experimental TR from chirp experiments. *: For omni-directional antennas, we use "LOS" to mean that antennas are in the same room, with no obstruction between them. However, note that cross-polar response arises from scattering.

| Environment Type | Correlation coefficient between impulse responses measured by PN and chirp excitations | Correlation coefficient between simulation and experimental TR |
|---|---|---|
| Spiral LOS | 0.997 | 0.974 |
| Spiral NLOS | 0.995 | 0.976 |
| Omni-directional co-polar LOS | 0.997 | 0.986 |
| Omni-directional cross-polar LOS * | 0.995 | 0.987 |
| Omni-directional co-polar NLOS | 0.991 | 0.978 |
| Omni-directional cross-polar NLOS | 0.990 | 0.975 |

experiments were conducted in the environments described in section 2.2. The presented values are examples of several measurements we conducted in different locations. This technique shows comparable performance for co-polar and cross-polar measurements, but, in general, LOS experiments for omni-directional antennas have higher correlation coefficient values in comparison with the NLOS measurements. This can be explained by considering the overall amplifier gain value on the Rx side in these two scenarios. In NLOS experiments, we amplified the received response by the overall 51 dB gain, however, we have lower path loss in LOS experiments and the overall receiver gain is 20dB. Higher gain values on the NLOS receiver side results in more noise amplifications, and, therefore, the correlation coefficient between data sets is lower.

Based on our measurements, impulse response of the channels can be changed dramatically from one location to another, but, all the measured responses show comparable accuracy to the examples presented in this chapter. This remarkable precision makes spread spectrum sounding highly appropriate for characterizing ultra-wideband radio channels in a variety of situations, as well as for control of channel compensation schemes such as time reversal.

# 3. UWB IMPULSE RESPONSE AND TIME REVERSAL: OMNI-DIRECTIONAL AND DIRECTIONAL ANTENNAS

## 3.1. Introduction

As we mentioned in the previous chapter, due to the large frequency bandwidth of 3.1 to 10.6 GHz, temporal resolutions of UWB systems are extraordinarily fine. This provides the capability to resolve most of the multipath components (MPCs) incident at the receiver. To capture and process received energies which are dispersed over large number of MPCs, complex receiver systems (i.e. Rake receivers [42]) are necessary. Time Reversal (TR) is a transmission technique which can be used in UWB systems to shift the receiver complexities to the transmitter side. TR is based on the reciprocity of the wave equations, and originally proposed as a solution to compensate inhomogeneous media's distortion [43]. In TR, channel impulse response is flipped in time domain, and used as a pre-matched-filter in the transmitter side. The time-reversed waveform is propagated back through the same channel, and multipath components add up coherently at the intended receiver at a particular time after traveling through different paths.

Time reversal performances have been investigated by several authors for UWB communications [6-8, 44-47]. However, the majority did not implement TR experimentally, and their analyses are based on the TR simulation which is basically the autocorrelation of the impulse response of the channel [44-46]. TR performances have been simulated based on IEEE proposed UWB multi-path channel model in [44, 45]. In [46], TR space-time focusing performance is studied based on simulations by taking autocorrelation and cross-correlation of the measured channel impulse responses which give an ideal prediction of TR capabilities when the measured data are noise free and the estimated channel impulse responses are perfectly accurate.

A few other researchers have studied UWB-TR experimentally by exciting the channel with the reversed version of the measured impulse response [6, 7, 9, 47]. Nan et. al. [7] used two omni-directional antennas 5 m away from each other and block the line-of-sight (LOS) path by a bookshelf. Experiments were carried out in the frequency range of 3.5-4.5 GHz, with impulse response measurements performed by using a Vector Network Analyzer (VNA). In [8, 9], experimental TR has been conducted for omni-directional antennas with approximately 8m propagation distance. Measured impulse responses are reversed, truncated and resampled in time, to construct appropriate TR waveforms for generating with an arbitrary waveform generator (AWG). Their measurements are limited to the band of 0.7-2.7 GHz. In [47], the same model of AWG has been used to analyze space time focusing of TR over 6.6m separation distance for omni-directional antennas. These experimental literatures either cover a small portion of the UWB, or are completely out of this band.

In this chapter, we measure impulse responses in time domain by using spread spectrum channel sounding [48, 49]. For each channel measurement, time reversal technique was experimentally applied by generating the time-reversed version of the channel with an AWG. We conducted our measurements over 15 locations in LOS and 15 locations in NLOS environments. Experimental TR results were compared with TR simulations to show the accuracy of our measurements. A special emphasis of this chapter is to assess capabilities of TR technique in suppression of multipath dispersions and antenna distortions in LOS and NLOS environments. For this purpose, impulse response (IR) and TR characteristics are studied for spiral directional and biconical omni-directional antennas, by calculating "root mean square delay spread", and "peak-to-average power ratio". For biconical antennas, channel multipath dispersions are the main reason for the delay spreads, while for spiral antennas, frequency-dependent delays of the antennas significantly modify signals upon radiation and reception. Based on our measurements, Time Reversal is a powerful technique to compensate antennas distortions; however, it is less effective in compressing UWB channel multipath effects.

The remainder of this chapter is organized as follows. Section 3.2 provides details of the environment layout and TR technique. Section 3.3 introduces different parameters to

Fig 3.1: Environment layout. Tx1 and Rx1 show respectively the positions of the transmitter and the receiver grid for the LOS measurements. Tx2 and Rx2 are the corresponding locations for the NLOS experiments.

characterize delay spread and temporal compression of IR and TR experiments. Examples of the IR and TR measurements, for both biconical and spiral antennas, are reported in section 3.4. Also in this section, the experimental results are analyzed, and TR performance is compared for different antenna types in both LOS and NLOS environments.

## 3.2.   Measurement Configuration

Here we use the same experimental setup explained in section 2.2. Spread spectrum channel sounding is employed for impulse response measurement. For details please see Chapter 2.

### 3.2.1.   Environment Layout

Measurements have been carried out in the subbasement of the MSEE building at Purdue University for which the floor plan is shown in Fig. 3.1. Channel propagations and TRs are studied in different locations for omni-directional and spiral antennas, in LOS and NLOS environments. To observe channel variations, in each scenario the Rx antenna is moved along a track to scan a 1.2m×2.4m area, while the Tx antenna is kept at the same location. The minimum inter-element spacing over each grid is 60 cm which

corresponds to 15 total measurement points. The LOS experiments (Tx1-Rx1) were conducted in a large laboratory (room 40 in Fig. 3.1) which contains metallic desks, cabinets, computers and scattering objects of different sizes with average propagation distance of 3.5m. For NLOS measurements (Tx2-Rx2), we placed the transmitter in the laboratory 40 and the Rx in room 39 across from the laboratory. In this case there are two cement walls and a hallway in the direct path of the Rx-Tx antennas and the average propagation distance is 14m. For directional spiral antennas, we aligned the Rx and Tx antennas to aim at each other, while in omni-directional scenarios, signals are propagated and received in all directions, and alignment is not required.

### 3.2.2. Time Reversal Technique

As we mentioned, in an ideal case, the received response from TR can be modeled as the autocorrelation of the impulse response of the system, which is a symmetric waveform. TR simulation can be expressed mathematically, in time and frequency domains, respectively, as:

$$y_{TR}(t) = h_{Sys}^{*}(-t) * h_{Sys}(t) \tag{3.1}$$

$$Y_{TR}(\omega) = H_{Sys}^{*}(\omega).H_{Sys}(\omega) = \left| H_{Sys}(\omega) \right|^{2} \tag{3.2}$$

Where * denotes the convolution operation, $h_{Sys}(t)$ and $H_{Sys}(\omega)$ are the measured impulse response of the channel, antennas and amplifiers, and $y_{TR}(t)$ and $Y_{TR}(\omega)$ are the expected responses of TR technique, respectively, in time and frequency domains. In Eq. (3.1), although $h_{Sys}$ and $y_{TR}$ are real, since we are considering them to be baseband signals, we retain the complex conjugate so that Eq. (3.1) is also applicable to the case where $h_{Sys}$ and $y_{TR}$ are envelope functions with an assumed carrier. As we can see in Eq. (3.2), TR compensates the spectral phase of the transfer function, and $Y_{TR}$ is equal to the square magnitude of the $H_{Sys}$.

In experimental measurements, transmitted signals from AWG, and received waveforms by the oscilloscope are modified, respectively, by the impulse response of the AWG ($h_{AWG}(t)$) and of the oscilloscope ($h_{Oscope}(t)$). We used the deconvolution method

to measure the combined AWG and scope response by dividing the spectral amplitude of the chirp signal recorded at the output of the AWG by the spectral amplitude of the ideal chirp waveform. These undesired effects are compensated in our measurements by programming the AWG with the waveform *x(t)* which in frequency domain can be expressed as:

$$X(\omega) = \frac{H_{Sys}^*(\omega)}{H_{AWG}(\omega) H_{Oscope}(\omega)} \tag{3.3}$$

When this waveform is constructed with the AWG, if there is no noise and if our response measurements are perfectly accurate, then the recorded TR waveform by the oscilloscope should be equal to the simulation, $y_{TR}(t)$, in Eq. 3.1. To assess the accuracy of the experimental TR, we compare it with the simulation result, and compute the correlation coefficient between the two data sets for each channel measurement.

## 3.3.  Channel Characterization Metrics

In order to characterize the delay spread of the measured impulse response and the quality of time reversal, different parameters can be defined. One of the most useful parameters that affects the data transmission rate over the channel is root mean square (RMS) delay spread. The RMS delay can be used as a practical parameter to measure the time dispersion introduced by multipath channels (when Tx and Rx are omni-directional antennas) and antennas dispersion (when highly dispersive antennas exhibiting frequency-dependent delay behavior are used). This quantity is given by:

$$\sigma \equiv \left[ \frac{\int_0^\infty d\tau \left(\tau - \overline{\tau}\right)^2 \left|s(\tau)\right|^2}{\int_0^\infty d\tau \left|s(\tau)\right|^2} \right]^{1/2} \tag{3.4}$$

where

$$\overline{\tau} \equiv \frac{\int\limits_0^\infty d\tau \ \tau \left|s(\tau)\right|^2}{\int\limits_0^\infty d\tau \left|s(\tau)\right|^2}, \tag{3.5}$$

In (3.4)-(3.5), |s(τ)| is the positive gain of the impulse response of the channel or the received response from TR excitation at delay τ relative to the first detectable signal arriving at $\tau_0$=0. In general, channel characteristic metrics strongly depend on the selected noise floor level. This threshold level should be as low as possible to capture all the real energies, but high enough to avoid the noise effects [22]. In our calculations, we define 37dB threshold level respect to the maximum power and set all components below this level equal to zero. In each measurement we averaged over a large number of waveforms (3000) in order to bring the noise floor sufficiently below the defined threshold that channel performance parameters can be obtained accurately. In a practical system this level of accuracy is not required, and one would not perform such averaging.

To evaluate the temporal focusing effectiveness of TR, we calculate and compare σ for IR and TR experiments in different situations. We define a temporal compression parameter $C_{rms}$:

$$C_{rms} = \frac{\sigma_{IR} - \sigma_{TR}}{\sigma_{IR}} \times 100,$$
(3.6)

Where $\sigma_{IR}$ and $\sigma_{TR}$ are, respectively, the RMS delay values of the impulse response, and the corresponding received response from the TR experiment. The parameter $C_{rms}$ provides a measure of the TR temporal focusing gain. We expect this ratio to be as high as possible to have a good compression by TR technique. Negative values of $C_{rms}$ shows TR increases the RMS delay spread of the channel. In [50-52], it is shown the RMS delay spread increases by TR technique in some environments; however, no physical explanation was provided for this phenomenon. In this chapter, we look at the system transfer functions, $H_{Sys}(\omega)$, to physically elucidate the cause of TR performance deterioration in some environments.

In another route, to show the time compression quality of TR, we define a parameter $\vartheta$ which is the ratio of the peak to the average power (PAPR) of the waveform presented in decibels:

$$\vartheta = 10\log\left(\frac{\max\left\{|s(t)|^2\right\}}{\frac{1}{T}\int_0^T dt \; |s(t)|^2}\right)$$
(3.7)

This quantity is especially important for receivers in which the decision criterion is based directly on thresholding. When TR results in time focusing and concentration of the power in few taps, we expect $\vartheta$ to be larger than the corresponding value for the impulse response measurement. We measure $\vartheta$ over a 200 ns time window for all experiments and present values in decibel. To evaluate PAPR gain provided by TR, a parameter $G_\vartheta$ is defined (in decibels) as:

$$G_\vartheta = \vartheta_{TR} - \vartheta_{IR}, \tag{3.8}$$

Where $\vartheta_{IR}$ and $\vartheta_{TR}$ are, respectively, the PAPR values of the impulse response and the corresponding received response from the TR experiment. The parameter $G_\vartheta$ provides insight about the PAPR gain achieved by implementing TR technique.

## 3.4. Impulse Response and Time Reversal Evaluation

In this section, we investigate Impulse responses and TR performances for spiral and omni-directional antennas. We have chosen these two antennas because they are affected by different important physical interactions. With the omni-directional antennas, the transmitted signals from the Tx can propagate in all directions and reach the Rx via different paths and interactions (e.g. reflection, diffraction or scattering). The received responses in these experiments consist of different components which have certain delays and attenuations. On the other hand, the spiral antennas are directional and strongly dispersive (caused by the frequency-dependant delay characteristic of these antennas). Here, distortions due to the antennas themselves affect the received responses, and the number of multipath components received is reduced compared to the omni-directional case. In particular, in LOS experiments the measured impulse response for spiral antennas is dominated by the antenna's dispersion (frequency dependent delay). This results in significantly different TR performance compared to other scenarios in which multipath propagation is important.

Impulse responses of spiral and omni-directional antennas have been studied separately in a number of papers in the literature, but to our knowledge, there is no comprehensive work to investigate and compare directional and omni-directional

responses and TR performances together. Impulse responses of spiral antennas in different bandwidths for LOS environment have been studied in [40, 41]. In [40], they extracted non-uniform phase characteristics of the antennas and excited the Tx antenna with waveforms designed to compensate the phase response. These references used a photonics-based arbitrary electromagnetic pulse shaper to generate the exciting waveforms. For omni-directional antennas, Molisch et al. [53] presented a comprehensive statistical model based on measurements and simulations for different environments in the frequency range of 3-10 GHz. In [22], indoor UWB channels were characterized in the time domain by using a 100 ps Gaussian-like waveform with approximately 7 volt amplitude peak; impulse responses were studied for directional TEM horn and omni-directional biconical antennas in both LOS and NLOS environments. The main focus of [22] was to study the statistical behavior of the impulse response for directional and omni-directional antennas; investigation of TR characteristics for these links was not considered.

In the following two subsections, we compare IRs and TR qualities of spiral and omni-directional antennas in LOS and NLOS environments. In each subsection, we first study a specific (but typical) impulse response for the omni-directional antennas, and compare in detail with the measured response of the spiral antennas placed at the same locations. Time Reversal is then implemented for these scenarios, and performances are fully investigated in Table 3.1. The typical presented LOS and NLOS experiments have propagation distances of 3.5m and 14m, respectively. We used 10dB gain amplifiers on the Tx side, and excited the antenna with the AWG using the maximum available peak-to-peak voltage of 0.5 volt. In the Rx side, we have 41 dB and 51 dB amplifier gains respectively for LOS and NLOS measurements. Finally at the end of each subsection, we repeat our experiments with the receiving antenna moved over a rectangular grid, and report the average and standard deviation of IR and TR performance metrics in Table 3.2. Finally, Table 3.3 summarizes the key results of this section.

Fig 3.2: Impulse responses of LOS omni-directional and spiral antennas over 100 ns time windows. Power delay profiles of these experiments are shown over 10 ns time windows. Arrows indicate two main components in the omni-directional responses.

### 3.4.1. Line-of-sight Environment

Fig. 3.2 compares the impulse responses of LOS omni-directional and spiral experiments over a 100 ns time window. In the small subfigures, we zoom in on the first 10ns of the power delay profile (PDP) of the responses to better show their characteristics. The PDPs are obtained by taking the magnitude squared of the impulse responses. We can see there are two main components in the impulse response of omni-directional antennas. The first, dominant received signal comes from the direct LOS path between the antennas. The sharp LOS signal proves the omni-directional antennas have low dispersion (low frequency dependent delay). The second multipath component, which is ~6 dB less than the direct path with a reversed amplitude sign, comes from a large metal rack on the left side of the Rx antenna. Spiral antennas are directional and strongly dispersive, so the measured impulse response is dominated by the frequency dependent delay of the antennas rather than multipath effects. Our measured impulse

Table 3.1 : Characterization metrics for the omni-directional and spiral responses presented in Fig. 3.2, 3.3, 3.5 , and 3.6. The LOS IR and TR values are based on the responses shown respectively in Fig. 3.2 and 3.3. The NLOS IR and TR parameters are also calculated for the responses in Fig. 3.5 and 3.6.

| | Antenna | Experiment | RMS delay $\sigma$ (ns) | PAPR $\vartheta$ (dB) | Temporal Compression Gain $C_{rms}$ (%) | PAPR Gain $G_{\vartheta}$ (dB) |
|---|---|---|---|---|---|---|
| LOS | Omnidirectional | Impulse response | 13.98 | 30.3 | -1.3% | 0.0dB |
| | | Time Reversal | 14.16 | 30.3 | | |
| | Spiral | Impulse response | 4.67 | 23 | 50% | 11.23dB |
| | | Time Reversal | 2.35 | 34.23 | | |
| NLOS | Omnidirectional | Impulse response | 21 | 21.95 | 7.2% | 6.17dB |
| | | Time Reversal | 19.5 | 28.12 | | |
| | Spiral | Impulse response | 9.5 | 23.38 | 25.2% | 7.83dB |
| | | Time Reversal | 7.1 | 31.21 | | |

response extends mainly over ~8 ns and shows a strong down-chirp characteristic which is similar to what was reported in [40]. To investigate the severity of the channel dispersion and antenna distortion for omni-directional and spiral antennas, respectively, we look at the parameters $\sigma$ and $\vartheta$ for the LOS impulse responses in Table 3.1. Comparing RMS delay values show the omni-directional response is dispersed over a longer time period compared to the spiral impulse response. Powers for omni-directional and spiral antennas are received in two different patterns. In the absence of good reflectors in the environment, power delay profiles of omni-directional antennas can be considered as a single exponential decay with a strong LOS component. Effects of the first dominant component on the parameters $\sigma$ and $\vartheta$ can be understood by calculating them for the impulse response excluding the first LOS signal. These parameters become $\sigma$=16.3ns and $\vartheta$=24.7dB after removing the first 300ps of the omni-directional impulse response. Comparing these values with Table 3.1 (which is based on the whole IR), we can see that without the first 300 ps, the PAPR reduces ~5.6dB and the rms increases ~ 14.2%. This shows the important effect of the LOS component. However, we have a different situation for the spiral impulse response. Spiral antennas are highly directional, and the impulse response has much fewer multipath components compared to the omni-directional case. In this case, the response is dominated by the LOS component distorted according to the frequency dependent delay of the antennas. If we calculate the
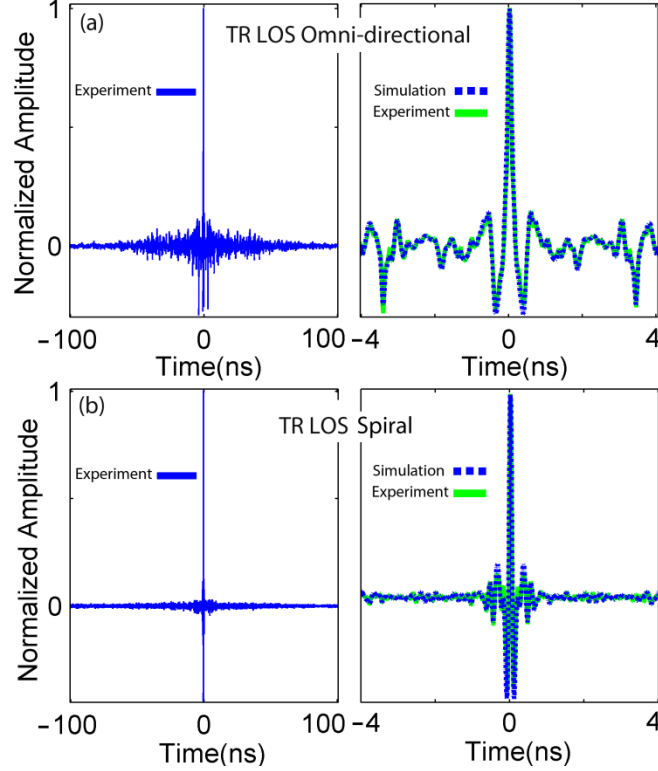
Fig 3.3: Experimental Time Reversal for LOS omni-directional and spiral antennas over 200ns time window. On the right side, we compare experimental and simulated TRs over smaller time windows to show the accuracy of our measurements.

aforementioned parameters for the spiral impulse response excluding the first 300 ps, they become σ=4.9ns and $\vartheta$=23.6dB which are comparable to the original parameters presented in Table 3.1.

Experimental TR results for impulse responses shown in Fig. 3.2 are presented on the left side of Fig. 3.3(a)-(b) over 200 ns time windows. The simulations and experiments of TRs are also compared over smaller time windows to better show the accuracy of our measurements. We can see these curves match peak for peak and there is at most a few percent difference between simulations and experiments. The correlation coefficients between simulations and experimental TR traces are, respectively, 0.991 and 0.966 for omni-directional and spiral scenarios, which shows excellent agreement.

To investigate the achieved gains by implementing TR, we compare the parameters σ, $\vartheta$, $C_{rms}$ and $G_{\vartheta}$ for the LOS TRs in Table 3.1. For the spiral experiment, the PAPR value is increased 11.23dB and the RMS delay spread is significantly shortened (~3 dB)
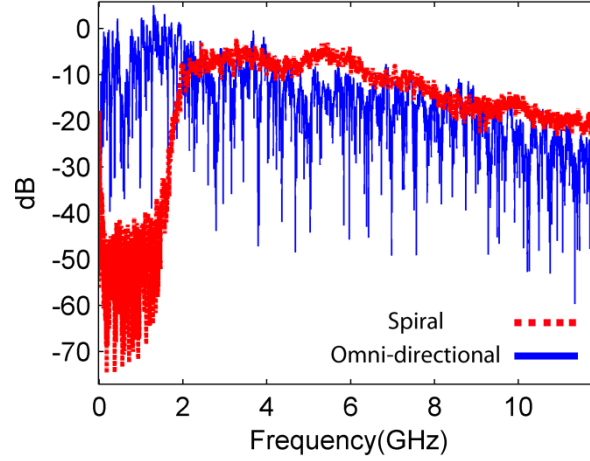
Fig 3.4: Frequency responses of the omni-directional and spiral LOS links computed from the impulse responses shown in Fig. 3.2. Multipath effects make the omni-directional spectrum frequency selective, while for spiral antennas, the transfer function is dominated by the antennas' frequency response.

after implementing TR technique. The response is symmetric and the energy is mainly concentrated around the symmetric point which means, in practical communication systems, a simpler receiver structure would be sufficient to capture a significant amount of the received power.

For the omni-directional antennas, zero PAPR gain ($G_\vartheta$) shows TR does not improve the $\vartheta$ value. Presence of the dominant strong LOS component in the omni-directional impulse response is the main reason for this poor TR performance. As we previously showed, removing the main LOS signal reduces $\vartheta$ from ~30.3dB to ~24.7dB, which shows the important effect of the LOS component on the PAPR value. In general, TR shows better PAPR gains when the strong taps of the impulse response are distributed over time. In the spiral case, there is no single strong dominant component, and TR gives a good PAPR gain value.

The negative temporal focusing ($C_{rms}$ = -1.3%) implies that TR cannot decrease the RMS delay spread of the channel, which is consistent with the results predicted by simulations in [51]. To explain the poor LOS TR performance of omni-directional compared to the spiral antennas, we look at the frequency responses of these experiments in Fig. 3.4. These frequency responses are calculated by taking Fast Fourier Transform

(FFT) of the measured impulse responses shown in Fig. 3.2. For omni-directional antennas, the spectrum is significantly frequency selective, which is the direct consequence of the channel multipath effects. Transmitted signals reach the Rx via different paths and experience certain delays and attenuations. The different delay components interfere in the frequency domain, yielding a frequency selective spectrum with many sharp fades. On the other hand, in LOS the transfer function of the directional spiral antennas is dominated by the frequency responses of the antennas. Multipath effects are limited in the directional antennas, and there are no such sharp fades in the spectrum. This result is exactly consistent with the shape of the power spectra measured in [41] by using an RF spectrum analyzer.

As we mentioned in Eq. (3.1)-(3.2), TR has two principal effects on the frequency domain representation of the received signal: 1) compensating the spectral phase; and 2) squaring the spectral magnitude. The first effect results in concentration of power at the center of the received response and reduces the RMS delay spread of the channel. The second effect shapes the power spectrum, increasing roll-off in the spectrum (e.g., at high frequencies) and accentuating sharp spectral variations (peaks, fades, etc). Both aspects of the second spectral shaping effect correspond to the aggravation of the overall system amplitude distortion and result in time broadening. Based on whether the phase compensation effect or the spectral shaping effect is stronger, the RMS delay spread of the channel can be either increased or decreased by the TR technique. The amplitude response of the LOS spiral antennas is approximately smooth; phase compensation is the dominant effect, which, overall, reduces RMS delay spread. However, for the LOS omni-directional antennas, presence of sharp fades in the transfer function makes the broadening effect of the spectral shaping more important. On the other hand, the spectral phase of the received response is dominated by the phase of the LOS component [3] which is essentially subject to no spectral phase variation. Due to this dominant undistorted LOS component, the spectral phase compensation effect provides less compression. As a result of these two phenomena, TR does not give an effective compression performance in the omni-directional LOS scenario.

Table 3.2: Average (Avg) and standard deviation (Std) values for omni-directional and spiral experiments over 15 different LOS locations and 15 different NLOS locations. In the text, we refer to impulse response metrics by "IR-Metrics Name" (e.g. spiral IR-PAPR means the average PAPR value for spiral impulse response measurements).

| | | | RMS delay $\sigma$ (ns) | | PAPR $\vartheta$ (dB) | | Temporal Compression Gain $C_{rms}$ (%) | | PAPR Gain $G_{\vartheta}$ (dB) | |
|---|---|---|---|---|---|---|---|---|---|---|
| | | | Avg | Std | Avg | Std | Avg | Std | Avg | Std |
| LOS | Omni-directional | IR | 14.3 | 1.1 | 29.8 | 1.5 | -7.8 | 16.9 | 0.8 | 1.6 |
| | | TR | 15.5 | 3.0 | 30.6 | 0.5 | | | | |
| | Spiral | IR | 5.56 | 0.68 | 23.0 | 0.25 | 44.3 | 10.4 | 11.0 | 0.35 |
| | | TR | 3.13 | 0.87 | 34.0 | 0.23 | | | | |
| NLOS | Omni-directional | IR | 19.7 | 2.01 | 21.8 | 1.77 | 16.4 | 6.9 | 5.1 | 1.7 |
| | | TR | 16.4 | 1.4 | 26.9 | 0.6 | | | | |
| | Spiral | IR | 9.2 | 1.97 | 22.8 | 1.45 | 16.6 | 10.4 | 7.5 | 1.69 |
| | | TR | 7.7 | 2.04 | 30.3 | 0.76 | | | | |

As explained earlier, we repeated LOS impulse response and TR measurements over a rectangular grid to observe more channel realizations. In table 3.2, we summarize average and standard deviation values of the performance metrics for these measurements under the LOS section. In general, standard deviations of spiral links, due to the limited channel multipath effects, are smaller compared to omni-directional antennas. We investigate effectiveness of TR technique in each scenario by measuring temporal compression and PAPR gains. As we can see, trends of average values are consistent with the physical discussions provided for the typical responses in Fig. 3.2. Although more measurements are required to derive a statistical model for the gain (e.g. the probability of the negative compression gain in omni-directional LOS experiments), we can already conclude that TR does not effectively compensate channel multipath dispersion in the LOS regime.

### 3.4.2. Non-line-of-sight Environment

In this section, we investigate impulse responses and TRs of omni-directional and spiral antennas in NLOS environments. Fig. 3.5 shows the impulse responses of NLOS omni-directional and spiral experiments over a 200ns time window. The power delay profiles over the first 10ns are also presented in two subfigures. For omni-directional
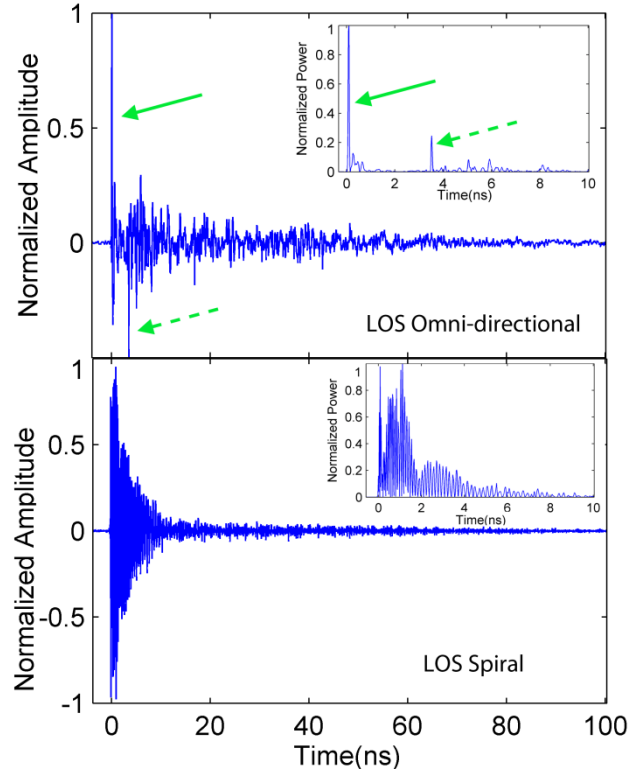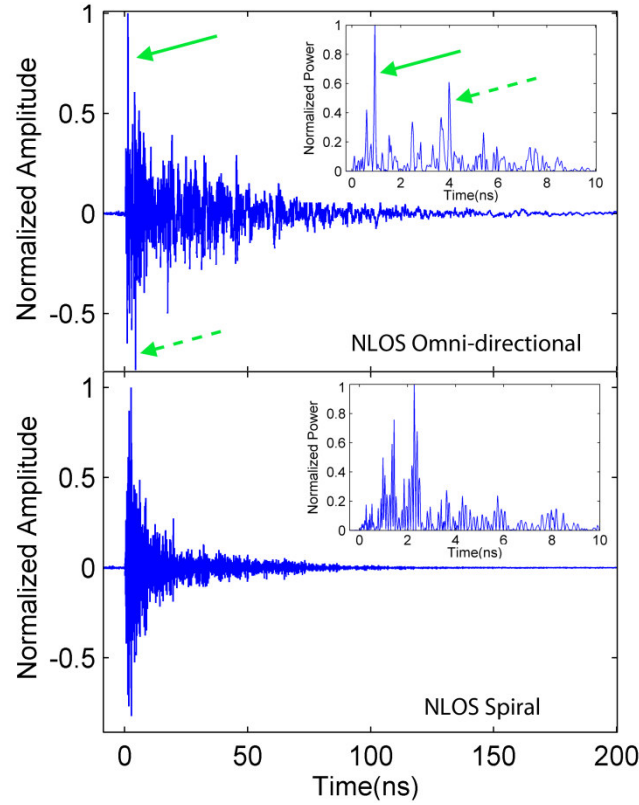
Fig 3.5: Impulse responses of NLOS omni-directional and spiral antennas over a 200 ns time window. Power delay profiles of the omni-directional and spiral experiments are shown over 10 ns time windows in the small subfigures. The continuous and dashed arrows, respectively, show the first and second strongest components in the NLOS response.

antennas, multipath components are distributed over time; unlike the LOS case, no strong dominant component exists in the channel response. The second strongest component in this case is just 2.2 dB less than the main one; while, for the LOS experiment, this value was in the order of ~6 dB. Comparison with the omni-directional impulse response parameters in Table 3.1 clarifies the basic differences between the LOS and NLOS responses. The IR-RMS delay of the NLOS channel ($\sigma$=21.0 ns) is ~50% larger than the RMS delay of the LOS scenario ($\sigma$=13.98 ns). The transmitted signals in NLOS environments experience more interactions (reflections, diffractions, etc) in their paths to the receiver, and therefore more multipath components incident at the Rx. The signal must pass through at least two cement walls to reach the Rx antenna, which increases the high frequency attenuation of the received response [37]. Due to the absence of the strong
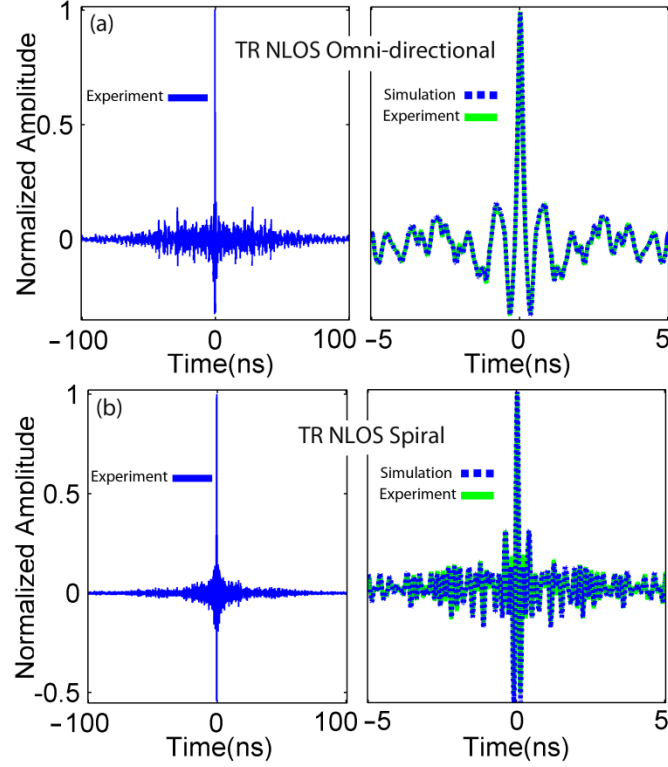
Figure 3.6: Experimental Time Reversal traces for NLOS omni-directional and spiral antennas over 200ns. On the right side, we compare experimental and simulated TRs over a smaller time window to show the accuracy of our measurements even in NLOS environments.

LOS component, the PAPR value ($\vartheta$=21.95 dB) is ~8.3 dB less than the corresponding value for the LOS case.

For spiral antennas, the IR-RMS delay in the NLOS case is approximately two times the spiral LOS situation. Therefore, with the increased antenna separation and the NLOS configuration, multipath effects now contribute more strongly to the delay spread than does antenna frequency dependent delay. As mentioned earlier, the two cement walls in the path of the antennas also introduce high frequency attenuation. Comparing the NLOS spiral antenna IR-RMS delay with that of the omni-directional antenna shows multipath effects are still reduced for directional antennas. For LOS spiral experiments, we did not have any dominant component that affects the PAPR value dramatically, so this value for the NLOS case is comparable to the LOS scenario.
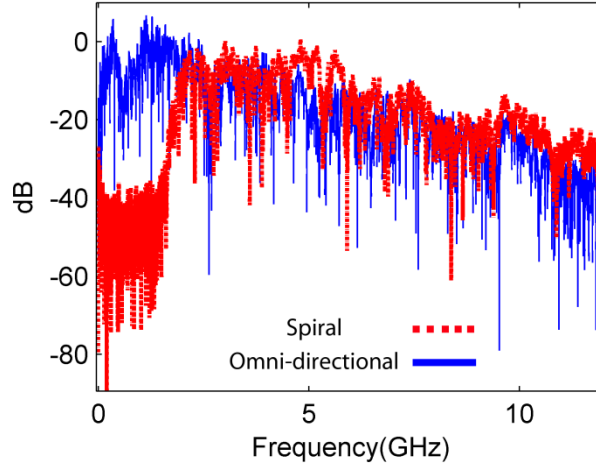
Fig. 3.7: Frequency responses of the omni-directional and spiral NLOS links of the impulse responses shown in Fig. 3.5. Both spectra have a faster decreasing slope (compared to the LOS case (Fig. 3.4)) due to the longer propagation distance and presence of cement walls in the propagation path. Multipath effects make these spectra frequency selective.

TR technique is implemented for these impulse responses and results are presented in Fig. 3.6 (a)-(b). Simulations and experiments of TRs are compared over 10ns time windows to better show the accuracy of our measurements. The full width at half maximum (FWHM) of the TR spiral antenna is 70 ps, while for omni-directional antennas it is 160 ps. As we show in Fig. 3.7, the impulse response associated with the spiral antennas has stronger high frequency content compared to the omni-directional response (e.g., there is ~3dB difference around 10GHz). For TR experiments this difference is two times larger in a dB scale (Eq. (3.2)), which explains the FWHM differences of spiral and biconical antennas. The correlation coefficients between simulations and experiments are 0.9969 and 0.982 for these measurements.

The achieved gains by implementing the TR technique can be analyzed by considering the NLOS $C_{rms}$ and $G_9$ parameters in Table 3.1. For omni-directional antennas, TR performance is improved compared to the LOS scenario. Absence of an undistorted LOS component is the main reason for this improvement. However, although TR provides considerable PAPR gain, it still gives only several percent time compression. Again, this can be explained by considering the frequency response of the channel. The omni-directional received spectrum (Fig. 3.7) looks like the LOS one, but

Table 3.3: Summary of average PAPR and temporal compression gains presented in Table 3.2 for different environments and antennas. In this table, symbols "Y" and "N" represent presence and absence of an impulse response characteristic, respectively.

| | | Impulse Response characteristics | | TR Performance Parameters | |
|---|---|---|---|---|---|
| | Antenna Type | Strong dominant component in IR | Sharp fades in the spectrum | Temporal compression Gain $C_{rms}$ (%) | PAPR Gain $G_\vartheta$ (dB) |
| LOS | Omni-directional | Y | Y | -7.8% | 0.8dB |
| LOS | Spiral | N | N | 44.3% | 11dB |
| NLOS | Omni-directional | N | Y | 16.4% | 5.1dB |
| NLOS | Spiral | N | Y | 16.6% | 7.5dB |

with a faster decreasing slope. Spectral shaping effect of TR again opposes compression, but due to the absence of the undistorted LOS component (would strongly affect the spectral phase), the phase compensation aspect of TR results in better focusing compared to the LOS omni-directional scenario, and TR overall provides modest temporal compression.

For the spiral experiment, both gain parameters ($C_{rms}$ and $G_\vartheta$ ) are worse than the LOS scenario. To understand the reason, we compare the frequency response of the NLOS experiment in Fig. 3.7 with the corresponding LOS spectrum (Fig. 3.4). We can see there are several sharp fades in the NLOS frequency response, in addition to a faster decreasing slope compared to the LOS spectrum. As mentioned earlier, in spiral NLOS experiments, multipath interactions and the frequency response of obstacles between the antennas (like walls, doors, etc) become as important as the response of the antennas themselves, and lead to interference effects in the frequency response function. The resulting fades in the power spectrum and its faster descending slope are the main reasons for deterioration in TR performance compared to that observed for spiral antennas in a LOS configuration.

To observe more NLOS channel statistics, we moved the receiver over a rectangular grid, while the Tx is fixed during all experiments. Results of these experiments are presented in Table 3.2 under the NLOS section. In contrast to the LOS scenario, standard deviations of the metrics for spiral antennas are comparable to the corresponding omni-

directional values (caused by the presence of multipath effects in both NLOS links). The compression and PAPR gains for NLOS omni-directional antennas shows higher gains can be achieved compared to the LOS experiments, but still temporal compression gain is not significant. In general, implementing TR technique on single input single output (SISO) channels with omni-directional antennas does not considerably reduce RMS delay spread.

To conclude this section, average values of compression gains and PAPR gains for experiments presented in table 3.2 are summarized in table 3.3. Based on our discussions, there are two important factors which significantly affect TR performance: 1) Presence of a strong dominant component in the impulse response (usually an undistorted LOS component); 2) Presence of sharp fades in the transfer function of the channel and antennas. We can get the best performance in the LOS spiral antennas in the absence of these two effects, while the worst TR performance is for LOS omni-directional scenarios, where two effects exist concurrently. For NLOS experiments, presence of sharp fades is the only degrading factor, and an intermediate TR performance can be achieved for both antennas.

# 4. PHASE COMPENSATION COMMUNICATION TECHNIQUE AGAINST TIME REVERSAL FOR ULTRA-WIDEBAND CHANNELS

## 4.1. Introduction

As explained in the previous chapter, Time Reversal (TR) can be used [43, 54] to reduce receiver's complexity and suppress multipath dispersion to some extent. TR performance has been studied by several authors for UWB communications, in most cases with the TR simulated on the basis of measured impulse responses [46, 51, 52] or IEEE UWB channel models [55, 56]. In [51] Monsef et. al. used TR simulations, based on the impulse responses measured using a vector network analyzer over 600 MHz- 6 GHz, to show that although TR has good performance in highly reverberant media, it does not show the same effectiveness in realistic indoor environments. Naqvi et. al. [9] performed experiments in which they measured bit error rate (BER) of time reversal communication systems for different data rates in the range of 15.6 Mbps to 1 Gbps. They carried out experiments both in indoor and in reverberating chamber environments over the frequency range of 0.7-2.7 GHz. They showed BER is dominated by the intersymbol interference (ISI) effects for data rates above 125 Mbps. Simulations have also been used to investigate different schemes that could provide better performance compared to a simple TR system (especially at high data rate) [46, 52, 55, 57]. For instance, Naqvi et al. [9] introduced a modified TR scheme in which the total UWB bandwidth was divided into $N$ sub-bands. They used 10 different passband filters, and normalized the power of each band by using equal power controls (EPC). Although they achieved a slightly better BER in their modified TR system, this technique cannot flatten sharp fades of the frequency response and, from a practical point of view, adds complexity. In [52, 58], time reversal is used with the multiple-input single-output

(MISO) structure to get a better temporal compression. Oestges et al [46] compared TR performance with that of a minimum mean squared error (MMSE) prefilter and showed the channel ISI can be suppressed much more strongly by the MMSE prefilter. As they emphasized, the main drawback of MMSE is high implementation complexity which becomes difficult when the number of channel taps increases.

In the previous chapter, we showed although TR is a powerful technique for compensation of phase distortions associated with broadband frequency-independent antennas, it shows only modest performance in compressing time spread associated with multipath delay. Here, we introduce the phase compensation (PC) [59] prefilter as a solution to suppress ISI in UWB systems and investigate its performance experimentally over the frequency band spanning 2-12 GHz. To the best of our knowledge, this topic has not been reported in the previous literature on UWB communications. PC pre- and post-filters have been extensively used in optical communications and ultrafast optics, for example, [60, 61] . PC has also been previously used [40] to compensate distortion due to spectral phase variations of broadband frequency-independent antennas (e.g. Archimedean spirals) in a situation essentially free of multipath. In the ideal infinite bandwidth case, this is known as All-Pass filtering [62]. For PC the frequency dependent phase of the system response is extracted, and the excitation signals are designed to have the opposite spectral phase. In this way, PC can be seen as an equal gain transmission (EGT) [63] which is implemented in the frequency domain. In equal gain transmitters, which are commonly used in multiple antenna systems, transmitted signals from different antennas are passed through appropriate phase filters to arrive coherently at the receiver. Here, in phase compensation, the spectral phase of the transmit signal cancels the spectral phase distortion of the system response, resulting in a compressed waveform at the receiver.

A special emphasis of this chapter is to compare the capabilities of PC and TR prefilters over indoor UWB channels in different regards including temporal and spatial focusing. Temporal focusing means that the transmitted energy adds up coherently at the target receivers, leading to a single short peak with very low sidelobes. This peaking translates into a significant signal-to-noise ratio (SNR) advantage which can be used to

dramatically reduce the intersymbol interference in a high-speed wireless communication system. Spatial focusing means that the spatial profile of the received response decays rapidly away from the target receiver. This leads to low probabilities of intercept and multi-user interference. By exploiting the spatial focusing, one may publicly broadcast control information, yet still use this information to enable covert communication.

We report experiments in which we apply TR and PC prefilters to different measured channel realizations in Line-Of-Sight (LOS) and Non-Line-Of-Sight (NLOS) environments. We then calculate temporal compression and peak-to-average power ratio (PAPR) gains of these prefilters and investigate their sensitivity to the noisy channel estimation. To generalize the result beyond our own indoor environment and characterize channel hardening performances, we present simulations based on 1500 channels using IEEE 802.15.4a model. Our studies show that PC has superior performance in compressing UWB multipath dispersions. This point is theoretically proved, independent of any particular channel realizations, in terms of the PAPR gain. In another route to evaluate data transmission performances, bit error rates are simulated, based on our measured indoor impulse responses, for received signal-to-noise ratio (SNR) values in the range of -5 to 30 dB. Although TR systems show significant ISI for data rates of 500 Mbps and above (especially in NLOS), PC yields remarkably improved BER which can be used for high-speed transmission of data as fast as 2 Gbps. Finally, we experimentally investigate the spatial focusing capabilities of TR and PC in NLOS environments. Our study again confirms the superior performance of PC. In general, PC offers potential as a lower complexity (low computation cost due to the efficient FFT algorithm) alternative for similar prefilters (i.e. optimal MMSE) which have better performance compared to TR [64].

The remainder of this chapter is organized as follows. In section 4.2, we formulate phase-compensation and explore the similarities and differences compared to TR. In section 4.3, we explain the research methodology including the experimental and simulation procedure. Examples of the PC and TR measurements, in LOS and NLOS environments, and their performance evaluations based on experimental results and the

IEEE 802.15.4(a) (the most comprehensive model for UWB channels) are reported in section 4.4.

## 4.2. Phase Compensation Technique

In PC prefilters the channel is excited with the opposite spectral phase of the measured impulse response to compensate delay distortions of the system. The waveform transmitted under PC ($X_{PC}(f)$) and the resulting received response ($Y_{PC}(f)$) can be mathematically expressed in the frequency domain as:

$$X_{PC}(f) = \exp\left(-j.\arg\left(H_{sys}(f)\right)\right),$$ (4.1)

$$Y_{PC}(f) = H_{sys}(f).X_{PC}(f) = \left|H_{sys}(f)\right|,$$ (4.2)

Where $arg(H_{Sys})$ is the spectral phase of the measured impulse response of the system. Eq. (4.1) shows the power spectral density (PSD) of the PC prefilter does not depend on the channel transfer function. Eq. (4.2) indicates PC compensates the spectral phase of the system transfer function, and $Y_{PC}$ is equal to the magnitude of the $H_{Sys}$. Compared to the TR received response (Eq. (3.2)), PC does not square the spectral magnitude of the channel response (amplitude distortion aggravation), and as a result, intuitively a better temporal sidelobe suppression performance (e.g. temporal peak to average power ratio (PAPR)) should be achieved by PC technique. From a theoretical viewpoint, we show in the Appendix (A) that the PAPR value for PC always exceeds that for TR (equality only happens when we have a phase-only channel for which PC and TR become formally identical). The PAPR is commonly used as a physical performance indicator in wireless communication systems with pre-post equalizers.

From one point of view, TR and PC can be seen as counterparts to the maximum ratio transmission/combining (MRT/MRC) and equal gain transmission/combining (EGT/EGC) techniques [63, 65] which are well known in MISO systems and frequency domain equalizers. From another point of view, PC can be considered as an equalizer that is an intermediate choice between time reversal and zero forcing (ZF) [3, 64]. In particular, in the frequency domain the received response with PC is the geometric mean

of the received responses with TR and ZF, respectively. ZF prefilters, in an ideal case, have a frequency response equal to the inverse of the system transfer function, and are designed to completely compensate channel distortions (zero ISI). In ZF prefilters channel inversion consumes a huge amount of power when the system transfer function exhibits deep fades (when channel transmission is poor). This drawback makes the ZF prefilter costly for a realistic communication system where transmitters are usually limited by some power constraints [3]. In many respects (e.g. maximum received peak power, ISI elimination capability, peak to sidelobe ratio), the performance of PC is intermediate between TR and ZF. Although PC does not perfectly eliminate ISI, we experimentally show it can combat the UWB multipath channel dispersions more efficiently compared to TR. Although other prefilters with improved ISI suppression performance compared to TR have been proposed, PC has the potential advantage of lower implementation complexity. The computation cost of this prefilter is low due to the efficient FFT algorithm (with complexity $o(N \log N)$ where $N$ is the number of taps [66]) which is particularly important in UWB systems with large number of taps. However, the complexity is higher than for TR, which requires only flipping the channel IR. As an example of other proposed equalizers [64, 67], Kyrtsi et al [64] combined TR and ZF prefilters by using least squares criterion to design a prefilter with acceptable performance over different data rate regimes. Similar to the optimal MMSE prefilter [46] which requires matrix inversion with general complexity of $o(N^3)$ (a comprehensive study on computational complexity of different equalizers are presented in [66]), their prefilter is difficult to implement in a practical UWB system with large delay spread channels corresponding to high number of taps.

## 4.3. Research Methodology

### 4.3.1. Experimental Measurements

Here we employ the experimental setup explained in section 2.2. Experiments were carried out over the environment layout described in Fig. 3.1. For each antenna placement, the experimental procedure for TR/PC measurements consists of three steps

1) Channel sounding 2) Waveform calculation for TR/PC and communicating this with some predefined accuracy to the Tx side through the wireless LAN 3) TR/PC waveform transmission and measurement. Spread spectrum channel sounding, as discussed in chapter 2, is used for impulse response measurements. We use an up-chirp signal defined over 0-12 GHz with 85.3 ns time aperture at 24 GS/s sampling rate for channel excitation. To extract system impulse responses from the received waveforms, a deconvolution method is implemented. First, we record the sounding waveform without wireless transmission (AWG output is connected to the oscilloscope by an RF cable). Then, the received waveform after propagation through the channel and antennas is deconvolved from the sounding waveform.

In the next step, the TR/PC waveforms are calculated based on the measured impulse responses, and sent back through the feedback loop (wireless local area network) with 8 bit resolution to the transmitter side. The waveform calculation for TR consists of resampling the obtained impulse response at 24 GHz and inverting the result in time. For PC, we first used Eq. (4.1) to calculate the PC prefilter in the frequency domain, and then take Inverse Fourier Transform (IFT) to construct the time domain PC waveform for generation by AWG. Finally, these signals are transmitted through the channel, and the received waveforms are recorded using the real-time oscilloscope.

### 4.3.2. Simulation Procedure

Since our measured channel responses are almost noise free [48], we use simulation to analyze the noise sensitivity of PC and TR. We add white Gaussian noise to the measured channel realizations and calculate these prefilters based on the noisy channel responses. Then, the temporal compression and PAPR gain performances are evaluated as a function of SNR (defined as the average channel response power to the average noise power in dB scale over ~170ns time window) over -5 to 25 dB in steps of 0.5 dB. The final performance curves are finally plotted based on the average results of the 15 NLOS channel realizations.

To assess the performance of TR and PC in high-speed data transmission, we simulate their BER performance. The simulation is based on transmitting $10^7$ random bits

using BPSK (Binary Phase Shift Keying) modulation over the measured channel realizations. We use TR and PC prefilters for combating the multipath channel dispersion. On the receiver side, we sample the received signal at the peak of PC/TR and make our decision based on the maximum-likelihood criterion [3]. We assume the receiver to be perfectly synchronized with the transmitter. Simulations are performed as a function of the received SNR (defined as the maximum received peak power to the noise power in dB scale) over -5 to 30 dB in steps of 1dB for data rates ranging 125Mbps to 4Gbps. The average BER performances are evaluated by averaging the BER of the 15 channel realizations for LOS and 15 channel realizations for NLOS.

We also compare the performance of PC and TR over the IEEE 802.15.4(a) standard, a comprehensive UWB channel model. In these simulations, we have used the statistical parameters presented in Table I of [53] for indoor NLOS residential environments.

## 4.4. Measurement Results and Analysis

### 4.4.1. Temporal Focusing of Phase Compensation versus Time Reversal

#### 4.4.1.1. Line of Sight Environment

Figure 4.1(a) shows the impulse response of a specific (but typical) LOS omni-directional antenna over 200 ns time window. The received response consists of different multipath components which extend up to ~100 ns time window. More details about IR characteristics measured by omni-directional antennas are presented in chapter 2. To mitigate the multipath effects, we implement TR and PC prefilters. Experimental TR and PC received responses are compared in Fig. 4.1(b)-(c). A key point is that as we can clearly see, sidelobes for PC are considerably smaller compared to those for TR.

We repeated LOS IR, TR and PC measurements over a rectangular grid to observe more channel realizations. In table 4.1, we summarize average and standard deviation values of the introduced metrics for these measurements under the LOS section. Average full width half maximum (FWHM) durations of the PC and TR responses are, respectively, 80 ps and 121 ps. The larger FWHM duration observed for TR arises because the received signal falls off more rapidly with frequency due to the squaring operation in Eq. (3.2). The average PAPR for TR and PC are increased, respectively, by
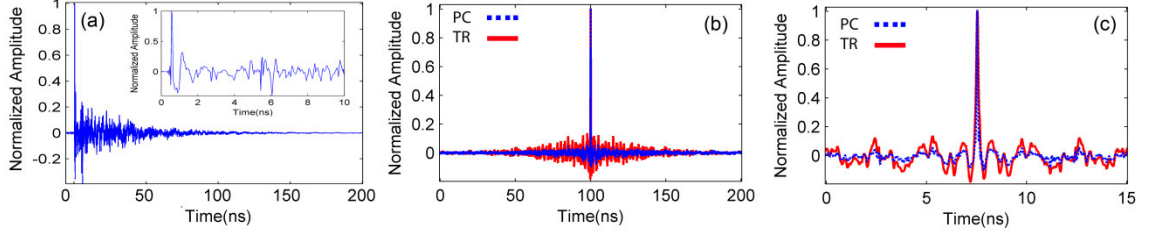
Fig 4.1: (a) Impulse response of LOS omni-directional antennas over 200 ns time window. In the small subfigure, we zoom in on the first 10ns of the response. (b) Received responses from TR and PC experiments implemented over the channel. (c) We zoom in on the main peak to show details. PC sidelobes are considerably smaller compared to the TR response.

1.05 dB and 4.4 dB compared to the IR-PAPR. For TR, the small PAPR gain ($G_\vartheta$ =1.05dB) indicates TR does not significantly improve the PAPR value. The presence of the dominant LOS component, which is essentially subject to no spectral phase variation, is one of the reasons for this performance. PC-RMS delay is more than two times less than the IR-RMS, while for TR it is increased by 7.2%. The negative temporal compression gain ($C_{rms}$= -7.2%) implies single-input single-out (SISO) TR cannot decrease the RMS delay spread of the channel, which is consistent with the predicted results by simulations in [52]. The broadening effect of SISO-TR (squaring the spectrum magnitude) counteracts and may even exceed the compression effect (spectral phase compensation); overall, TR does not reduce the RMS delay spread of the channel (Please see chapter 3 for more details). However, for PC prefiltering spectral phase compensation is the only effect present, and the observed compression gain is significantly larger. In short, PC not only in average reduces RMS delay of the channel to 49% of its original value, but also gives a 4.4 dB PAPR gain.

The simulated BER performance averaged over the LOS realizations discussed in Table 4.1 are presented in Fig. 4.2. As we can see, for low SNR regime (<5dB), the system performances are determined by the dominant noise level, and both PC and TR have high BERs. Intersymbol interference becomes more important for higher SNRs. BER curves for the TR prefilter reach a plateau for data rates of 500 Mbps and above, where increasing the SNR cannot improve the performance any further. In this situation, the system performance is saturated by the ISI originating from TR sidelobes [46]. For

Table 4.1: Average (Avg) and standard deviation (Std) values for omni-directional experiments over 15 LOS and 15 NLOS locations. In the text, we refer to impulse response metrics by "IR-Metrics Name". TR and PC notations are respectively used for time reversal and phase compensation metrics.

| | | RMS delay σ (ns) | | PAPR ϑ (dB) | | FWHM (ps) | | Temporal Compression Gain $C_{rms}$ (%) | | PAPR Gain $G_\vartheta$ (dB) | |
|---|---|---|---|---|---|---|---|---|---|---|---|
| | | Avg | Std | Avg | Std | Avg | Std | Avg | Std | Avg | Std |
| LOS | IR | 14.4 | 0.9 | 29.4 | 1.2 | - | - | - | - | - | - |
| | TR | 15.4 | 1.5 | 30.4 | 0.6 | 121 | 7.2 | -7.2 | 10.3 | 1.05 | 1.0 |
| | PC | 7.0 | 2.1 | 33.79 | 0.2 | 80 | 2.6 | 51.2 | 15.1 | 4.4 | 1.1 |
| NLOS | IR | 19.9 | 1.3 | 19.15 | 1.46 | - | - | - | - | - | - |
| | TR | 16.7 | 1.6 | 26.6 | 0.67 | 202 | 17 | 15.8 | 7.8 | 7.46 | 1.2 |
| | PC | 6.2 | 1.4 | 31.3 | 0.24 | 119 | 8.6 | 69.0 | 6.03 | 12.13 | 1.3 |
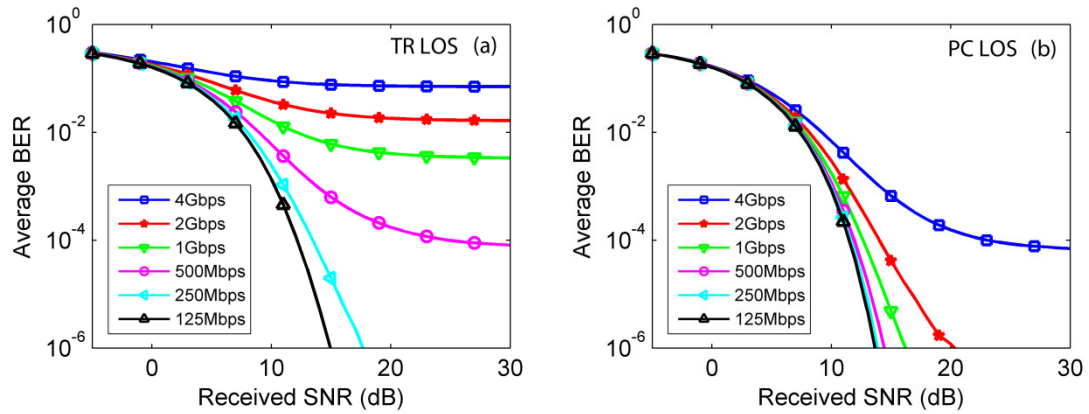


Fig 4.2: Average Bit Error Rate (BER) for LOS PC and TR. The performance of PC is clearly superior to that of TR in the high data rate regime (500Mbps and above).

the PC prefilter, we have the performance saturation only for the highest (4 Gbps) data rate transmission. This curve levels off at $10^{-4.1}$ BER which is by far better compared to the $10^{-1.1}$ level of the BER plateau of the 4 Gbps TR curve. Although TR and PC curves are close to each other for the low data rate transmission of 125 Mbps, for higher data rates the performance of PC is considerably superior to the TR technique. For instance, the BER for 2 Gbps data rate with PC is below $10^{-4}$ for SNR values larger than 14 dB;

however, with TR this curve reaches a floor at $10^{-1.7}$ BER, and better performance cannot be achieved.

### 4.4.1.2. Non-Line-of-Sight Environment

Fig. 4.3(a) shows an impulse response of a typical NLOS channel over a 200 ns time window. Unlike Fig. 4.1(a), no strong dominant component exists in the channel response. The greater distance and the presence of two cement walls between Tx and Rx lead to an increased number of resolved multipath components and greater high frequency attenuation compared to the LOS scenario discussed earlier. We implement TR and PC prefilters and compare the resulting responses in Fig. 4.3(b)-(c). We can clearly see significant superior sidelobe suppression can be achieved using PC prefiltering compared to TR in NLOS UWB channels.

NLOS channel statistics, obtained by moving the receiver over a rectangular grid as described in section 3.2.1, are tabulated in Table 4.1. This table reconfirms the strength of PC in combating the multipath dispersions. The FWHM of the PC and TR responses are, respectively, 119 ps and 202.5 ps. These values are larger compared to the corresponding LOS values which is consistent with increased loss for the higher frequencies. The TR and PC performances are improved compared to the LOS scenario. For instance, the PAPR gains are respectively ~ 6.4dB and ~7.7 dB higher for NLOS TR and PC compared to the corresponding LOS values. Absence of the undistorted LOS component is the main reason for this improvement. However, although TR provides PAPR gain, it still gives
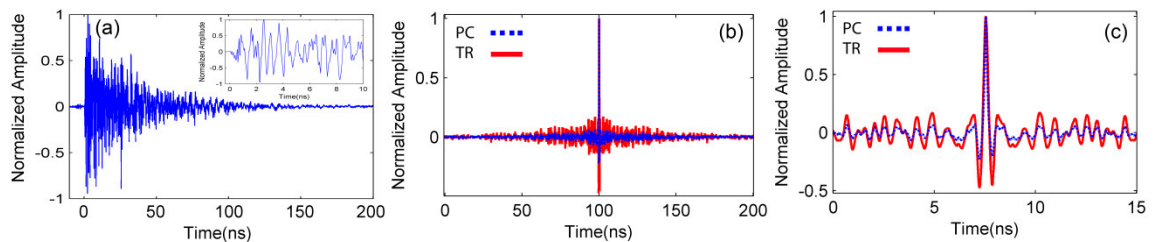


Fig 4.3: (a) Impulse response of NLOS omni-directional antennas over 200 ns time windows. In the small subfigure, we zoom in on the first 10ns of the response. (b) Received responses from TR and PC experiments implemented over the channel presented in (a). (c) We zoom in on the main peak to show details. PC sidelobes are considerably smaller compared to the TR response.

only modest time compression. The RMS delay of PC is 69% shorter and its PAPR value is 12.13 dB larger than the corresponding NLOS IR values. These values for the TR are only 15.8% and 7.46 dB which again point to superior multipath delay compensation using the PC technique.

To evaluate capabilities of PC versus TR beyond our indoor environments, we compare their performance based on 1500 simulated channels using CM2 IEEE 802.15.4a model (NLOS indoor residential environments) [53]. Figure 4.4 shows the cumulative distribution function (CDF) of (a) the RMS delay and (b) the PAPR for IR, TR and PC. Both prefilters provide PAPR gain as well as channel hardening, i.e., reduction of PAPR variations in terms of 10%-90% rise of the CDF. However, PC gives rise to significantly better gain and channel hardening. In terms of RMS delay, PC provides both compression and channel hardening (though much less hardening than is achieved for PAPR). For TR the compression is minimal, and no hardening is apparent. In both cases the simulated temporal compression is smaller than observed experimentally. This difference can be explained by the fact that IEEE 802.15.4a does not take into account important propagation effects like distance dependence, random variation of the path loss exponent, and frequency dependence of the path gain [53]. This point shows the importance of experimental implementations.
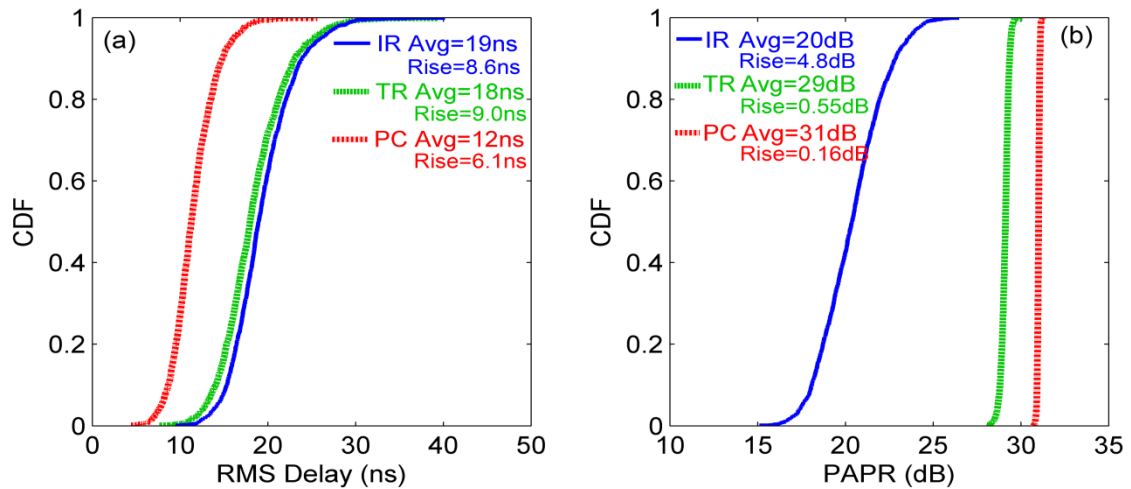


Fig 4.4: Cumulative Distribution Function (CDF) for (a) RMS delay and (b) PAPR plotted based on 1500 channel impulse responses simulated using the IEEE 802.15.4(a) model.On each figure, we show the corresponding average values (Avg) and the 10%-90% rise of the CDF (Rise) for IR, TR and PC.
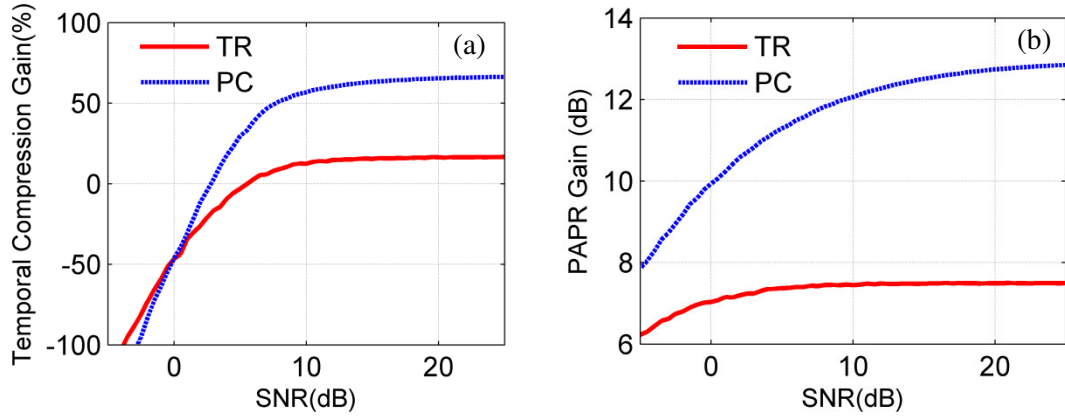
Fig 4.5: Noise sensitivity for NLOS PC and TR (a) Temporal Compression Gain. (b) PAPR gain.
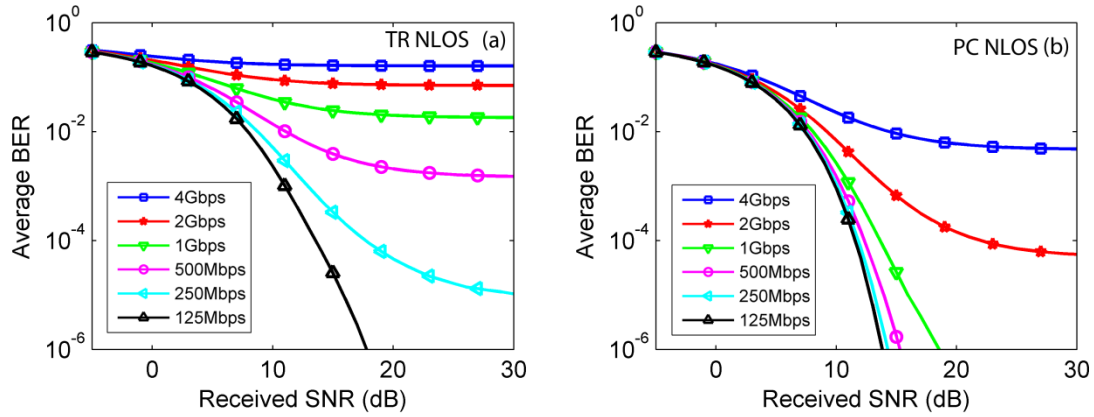


Fig 4.6: Average Bit Error Rate (BER) for NLOS PC and TR. The performance of PC is clearly superior to that of TR for the data rates of 250 Mbps and above.

The sensitivity of prefilter performance to errors in the estimated channel response has been studied for TR in [53]. Using the simulation procedure outlined in section 4.3.2, here we compare the performance of PC and TR prefilters as a function of the signal to noise ratio in the channel response estimation. Figure 4.5(a) shows both prefilters actually increase the RMS delay in low SNR regimes. Temporal compression is achieved for SNRs larger than 2.6 dB and 5.5 dB respectively for PC and TR. The PAPR gain performance is compared in Fig. 4.5(b). Although PC is more sensitive to additive noise (its gain drops faster as the SNR decreases), it always provides superior PAPR gain compared to TR.

The simulated BER performance of NLOS PC and TR prefilters, averaged over the channel realizations discussed in the NLOS section of Table 4.1, are presented in Fig. 4.6. Comparing Fig. 4.6 and Fig. 4.2 shows both NLOS PC and NLOS TR responses have inferior BER performances compared to the corresponding LOS scenarios. This can be explained by the fact that NLOS responses have narrower effective bandwidths. This effect is especially important for TR prefiltering for which the frequency rolloff is twice as large in a dB scale (Eq. (3.2)). As we see in Fig. 4.6(a), TR BER curves exhibit error floors for data rates of 250 Mbps and above, for which ISI saturates system performance. For PC in Fig 4.6(b), 2 and 4 Gbps curves level off, respectively, at $10^{-4.25}$ and $10^{-2.3}$ which are considerably better compared to the attained plateau by the corresponding NLOS TR curves ($10^{-1.15}$ for 2Gbps and $10^{-0.79}$ for 4 Gbps). In general, PC prefilters have substantially superior performance compared to TR. For instance, BER of 1Gbps PC is below $10^{-4}$ for SNR larger than ~13 dB; however, for TR technique, this curve floors at $10^{-1.74}$ and better performance cannot be achieved.

### 4.4.2. Spatial Focusing of Time Reversal versus Phase Compensation

In strong multipath channels, if two receivers are spaced more than few wavelengths (one wavelength equals ~3 cm for 10 GHz center frequency), their impulse responses are expected to be strongly uncorrelated [17]. As a result, in addition to the temporal focusing which compresses the channels' energy into one central peak, beamforming (TR, PC, etc) also provides spatial focusing. Spatial focusing means the received response peaks at the target receiver and decays rapidly as we move away. As discussed later, this selective peaking in a specific transmit-receive antenna link can be exploited to achieve covert wireless data transmission.

The experimental procedure to characterize the spatial focusing consists of two steps. First, we measure the channel impulse response from the Tx to the target receiver which is located at the center of an automatic antenna positioner. We apply TR/PC beamforming based on the measured impulse response and record the received response. In the next step, we move the receive antenna with the step size of 2 cm on a 1m×1m square grid and measure the received peak values as we move away from the center
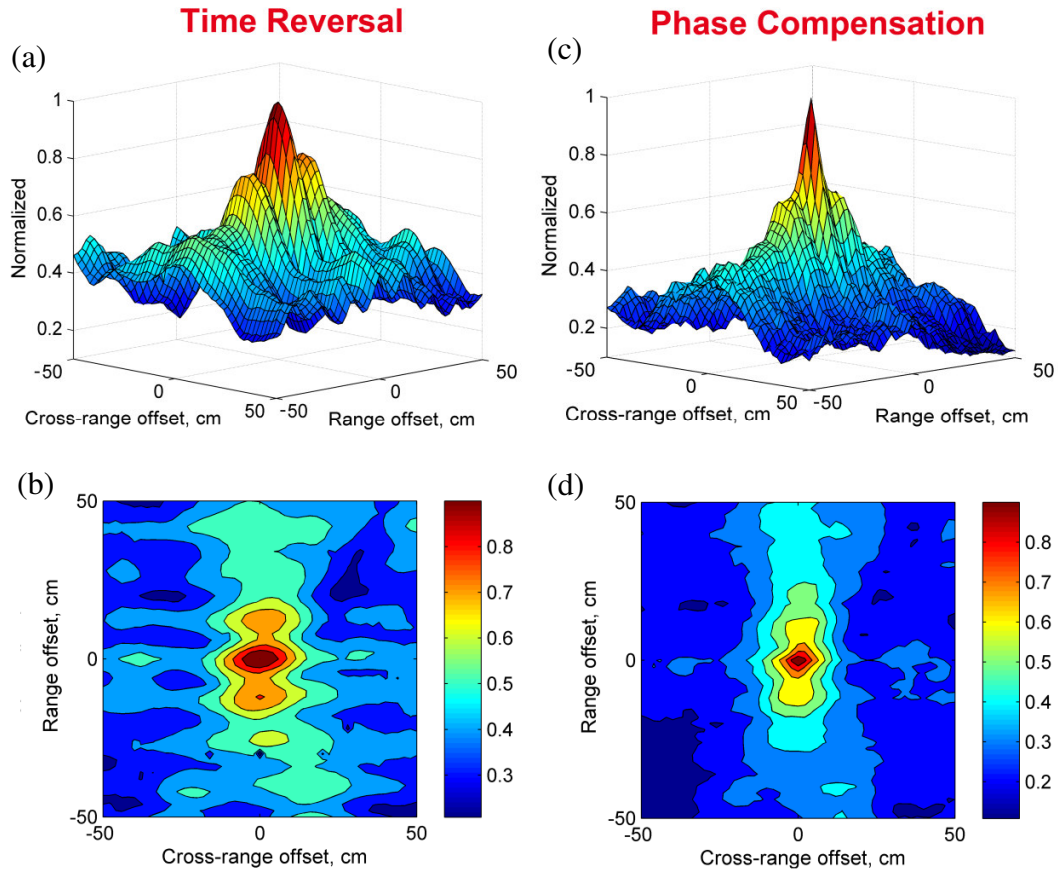
Fig 4.7: Spatial focusing of (a-b) TR and (c-d) PC in a NLOS environment with ~15 m propagation distance.

location. The experimental results for a NLOS environment with propagation distance of ~15 m are presented in Fig. 4.7. Figure 4.7 (b) and (d) are different views of Fig. 4.7 (a) and (c), respectively. In these figures, we define range as the direction from the Tx to the Rx antenna. Cross-range is perpendicular to the range direction.

For both TR and PC, the spatial focusing rolls off faster in the cross-range direction. In the range direction, there are two sidelobes in addition to the approximately symmetric central peak. As predicted by simulation in [46], structure of these peaks depends strongly on the environment geometry. Overall, PC provides a better spatial focusing compared to the TR. For instance, the signal level of PC falls below 3 dB with respect to the main central peak after ~10 cm offset in the cross-range direction; however, this number for TR is ~36cm.

As an intriguing example of the opportunities available from the spatial focusing, consider the following experiment which has been conducted to achieve selective peaking at the target receiver. Two Rx antennas are located 50 cm away from each other (Rx1-Rx2) in a NLOS environment in respect to the Tx. Fig. 4.8 (a),(b) show impulse responses of these two channels over the frequency range of 2-12 GHz. The impulse
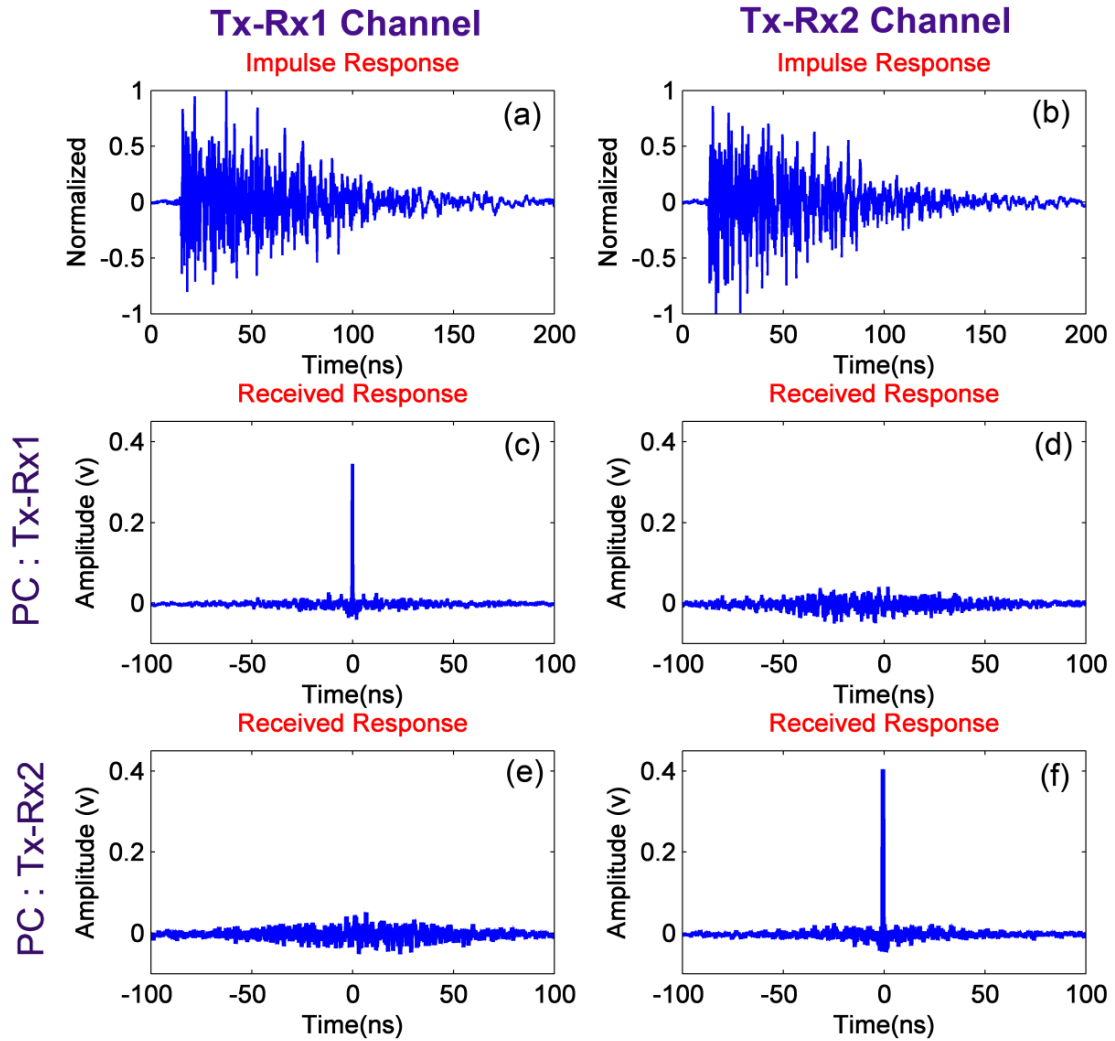


Fig. 4.8: (a-b) Channel impulse response between Tx-Rx1 and Tx-Rx2. (c-d) Received responses at Rx1 and Rx2 whe transmitted waveform is matched to the channel Tx-Rx1. (e-f) Received responses at Rx1 and Rx2 when transmitted waveform is matched to the channel Tx-Rx2.

responses exhibit strong multipath dispersions up to ~150 ns, which is spread more than 1000 times compared to the fundamental time resolution <100 ps. Due to the strong multipath scattering, the impulse responses are nearly uncorrelated although the delay spreads are similar. With knowledge of the channel impulse responses, Tx may transmit a PC waveform matched to the Tx-Rx1 multipath channel which results in significant peaking at the target receiver (Rx1), Fig. 4.8 (c). The interesting point is that because of the spatial diversity of UWB multipaths, the Rx2 which is located a few wavelengths away from the intended receiver (Rx1) gets a noise like waveform similar to Fig. 4.8(d) which provides a basis for covert communications. In a similar way, when the Tx transmit PC waveform to achieve peaking at Rx2 (Fig. 4.8 (f)), the received pulses by Rx1 are a series of noise like pulses (Fig. 4.8 (e)). To our knowledge these are the first successful experiments of this kind that cover the whole UWB band.

In conclusion in this chapter, we investigated the phase compensation (PC) prefilter as a solution to suppress multipath dispersion in UWB systems. Our results suggest that the PC prefilter has the potential to be used in high-speed covert UWB communication channels as an effective way to combat channel multipath dispersions, provide channel hardening and spatio-temporal focusing.

# 5. EXPERIMENTAL TEST-BED FOR STUDYING MULTIPLE ANTENNA BEAMFORMING OVER ULTRA WIDEBAND CHANNELS

## 5.1. Introduction

In recent years intensive research has been performed to explore the opportunities of multiple antenna systems in connection with sophisticated transmit beamformings (e.g. TR or Minimum Mean Square Error (MMSE)) over the UWB channels [46]. Transmit beamforming shifts receiver complexity to the transmitter side and provides temporal and spatial focusing, which reduce respectively inter-symbol interference (ISI) in high speed wireless communications and inter-channel interference in multiple user networks. In addition, multiple antenna systems have been exploited to extend the UWB transmission range [52] and to achieve increased information rate and better spatial focusing and temporal compression compared to that possible with a single transmit-receive antenna pair [46, 52, 68-73].

Much of the previous research in multiple antenna systems for UWB is theoretical and based on simplified models [46, 52, 68-70] which do not address experimental challenges such as imperfect channel estimation or transmitter synchronization and antenna coupling. For example, in [46, 52, 68, 69] TR performance of Multiple-Input Single-Output (MISO) systems is studied based on simulations by computing auto- and cross-correlations of the measured impulse responses (IR). This gives a prediction of MISO-TR capabilities when the measured data are noise free and the estimated IRs are perfectly accurate. A few researchers have studied UWB MISO systems experimentally by applying transmit beamforming (particularly TR in most cases) [71-73]. In [71, 72], FPGA boards are used to test MISO-TR systems for two transmitters at a center frequency of 3GHz, with bandwidth specified as 800 MHz at -10 dB. Naqvi et al [73]

used an arbitrary waveform generator (AWG) to study TR in a two transmit antenna configuration in a reverberation chamber over the frequency range of 0.7-2.7 GHz. These studies either cover only a small portion of the UWB or are completely out of the 3.1-10.7 GHz band.

The lack of comprehensive experimental measurements over UWB multiple antenna systems has motivated us to extend our work to implement an experimental setup capable of testing the performance of different transmit beamforming designs in multiple antenna configurations over the frequency range of 2-12 GHz. To the best of our knowledge, this is the first experimental report of multiple antenna beamforming over the full UWB band. Implementation of our setup is based on using optical fiber delays to apply appropriate time shifts to the output of an electrical AWG. Although optical delay lines have been extensively reported for true-time-delay feeds of phased array radar antennas [74] over large bandwidth, our work is the first to apply fiber delay lines for UWB multiple antenna beamforming. Although this setup can be extended to study the performance of arbitrary number of transmit antennas in connection with any sophisticated beamforming design, we introduce it in detail by implementing a 4×1 MISO configuration. The emphasis of the current chapter is to demonstrate the viability of our setup and assess its experimental accuracy in applying beamforming.

The remainder of this chapter is organized as follows. Section 5.2 provides details of the physical measurement setup. Section 5.3 describes our measurement methodology and examples of the experimental results.

## 5.2. Experimental Setup

Fig. 5.1 shows a block diagram of the measurement setup. Tektronix arbitrary waveform generator 7122B is used in interleaving zeroing-on mode which gives the maximum available sampling rate of 24GS/s. The AWG not only provides sufficient bandwidth to probe channels over a frequency band spanning 2-12 GHz, which exceeds the full FCC UWB band, but also provides the flexibility to implement different transmit beamforming algorithms. Its main limitation is that only one output is operational in
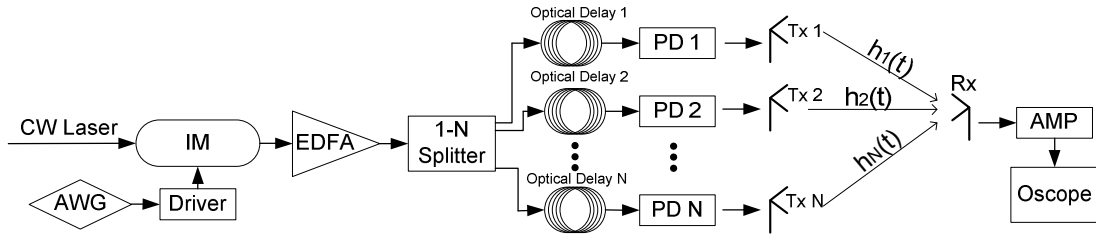
Fig 5.1: Block diagram of the measurement system. CW laser: Continuous wave laser, AWG: Arbitrary waveform generator, IM: Intensity modulator, PD: Photodiode, Tx: Transmit antenna, Rx: Receive antenna.

interleaving mode, which would normally suffice only for testing of single transmit antenna configurations [48, 49, 75, 76]. To extend the capabilities of the AWG to study multiple antenna systems, we propose a photonic solution which exploits the long recordlength of the AWG (up to 64M points). The main concept is to use the AWG to generate a sequence of waveforms (e.g., TR signals for different channels in a MISO configuration) with relative delays which are longer than the maximum delay spread of the wireless channel. The electrical signal from the AWG is mapped to the optical domain and split to drive different photodiodes (PD) which are connected to the transmitting antennas. The individual transmit waveforms are aligned in time using optical fiber delay lines such that they arrive at the receiving antenna in synchronism. In this way we can concurrently excite different antennas with different transmit waveforms by using a single AWG.

Back to our setup in Fig. 5.1, to accomplish this idea, the output of AWG is amplified by a driver amplifier (Picosecond Pulse Labs Model 5865) which has 12 GHz bandwidth and maximum 26 dB small signal gain. A commercial lithium niobate intensity modulator (IM) is used [38] to create an optical intensity that mirrors the electrical output of the AWG. A continuous-wave (CW) optical signal at 1.55µm wavelength is directed into the IM with DC electrical bias adjusted precisely for 3dB transmission and with the driver output connected to the RF input of the IM (Fig. 5.1). There is a trade-off between the dynamic range of the modulated optical waveform and the nonlinearity introduced by the sinusoidal response function of the IM, which should be considered to have an appropriate electronic to optical mapping. In our current

experiments, we have used maximum modulation depth of ~75%. The output of the IM is boosted by an erbium-doped fiber amplifier (EDFA Pritel SPFA-18) placed immediately before an optical splitter which ideally divides the incoming beam into $N$ equal beams. Each output of the splitter is delayed appropriately by passing through a fiber delay line and converted back to the electrical domain using a photodiode (bandwidth > 12.3 GHz). In our current setup, we use a 1×4 splitter and directly connect the PD1 to the 1$^{st}$ splitter output. Approximate delays of 600 ns, 1200 ns and 1800 ns are respectively applied to the 2$^{nd}$, 3$^{rd}$ and 4$^{th}$ outputs of the splitter. The relative delay increment of ~600 ns is much longer than the maximum delay spread of the channel (~200 ns). With optical amplification the electrical signals out of the PDs have ~0.4V peak to peak amplitude (e.g. Fig. 5.2) and are large enough to directly drive the antennas for impulse response sounding without electrical amplification. Wideband omni-directional antennas (ELECTRO-METRICS EM-6865 2-18 GHz) which have vertical polarization and uniform radiation pattern in the azimuth plane are used as transmitters (Tx) and receiver.

The output from the Rx antenna is passed through a low noise amplifier with 0.1-20 GHz frequency response and a minimum 31dB gain. The amplified signal is directly connected to a real-time oscilloscope (Digital Serial Analyzer, Tektronix DSA 72004B) with 20 GHz analog bandwidth and maximum real-time sampling rate of 50 GS/s. The oscilloscope is triggered by one of AWG's digital "marker" outputs which is synchronized with the transmitted waveform with timing jitter below 30 ps.

Although, we have conducted our experiments in several line-of-sight (LOS) and NLOS environments, in this chapter the measurement methodology is explained over a specific but typical 4×1 MISO indoor NLOS channel. The average propagation distance between Tx antennas and the receiver (Rx) is 14 m and there are two walls and a storage room (which contains large metallic desks and cabinets) in the direct paths of the Rx-Tx antennas. To show the accuracy of our setup by comparing the experimental results with the simulations, we place the transmitting antennas with the minimum inter-element distance of 70 cm to avoid coupling effects between them. This distance is also sufficient to have approximately decorrelated channels (i.e. correlation coefficients between  MISO
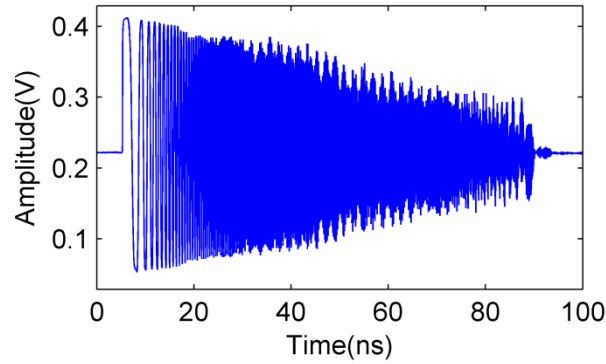
Fig 5.2: Generated chirp waveform out of PD1. This waveform is used as a reference for applying post-processing deconvolution to extract impulse responses.

channels are on the order of 0.15) which is necessary to get spatial-temporal focusing gains in addition to power gain in a MISO system [68].

## 5.3. Measurement Methodology and Experimental Results

Here we discuss the methodology and present experimental results first for the impulse response measurement and then for multiple-antenna beamforming.

### 5.3.1. Channel Impulse Response Measurement

We perform spread spectrum channel sounding to characterize impulse responses [48]. The main advantage of spread spectrum sounding is that the excitation waveform has low peak-to-average ratio and higher levels of total transmitted power compared to ultrashort pulse excitation which results in higher dynamic range. In these experiments a linear up-chirp waveform defined over DC-12 GHz with 85.3 ns time aperture at 24 GS/s frequency rate is used for sounding. After the AWG is programmed for the chirp waveform, we first perform a calibration measurement in which we measure the waveforms after the PDs by directly connecting it to the real-time oscilloscope. Fig. 5.2 shows the recorded signal out of PD1, which is used as a reference signal in the post-processing method to extract IRs. Other PDs also have similar outputs with relative time shifts due to the optical delay lines. The roll off of the chirp waveform in time simply reflects the frequency response of the AWG, driver and IM. There is a DC bias in the

output waveforms of the PDs (waveforms generated in photonic domain are always positive), which will be filtered by the high-pass characteristic of the antennas.

We excite the MISO channel with the chirp waveforms and record the received response by the oscilloscope (see Fig. 5.3). The received waveform consists of 4 separate parts corresponding to MISO channels $h_1(t)$-$h_4(t)$. A single scope trace contains
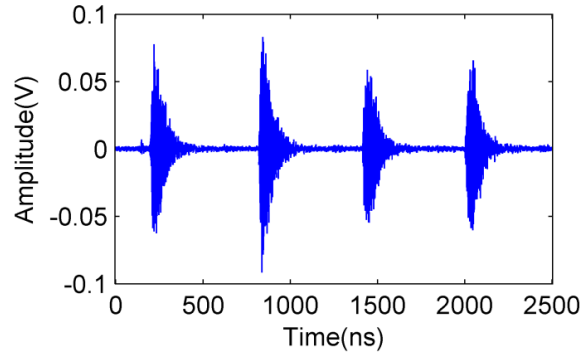


Fig. 5.3: Received response from channel excitation for MISO experiments.
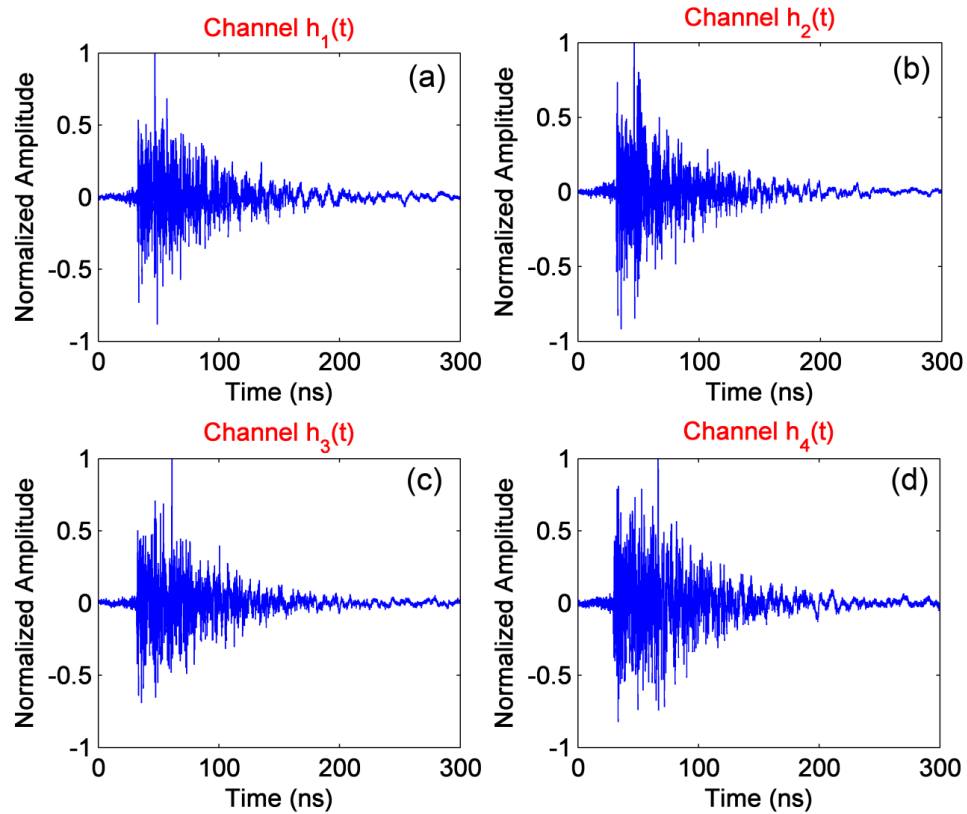


Fig. 5.4: Measured impulse responses from $h_1(t)$, $h_2(t)$, $h_3(t)$ and $h_4(t)$ links.

the impulse response information of all four channels, including relative delays due to the optical delay lines and propagation times (different channels have slightly different propagation distances).

To extract impulse responses from the received waveforms deconvolution is applied between the recorded reference waveform (Fig. 5.2) and the received response (Fig. 5.3). In this way, modulations of the transmitted power spectrum due to the system imperfections (e.g., frequency response of the AWG or nonlinearities of the IM) are compensated, and unbiased estimations are acquired. More details about our method, including assessments of its accuracy, are presented in chapter 2 [48]. Fig. 5.4 show the measured multipath impulse responses corresponding to the links $h_1(t)$ - $h_4(t)$. As we can see, the multipath components are distributed over time up to ~150 ns [75]. Due to strong multiple scattering, the IRs from the different Tx antennas are nearly uncorrelated (correlation coefficient of ~%15), although the delay spreads are similar.

### 5.3.2. Multiple Antenna Beamforming Experiment

After measuring the impulse responses, we can experimentally apply any arbitrary beamforming. Here we explain the procedure in detail with TR. The waveform calculation for TR consists of resampling the obtained IRs at 24 GS/s and inverting the result in time. The beamforming process is depicted schematically in Fig. 5.5. Each symbol represents a time reversed version of the IR from one of the Tx antennas. The overall waveform arrives at the various PD outputs with different delays. The dotted rectangle indicates the time period during which all antennas are excited simultaneously.
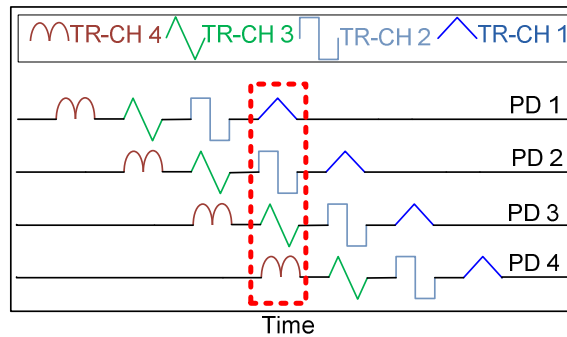


Fig 5.5: The AWG waveform shows up with different delays at the PD outputs. The time slot depicted by a dotted rectangle shows the period during which all antennas are excited simultaneously.
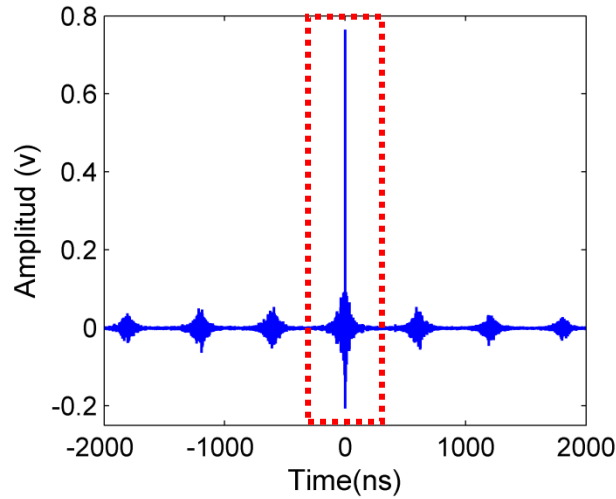
Fig 5.6: Received response from MISO-TR beamforming experiment. Time Reversal in the MISO configuration is achieved during the time period depicted by a dotted rectangle. The extra waveforms outside the dotted rectangle result in lower amplitude, noise-like responses at the Rx and are clearly separated in time from the main signal.

Beamforming in the MISO configuration is achieved during this time period, resulting in a strong peak at the Rx. The extra waveforms outside the dotted rectangle result in lower amplitude, noise-like responses at the Rx and are clearly separated in time from the main signal, Fig. 5.6.

Fig. 5.7(a)-(b) shows an example of the Rx response in MISO-TR beamforming experiments over two different time windows. The data are compared with the simulated response, equal to the sum of the autocorrelations of the measured impulse responses, $h_1(t)$-$h_4(t)$, timed such that the autocorrelation peaks are exactly synchronized. We can see data and simulation are extremely close. In this example the correlation coefficient between experimental and simulated traces is 0.98. This high level of agreement shows our accuracy both in measuring impulse responses and in aligning the received peaks in the MISO configuration. The full width at half maximum (FWHM) of MISO-TR is ~250 ps. Comparing Fig. 5.4 and 5.7(a)-(b) demonstrates that significant compression is achieved by implementing MISO TR. The peak to average power ratio (PAPR), measured over 200 ns time window, for the MISO TR response is ~12 dB higher than for the uncompressed impulse responses (Fig. 5.4).
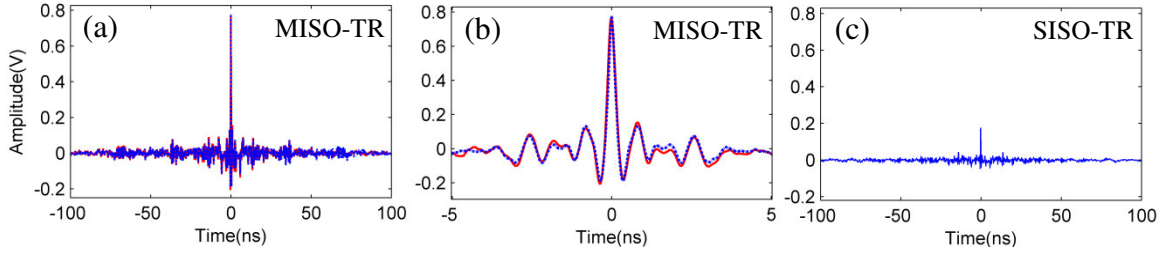
Fig 5.7: Comparison between Time Reversal simulations and experiments for omni-directional 4×1 MISO in NLOS environment. (a) 200ns time window. (b) Zoom in on the main peak. (c) Experimental SISO-TR over $h_1(t)$.

To show an example of the achieved array gain and better temporal focusing of MISO systems compared to SISO, we turned off the transmitted TR signals from PD2, PD3 and PD4 and leave the PD1 unchanged. The received response from applying SISO-TR over $h_1(t)$ is shown in Fig. 5.7(c). As we see from these figures, an amplitude gain factor of ~4.3 (peak power gain of 12.6 dB) is achieved in the MISO experiment, roughly as expected for a four antenna system. The PAPR for Fig. 5.7(a) is ~2.4 dB higher than for the SISO-TR shown in Fig. 5.7(c), which shows better sidelobe suppression of MISO configuration compared to SISO.

In a similar way, we can employ this experimental test-bed to explore MISO-PC over the UWB channels. Fig. 5.8 shows the received response from applying MISO-PC over the UWB channels shown in Fig. 5.4. The full width at half maximum of the MISO-PC is less than 160 ps. The peak to average power ratio (PAPR) for the MISO-PC
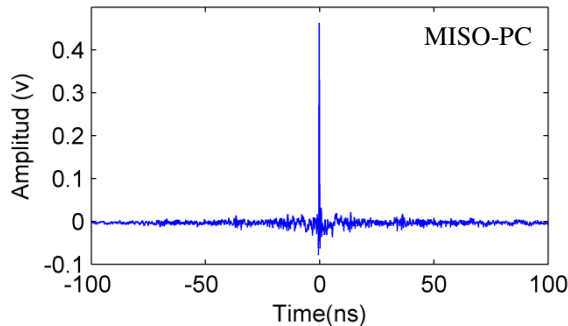


Fig 5.8: Received response from MISO-PC experiment. The peak to average power ratio (PAPR) for the MISO-PC response is ~16 dB higher than the uncompressed impulse responses.

response is ~16 dB higher than the uncompressed impulse responses (Fig. 5.4). Comparing performance of MISO-PC with the MISO-TR shows PC considerably outperforms TR in mitigating multipath dispersions. The achieved PAPR for MISO-PC is ~4 dB larger than the corresponding value for MISO-TR. The FWHM of MISO-PC is also ~90 ps smaller than the FWHM of MISO-TR.

We performed several channel measurements and beamforming experiments over the frequency range of 2-12 GHz for distances ranging between 10-17 m for NLOS channels and 3-7 m for LOS channels to study the repeatability and accuracy of this setup. All measurements show accuracy comparable to the example presented in this chapter. The excellent accuracy of this setup makes it highly appropriate for practical investigations of different topics including temporal-spatial focusing, waveform design and polarization multiplexing over UWB channels for multiple antenna systems.

# 6. MICROWAVE PHOTONICS FOR SPATIO-TEMPORAL COMPRESSION OF ULTRABROADBAND SIGNALS THROUGH WIRELESS CHANNELS

## 6.1. Introduction

One of the key limitations of UWB systems is the generation and distribution of ultrabroad waveforms. Due to limits associated with digital-to-analog convertors, electronic AWGs have a restricted RF bandwidth. Although recently offering increased bandwidth approaching 18 GHz, electronic solutions suffer large timing jitter and may be difficult to deploy in harsh environments characterized for example by high electromagnetic interference (EMI). To overcome these limitations, there have been substantial efforts in recent years to merge optical and wireless systems, a technology known as radio-over-fiber [77]. Optical systems [78-84] are generally immune to EMI, provide ultrabroad bandwidth and support remoting application by taking advantages of low loss brodbandwidth optical fibers [77, 79, 80, 85, 86]. However, most previous works on radio-over-fiber focus on generation and fiber distribution of ultrabroadband impulses [77, 85, 86], but do not consider multipath distortion which is a dominating effect in most real environments.

In this chapter, we show that photonics can go beyond waveform distribution to provide also precompensation of important distortions in the wireless channels. To the best of our knowledge, this is the first experimental report that explores an RF-photonic transmitter both to characterize the multipath dispersions in real wireless channels and generate predistorted waveforms to achieve focusing through such environments. Although the conventional photonic AWG techniques have been used to partially compensate the frequency dependent delay of closely spaced directional antennas [40, 87], their time bandwidth product is insufficient for experiments involving multipath

channels where the received response is distorted orders of magnitude larger than the fundamental system time resolution. Here, we propose a new photonic AWG technique, Near-Field Frequency-to-Time Mapping (NF-FTM) [88], to circumvent the previous limitations and achieve high fidelity waveforms with radically increased time bandwidth product (TBWP). The large bandwidth available from our photonic waveform generator permits us to operate over the frequency range of 2-18 GHz, nearly an order of magnitude larger than the analogous experiments which relied on electronic waveform generators [67, 70, 89]. Our photonic AWG system supports remote applications with photonic drive signals generated remotely and delivered via fiber optics to a small optical-to-electronic conversion module (photodiode) at the required location, which is practically important to centralize the transmission equipment in a shared unit and reduce the complexity close to local users [77].

The remainder of this chapter is organized as follows. Section 6.2 mathematically describes the conventional frequency-to-time mapping approach which has enjoyed special attention in Radar and wireless communication applications. In section 6.3, we explain near-field frequency-to-time mapping and derive the achievable TBWP for this technique. Section 6.4 presents a numerical simulation to show unique advantages of the new proposed technique. Section 6.5 describes our experimental setup for the photonic AWG and provides an example in which we generate an ultrabroadband RF quadratic chirp signal over the frequency range of nearly baseband up to 41 GHz. This is more than a factor of two beyond the highest bandwidth available from commercial electronic arbitrary waveform generators. We show while this signal can be generated easily by the proposed NF-FTM technique with high fidelity, the conventional technique results in a very badly distorted signal. Section 6.6 compares the upper bound estimations of the RF bandwidth and time aperture achievable from NF-FTM and the conventional FTM techniques. Finally in section 6.7, we present the main implication of this chapter which is employing the introduced photonic AWG technique to suppress antenna distortion and multipath dispersion of ultrabroadband wireless systems with three octave bandwidth.
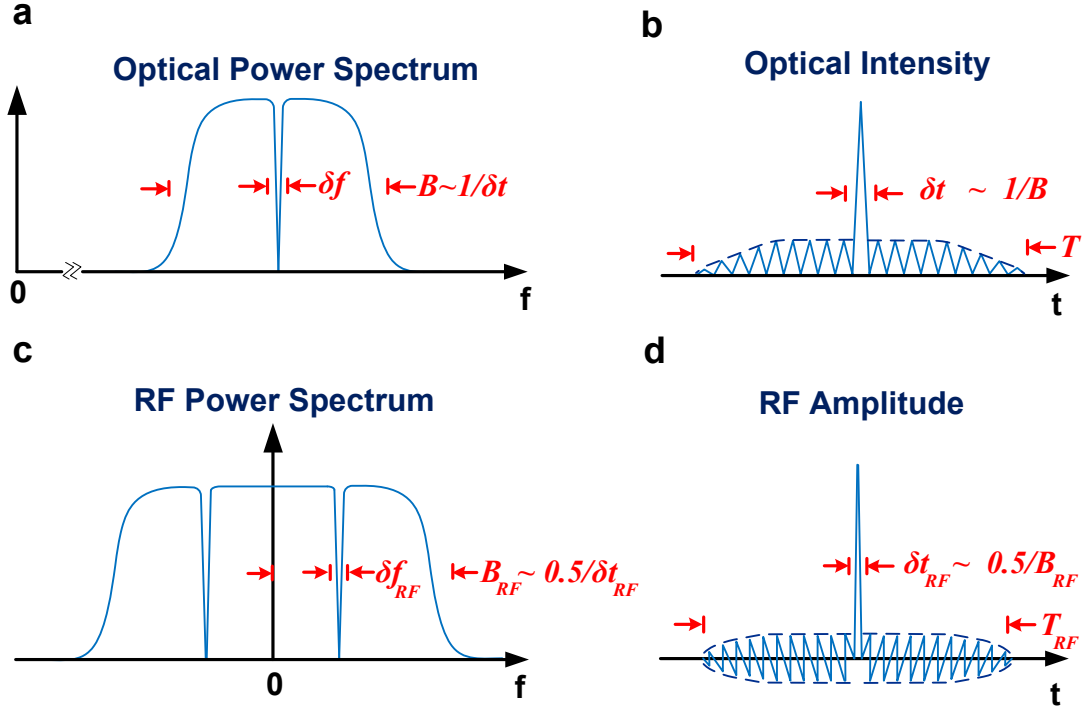
Fig 6.1 : (a-b) Frequency and time domain variables for optical waveforms. (c-d) Frequency and time domain variables for RF waveforms. We use subscript "RF" for all RF quantities.

## 6.2.  Frequency-to-Time Mapping for Microwave Photonics

Here we cover the basics of the conventional frequency-to-time mapping method and derive the relation between the maximum RF bandwidth and time aperture under the far-field condition. To facilitate discussion, we show frequency and time domain variables for optical and RF signals in Fig. 6.1. For optical waveforms, which are of a passband nature, the bandwidth $(B)$ is defined as the difference between the highest and lowest (nonzero) frequency components, Fig. 6.1(a). The shortest temporal feature, $\delta t$, is inversely related to the total bandwidth by $\delta t \sim 1/B$, and the maximum temporal window, $T$, is inversely related to the optical spectral resolution, $\delta f$, by $T \sim 1/\delta f$ . By contrast, for the baseband RF waveforms, the RF bandwidth, $B_{RF}$, is defined as the highest frequency component, as shown in Fig. 6.1(c). $B_{RF}$ is inversely related to twice the RF temporal

Table 6.1: Variables and their meaning. Optical variables refer to the shaped signal prior to dispersive propagation.

| Symbol | Meaning | Symbol | Meaning |
|--------|---------|--------|---------|
| $\delta t$ | Optical temporal resolution | $\delta t_{RF}$ | RF temporal resolution |
| $T$ | Optical time aperture | $T_{RF}$ | RF time aperture |
| $B$ | Optical bandwidth | $B_{RF}$ | RF bandwidth |
| $\delta f$ | Optical spectral resolution | $\Delta f_{inst}$ | Instantaneous freq. shift–optical |
| $\delta\phi$ | Phase change at a given time sample | $TBWP$ | Time bandwidth product |
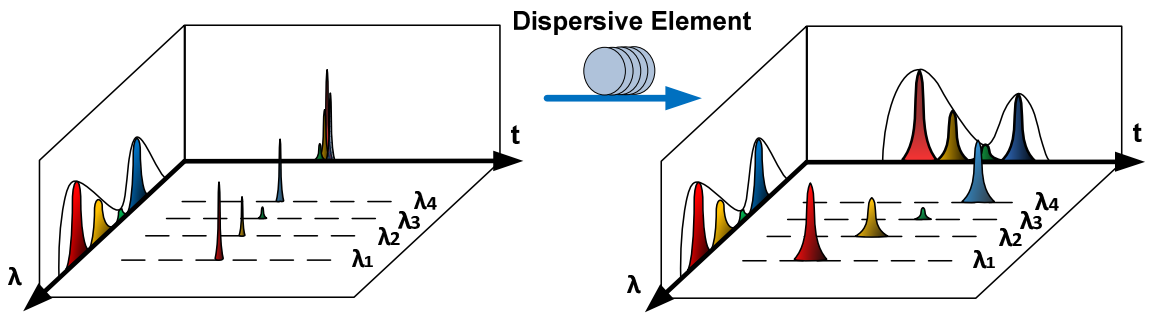


Fig 6.2: Frequency-to-time mapping phenomenon. When the shaped spectrum propagates through a dispersive element, different wavelengths travel at different speeds (only four wavelengths are shown for illustration). For sufficiently large chromatic dispersion, we get a linear frequency-dependent time delay which maps the power spectrum to the temporal intensity profile.

resolution, $\delta t_{RF}$, by $B_{RF} \sim 0.5/ \delta t_{RF}$ , consistent with the logic that two time samples are required to represent an RF cycle. These variables are all summarized in Table 6.1.

Fig. 6.2 shows the frequency-to-time mapping phenomenon. The desired waveform is programmed onto the optical power spectrum using a pulse shaping element (e.g. Fourier transform pulse shaper [90]). When the shaped spectrum propagates through a dispersive element with group delay dispersion (the frequency dependence of the group velocity), different wavelengths travel at different speeds. For large enough dispersion, we get a linear frequency-dependent time delay which maps the power spectrum to the temporal intensity profile.

Mathematically, the transformation of a pulse propagating in a medium with group delay dispersion ($\psi_2$) can be expressed by the Fresnel integral [61]:

$$a_{out}(t) \propto \exp\left(-j\frac{t^2}{2\psi_2}\right)\int_{-\infty}^{+\infty} a_{in}(t')\exp\left(-j\frac{t'^2}{2\psi_2}\right)\exp\left(j\frac{t\,t'}{\psi_2}\right)dt' \qquad (6.1)$$

where $a_{in}(t)$ and $a_{out}(t)$ are respectively the complex envelopes of the signals before and after the dispersive medium. Here $\psi_2$ is the group delay dispersion which is defined as $\psi_2 = -\partial^2\beta(\omega)/\partial\omega^2.L$ where $\beta(\omega)$ is the propagation constant of the medium with length $L$. In some applications, notably fiber optics the fiber dispersion is usually described in terms of a dispersion parameter $D$ with units $ps\ nm^{-1}\ km^{-1}$, related to the group delay dispersion as $\psi_2 = (\lambda^2 D)/(2\pi c).L$ where $\lambda$ is the wavelength and $c$ is the speed of light.

To facilitate our later discussion, we introduce the notation $a_{FTM}(t)$ to denote the shaped input field $a_{in}(t)$ associated with the frequency-to-time mapping. When the so called *far-field* limit is satisfied, the temporal phase variation associated with the $exp(-jt^2/2\psi_2)$ factor within the integral is negligible [61, 91, 92]. To be definite, in the analysis that follows we require that the phase variation within a time duration equal to the inverse of the finest spectral feature placed onto the input spectrum should be $< \pi/8$ [92] [1]. Under these conditions the output intensity profile is simply a scaled replica of the optical power spectrum, i.e.,

$$\left|a_{out}(t)\right|^2 \overset{\substack{Far\ Field \\ \propto \\ Limit}}{} \left|\exp\left(-j\frac{t^2}{2\psi_2}\right)\int_{-\infty}^{+\infty} a_{FTM}(t')\exp\left(j\frac{t\,t'}{\psi_2}\right)dt'\right|^2 = \left|A_{FTM}\left(\omega = -t/\psi_2\right)\right|^2 \quad (6.2)$$

where $A_{FTM}(\omega)$ is the Fourier transform of $a_{FTM}(t)$. Here, we take the definition of the Fourier transform of a function $f(t)$ as $F(\omega) = \int f(t')\exp(-j\omega t')\,dt'$. Equation (6.2) shows that the detected intensity profile after frequency-to-time mapping is proportional to the Fourier transform of the input signal at the angular frequency $\omega = -t/\psi_2$. For RF-

---

[1] Although closely related to the far-field condition, the requirement of quadratic phase $< \pi/8$ is more accurately termed the "antenna designer's formula." To keep the language simple, in this chapter we will refer simply to the "far-field condition".

AWG, the input power spectrum is shaped as $|A_{FTM}(\omega=-t/\psi_2)|^2$, which is taken to be equal to the desired RF waveform $|a_{out}(t)|^2$, appropriately scaled. Although equation (6.2) indicates that when FTM applies, the spectral phase of $A_{FTM}(\omega=-t/\psi_2)$ can be arbitrary chosen, we use a flat spectral phase for experiments and simulations in this chapter.

A critical bottleneck in this method, however, is the minimum required dispersion ($\psi_{2-min}$) to meet the far-field criterion. As explained above, this condition corresponds to tolerating phase errors up to $\pi/8$ within the quadratic factor $exp(-jt^2/2\psi_2)$ of the Fresnel integral [91, 92]:

$$\left| \frac{(T/2)^2}{2\,\psi_2} \right| < \frac{\pi}{8} \quad \Rightarrow \quad \frac{T^2}{\pi} < \left| \psi_2 \right| \quad \Rightarrow \quad \left| \psi_{2-min} \right| = \frac{T^2}{\pi} \approx \frac{1}{\pi\,\delta f^2} \tag{6.3}$$

This requirement directly imposes strict limits on the complexity and bandwidth of the achievable RF waveforms if arbitrary electrical waveforms are to be generated with high fidelity (low distortion):

$$B_{RF} \approx \frac{0.5}{\delta t_{RF}} \stackrel{2\pi\,\delta f=\delta t_{RF}/|\psi_2|}{=} \frac{0.5}{2\pi\,\delta f\,|\psi_2|} < \frac{0.5}{2\pi\,\delta f\,|\psi_{2-min}|} \stackrel{(6.3)}{\approx} 0.25\times\delta f \tag{6.4}$$

Here we have assumed that the minimum duration RF features ($\delta t_{RF}$) are determined by frequency-to-time mapping of the finest optical spectral features ($\delta f$). Equation (6.4) shows that the maximum achievable RF bandwidth of the conventional FTM method is proportional to the optical spectral resolution. To synthesize an undistorted RF waveform with larger frequency content, a coarser spectral resolution is required which limits one from exploiting the full TBWP of modern pulse shapers.

Working at the maximum RF bandwidth permitted under equation (6.4), the RF time aperture ($T_{RF}$) can be expressed as:

$$T_{RF} \approx N\delta t_{RF} = \frac{B}{\delta f}\delta t_{RF} \approx B\frac{1}{\delta f}\frac{0.5}{B_{RF}} \stackrel{(6.4)}{\approx} B\frac{0.25}{B_{RF}}\frac{0.5}{B_{RF}} \approx \frac{0.125\,B}{(B_{RF})^2} \tag{6.5}$$

where $N = T/\delta t = B/\delta f$ is the ratio of the time aperture and temporal resolution of the shaped optical signal prior to dispersive propagation, or equivalently the ratio of the optical bandwidth and finest spectral feature. In this regime, the TBWP is:

$$TBWP_{FTM} \overset{(6.5)}{\approx} \frac{0.125B}{B_{RF}} \tag{6.6}$$

Equation (6.6) shows the $TBWP_{FTM}$ is inversely proportional to the required RF bandwidth and becomes disappointingly small for RF bandwidth beyond those already available with electronic arbitrary waveform generators. Although experiments reaching bandwidths beyond the limit presented in equation (6.6) have been reported [93], the failure of these experiments to satisfy the far-field condition and the consequent significant loss of fidelity to generate arbitrary RF waveforms have apparently gone unnoticed.

## 6.3. Near-Field Frequency-to-Time Mapping

Here, we introduce a new technique which uses the amplitude and phase programmability of the shaper to overcome limitations imposed by the far-field requirement and achieve arbitrary nondistorted waveforms with the maximum available TBWP. In this approach, which we call Near-Field Frequency-to-Time Mapping (NF-FTM), the pulse shaper is programmed to yield a complex envelope $a_{NF\text{-}FTM}(t)$ represented by:

$$a_{NF-FTM}(t) = a_{FTM}(t)\exp\left(j\frac{t^2}{2\psi_2}\right) \tag{6.7}$$

where as mentioned above, $a_{FTM}(t)$ is defined in terms of the target RF waveform assuming frequency-to-time mapping strictly applies. Here $a_{FTM}(t)$ is multiplied by a new quadratic phase term that cancels out the phase factor $exp(-jt^2/2\psi_2)$ in equation (6.1). As a result the target waveform $|a_{out}(t)|^2$ that appears in the frequency-to-time mapping expression, equation (6.2), is obtained exactly independent of the far-field condition. Experimentally we realize this condition simply by reprogramming the pulse shaper according to the Fourier transform of equation (6.7); no new physical device is needed.

From another viewpoint, equation (6.7) is reminiscent of time lens [94, 95] studies in which physical elements such as electro-optic phase modulators or nonlinear wave mixing generate quadratic temporal phase. However, in our scheme we compute the effect of the quadratic temporal phase to arrive at a complex optical spectrum, which we then program in the optical frequency domain. Since there is no physical element providing direct time domain phase, we can consider our new approach as assisted by a virtual-time-lens. The waveform predistortion prescribed under this method advances the location at which the Fourier transform relation of equation (6.2) applies from the far-field into the near-field region, enabling generation of waveforms not accessible under the far-field condition.

### 6.3.1.   Theory of Near-field Frequency-to-Time Mapping

As mentioned for the FTM technique, a phase error of $\pi/8$ is tolerable in the Fresnel integral. Hence, the quadratic phase introduced in equation (6.7) does not necessarily need to exactly cancel out the phase factor $exp(-jt^2/2\psi_2)$ in equation (6.1) to produce the desired RF waveforms. This makes our new NF-FTM method tolerant of small phase errors that may arise in experimental systems.

#### 6.3.1.1. Maximum RF Bandwidth Limit

Here, we analyze the ability to realize the operation specified by equation (6.7) using a Fourier transform pulse shaper. The assumed temporal quadratic phase implies time-varying frequency shifts away from the initial frequency content. Since shaping occurs in the spectral domain which does not increase optical bandwidth, a main requirement for physical realizability is that the spectral broadening that would accompany the quadratic temporal phase remains small compared to the optical bandwidth. Here, we follow this logic to establish a limit on the maximum temporal quadratic phase that may be introduced.

The phase shift of the *nth* temporal feature ($\phi_n$) of the quadratic factor applied in equation (6.7) can be written as:

$$\phi_n = \frac{\delta t^2 (n - N/2)^2}{2\psi_2}, \qquad 1 \le n \le N \qquad (6.8)$$

Where $N$, as defined above, is the total number of resolvable features of the pulse shaper. The maximum phase change from one temporal feature to the next ($\delta\phi_{max}$) which occurs at the edges of the quadratic phase is:

$$\delta\phi_{max} = |\phi_N - \phi_{N-1}| \overset{(6.8)}{=} \frac{\delta t^2}{2|\psi_2|}(N-1) \approx \frac{\delta t^2}{2|\psi_2|} N = \frac{\delta t^2}{2|\psi_2|} \frac{B}{\delta f} \overset{\delta t \sim 1/B}{\approx} \frac{1}{B} \frac{1}{2|\psi_2|} \frac{1}{\delta f} \quad (6.9)$$

Using the fact that the detected intensity profile is proportional to the Fourier transform of the input signal at the angular frequency $\omega = -t/\psi_2$, we have:

$$\delta\phi_{max} \overset{(6.9)}{\approx} \frac{1}{B} \frac{1}{2|\psi_2|} \frac{1}{\delta f} \overset{2\pi \, \delta f = \delta t_{RF}/|\psi_2|}{=} \frac{\pi}{B} \frac{1}{\delta t_{RF}} \overset{\delta t_{RF} \sim 0.5/B_{RF}}{\approx} \frac{2\pi}{B} B_{RF} \qquad (6.10)$$

Equation (6.10) shows the maximum applied temporal phase shift ($\delta\phi_{max}$) is proportional to the ratio of the generated RF bandwidth ($B_{RF}$) to the optical bandwidth. Although the applied temporal quadratic phase shift is essential to get a faithful frequency to time mapping in the near field region, it remains small except at very high RF bandwidth such that $B_{RF}$ approaches the optical bandwidth. For example for ultrabroadband waveforms with bandwidth in the range of ~10 to ~100 GHz, the $B_{RF}$ is orders of magnitude smaller than the optical bandwidth (optical bandwidth of 5THz is assumed), and the corresponding $\delta\phi_{max}$ is limited to the range of only ~$0.004\pi$ to ~$0.04\pi$.

To estimate the maximum spectral broadening that would be introduced by a true quadratic temporal phase factor, we use the principle of the instantaneous frequency shift ($\Delta f_{inst}$) [61]. This parameter is defined in terms of the time derivative of the applied temporal phase ($\delta\phi$) as:

$$\Delta f_{inst} = \frac{1}{2\pi} \frac{\delta\phi}{\delta t} \le \frac{1}{2\pi} \frac{\delta\phi_{max}}{\delta t} \overset{\delta t \sim 1/B}{\approx} \frac{\delta\phi_{max}}{2\pi} B \overset{(6.10)}{\approx} B_{RF} \qquad (6.11)$$

Equation (6.11) shows the instantaneous frequency shift that would accompany a true quadratic temporal phase is proportional to the target RF bandwidth. This equation

reconfirms our conclusion derived based on equation (6.10) from another viewpoint. The spectral broadening that would accompany the quadratic phase factor remains considerably small unless the RF bandwidth approaches the optical bandwidth. For example, when we seek to generate an RF signal with maximum bandwidth in the range of 10 to 100 GHz, the corresponding spectral broadening implied by the quadratic phase factor is limited to the range of only 0.2% to 2% of the initial optical spectrum bandwidth (optical bandwidth of 5 THz is assumed).

The $\Delta f_{inst}$ calculated in equation (6.11) is the shift we would get if we multiplied by a real quadratic phase. Since we cannot increase the optical bandwidth in our method (since we employ spectral shaping, which implements a virtual not a real time lens), we require the implied instantaneous frequency shift (or equivalently the RF bandwidth) to be much smaller than optical spectrum bandwidth. Otherwise the near-field frequency-to-time mapping process will be disturbed.

$$\Delta f_{inst} \overset{(6.11)}{\approx} B_{RF} \ll B \qquad \overset{(6.10)}{\Leftrightarrow} \qquad \delta\phi_{max} \ll 2\pi \qquad (6.12)$$

As a conservative bound, we limit the instantaneous frequency shift (or equivalently the RF bandwidth) to be smaller than one-eighth of the optical bandwidth *(B)* (e.g., for a pulse shaper with 5 THz spectral bandwidth, this number is roughly 625 GHz). This means that NF-FTM can be applied over a very wide microwave frequency range while maintaining waveform fidelity, which is quite distinct from conventional FTM. From another viewpoint, this condition is equivalent to limiting the maximum temporal phase change from one feature to the next to be smaller than π/4:

$$\delta\phi_{max} \overset{(6.10)}{\approx} \frac{2\pi}{B} B_{RF} \qquad \xrightarrow{\quad B_{RF} < 0.125 \times B \quad} \qquad \delta\phi_{max} < \frac{\pi}{4} \qquad (6.13)$$

This condition is in close agreement with the results of a series of numerical simulations we have performed considering bandwidth, pixelation and resolution limitations of the pulse shapers. Some simulation examples are provided in section 6.4 and 6.5.3.

### 6.3.1.2. Time Aperture versus RF Bandwidth

For the generated microwave waveforms within the limit of equation (6.12), the time aperture and the maximum RF bandwidth are related as:

$$T_{RF} = N\delta t_{RF} = \frac{B}{\delta f}\delta t_{RF} \overset{\delta t_{RF} \sim 0.5/B_{RF}}{\approx} \frac{B}{\delta f}\frac{0.5}{B_{RF}} \tag{6.14}$$

In this regime, the achievable time bandwidth product (TBWP) can be estimated by:

$$TBWP_{NF-FTM} \approx 0.5\frac{B}{\delta f} \tag{6.15}$$

As we see from equation (6.15), the $TBWP_{NF\text{-}FTM}$ in near-field frequency-to-time mapping is only a function of pulse shaper's characteristics. In particular, the available TBWP is equal to one half the number of spectrally resolved control elements within the optical bandwidth. As long as equation (6.12) is satisfied, $TBWP_{NF\text{-}FTM}$ is directly proportional to the optical bandwidth and is independent of the targeted RF bandwidth. This is in contrast to equation (6.6), for which the $TBWP_{FTM}$ in conventional frequency-to-time mapping was inversely proportional to the required RF bandwidth.

### 6.4. Simulation Results

Here we simulate generation of a linear down-chirp signal (instantaneous frequency changes linearly with time) with time aperture of ~125 ns and RF bandwidth of ~20 GHz, corresponding to a TBWP of 2500. The pulse shaper is simulated based on the model presented in [61, 96] which includes the finite bandwidth of the input field, the finite spectral resolution of the pulse shaper associated with the finite spot size of any single frequency component at the Fourier plane, and the pixellated nature of the spatial light modulator employed in the pulse shaper. In this simulation, a pulse shaper with 25125 pixels, optical spectral resolution of 1 GHz, and total optical bandwidth of 5.025 THz (corresponds to the lightwave C band) is used. Although such a pulse shaping experiment is beyond any reported yet, pulse shapers with resolution well below 1 GHz have already

been demonstrated [97, 98], as have programmable shapers with thousands of individually controllable elements at a few GHz spectral resolution configured in a novel two-dimensional spectral dispersion geometry [99]. Thus, this example is chosen to motivate the potential to generate high fidelity RF arbitrary waveforms through NF-FTM even for pulse shapers that challenge the state-of-the-art.

The output of the pulse shaper is stretched through a dispersive medium with total dispersion of 3.125 ns/nm to yield a time aperture of 125 ns. Figure 6.3(a) shows the target waveform programmed onto the power spectrum, assuming frequency-to-time mapping applies. The roll-off (loss of modulation contrast) for the short wavelength portion of Fig. 6.3(a) arises because the rapidity of spectral modulation is approaching the pulse shaper spectral resolution. As explained in [61, 96], the effect of pulse shaper resolution can be modeled by convolving with a Gaussian signal in the frequency domain, which introduces attenuation for spectral modulation that is too rapid.

In this example in which we use a total dispersion of 3.125 ns/nm, the far-field limit is strongly violated. Equation (6.3) shows for pulse shaping with a finest spectral feature of 1 GHz, the far-field limit is satisfied only for dispersions larger than ~250 ns/nm. Here, the maximum temporal phase variation (in the quadratic phase term inside the integral of equation (6.1)) is ~$10\pi$ within a time duration equal to the inverse of finest spectral feature placed onto the spectrum by the pulse shaper. This is much larger than the maximum allowed value ($\pi/8$) in the far-field criterion. As a result the generated RF waveform, Fig. 6.3(b), is badly distorted, and certain groups of frequencies are strongly attenuated, Fig. 6.3(c).

Now, we use near-field frequency-to-time mapping to circumvent the far-field condition. To avoid any possible confusion, we would like to emphasize that the required temporal quadratic phase required to advance the Fourier plane into the near-field region is several orders of magnitude smaller than the spectral phase induced by the dispersive medium (e.g. optical fibers). For instance in this example, the total unwrapped spectral phase arising due to passage through the dispersive medium is ~$1.6 \times 10^5 \pi$, while the maximum temporal phase required to implement the virtual time lens is only ~$10\pi$.
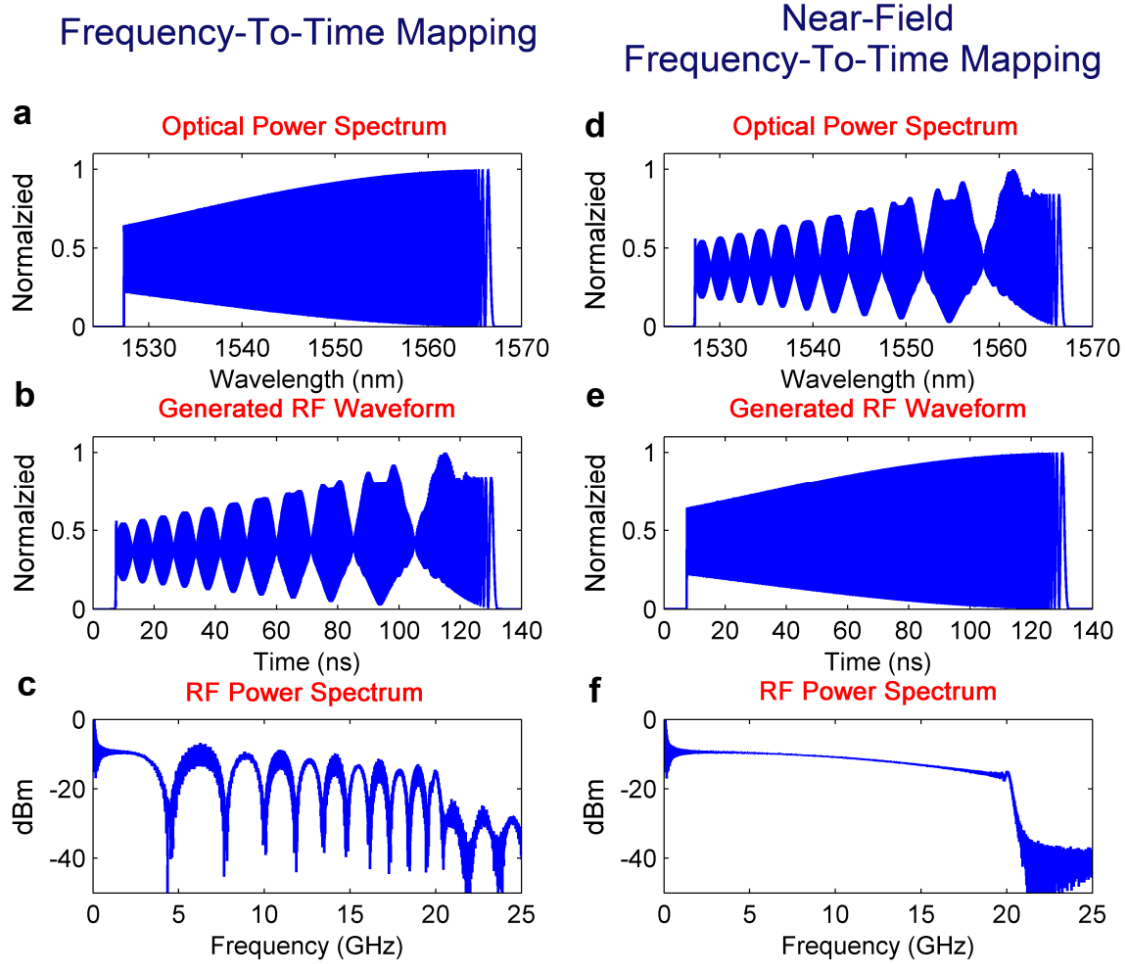
Fig 6.3: Simulating the generation of a linear down-chirp RF waveform over frequencies from baseband to ~20 GHz with time aperture of ~125 ns, corresponding to a TBWP of ~2500. (a-c) Waveforms from conventional frequency-to-time mapping. The generated RF waveform is badly distorted, and certain frequencies are strongly attenuated. (d-f) Waveforms from near-field frequency-to-time mapping. A beautiful chirp is obtained, and the RF spectrum extends smoothly out to ~20 GHz.

Fig. 6.3(d) shows the optical power spectrum shaped according to equation (6.7) based on NF-FTM. In this example in which a flat spectral phase is assumed for $a_{FTM}(t)$, the optical power spectrum for NF-FTM, Fig. 6.3(d), is a scaled replica of the temporal distortion of Fig. 6.3(b). A simple derivation explaining this scaling relationship is presented in the Appendix (B). Although Fig. 6.3(d) shows only the power spectrum, the corresponding field must have the spectral phase function as prescribed by NF-FTM. This is unlike FTM, where input spectral phase does not affect output power spectrum.

When this pre-distorted signal propagates through the dispersive medium, a time domain RF waveform with beautiful chirp is obtained, Fig. 6.3(e), in excellent agreement with the target waveform–refer to Fig. 6.3(a), appropriately scaled. The RF spectrum of this signal, Fig. 6.3(f), extends smoothly out to ~20 GHz with less than 6.5 dB roll-off in respect to the 1 GHz frequency component.

## 6.5.  Experimental Implementation of NF-FTM

### 6.5.1.  Experimental Setup

The experimental setup is shown in Fig. 6.4. An erbium-doped fiber ring mode-locked laser with repetition rate of ~50 MHz and wavelength range of ~1520 nm-1610 nm is used as the input source. The laser pulses are shaped with a commercial pulse shaper (FINISAR 1000s) with spectral resolution of ~10 GHz and operating wavelength range of 1527.4 nm-1567.4 nm. The output pulses are stretched in ~10.3 km of single mode fiber (total dispersion of ~170 ps/nm and dispersion slope of ~0.57 ps/nm$^2$). The RF signal is detected by a high-speed photodetector with bandwidth of ~50 GHz. A digital sampling oscilloscope and an RF spectrum analyzer with respective bandwidths of
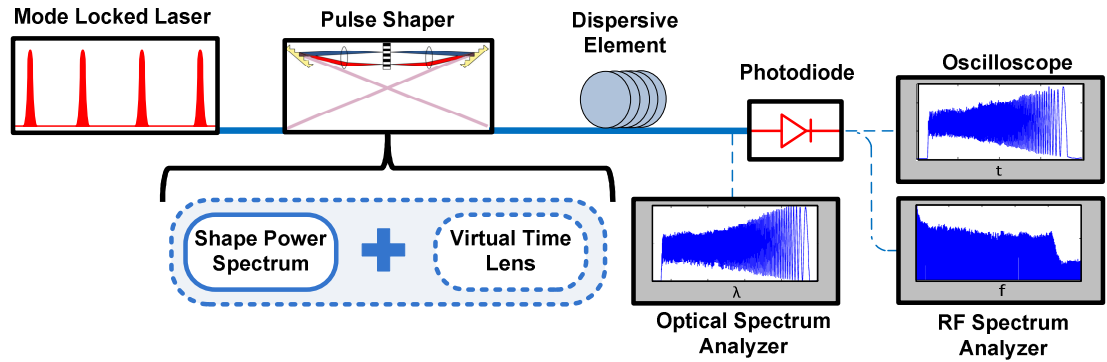


Fig 6.4: Experimental setup (only main components are shown). Output pulses of a mode-locked laser are sent through a pulse shaper with spectral resolution of ~10 GHz. The pulse shaper can be programmed either according to the conventional FTM method in which the desired waveform is sculpted onto the optical power spectrum or according to the Near-Field Frequency-to-Time mapping (NF-FTM) algorithm. In NF-FTM the spectral shaping of FTM is modulated as prescribed by an assumed quadratic temporal phase factor (virtual time lens) resulting in both amplitude and phase spectral shaping. In either case, the generated signals are stretched in a dispersive element, and then the RF signals are detected by a high-speed photodiode (PD).

60 GHz and 50 GHz are used to characterize the generated RF waveforms in time and frequency. The optical spectrum is also measured with an optical spectrum analyzer with spectral resolution of 0.01 nm.

### 6.5.2. Experimental Result

We illustrate the limits of conventional FTM with an experiment in which we seek to generate a quadratic down-chirp waveform with ~41 GHz bandwidth and ~6.8 ns time aperture. The instantaneous frequency is designed to decrease monotonically from 41 GHz down to baseband according to a concave-down quadratic function of time.

Assuming frequency-to-time mapping applies, the target waveform is written onto the power spectrum, Fig. 6.5(a). However, for this example, for which the variation of the temporal quadratic phase term within the integral of equation (6.1) reaches ~$1.84\pi$, the far-field criterion is strongly violated. As a result the generated RF waveform, Fig. 6.5(b), is badly distorted, and certain groups of frequencies are strongly attenuated, Fig. 6.5(c). To comply with the far-field condition, equation (6.4) dictates that in order to synthesize an RF waveform with spectrum up to 41 GHz, the pulse shaper should be programmed with super-pixels with minimum resolution of ~164 GHz (equation (6.4)), much coarser than the ~10 GHz spectral resolution capability of the pulse shaper. This would reduce the maximum possible TBWP of the synthesized waveform to <17 (equation (6.6)) for frequency-to-time mapping free of significant distortion.

To overcome the limitations of the far-field condition, we use the proposed NF-FTM. Fig. 6.5(d) shows the new optical power spectrum which now shows strong predistortions that closely resemble the temporal distortions of Fig. 6.5(b). Unlike previously, the shaped field is necessarily programmed with spectral phase variation as well; however, this is not visible in a plot of the power spectrum. After dispersive propagation a time domain RF waveform with beautiful chirp is obtained, Fig. 6.5(e), in close agreement with the target waveform – refer to Fig. 6.5(a), appropriately scaled. Here due to the pulse shaper spectral resolution, the high frequency modulations of the chirp signal shows an amplitude roll-off compared to later, low frequency components.
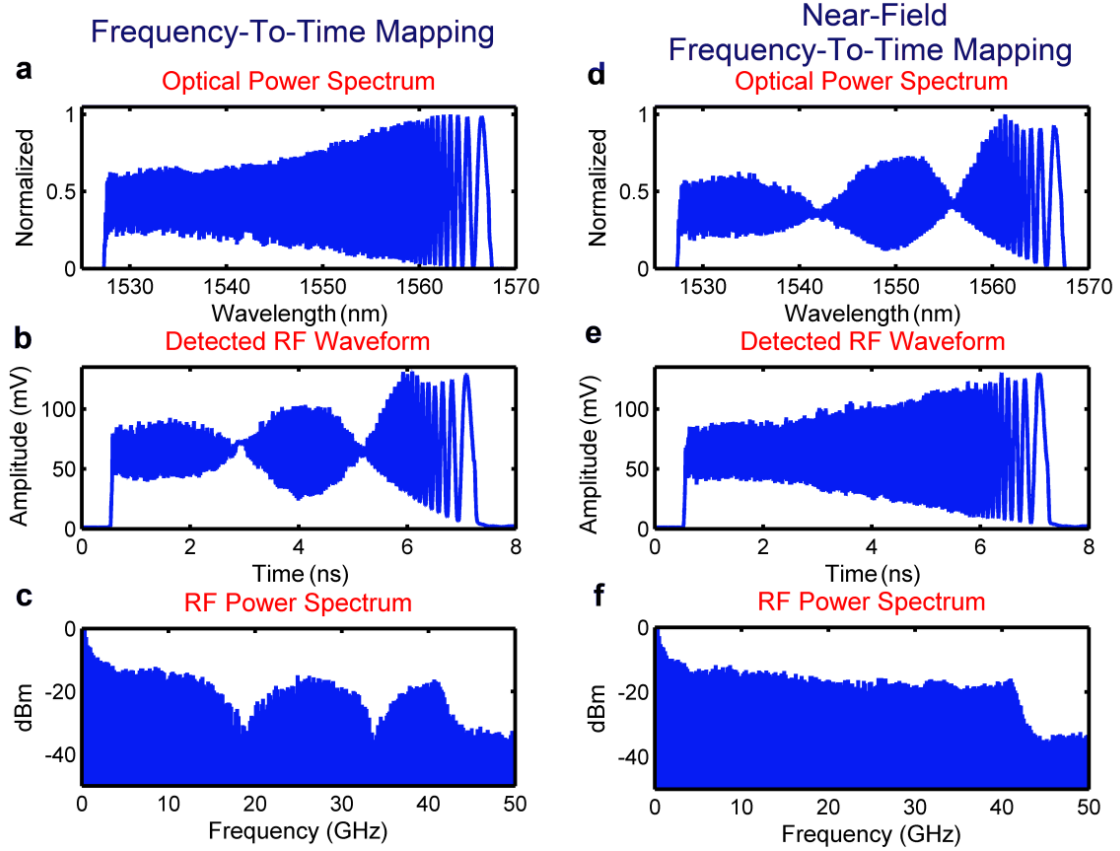
Fig 6.5: Generating down-chirp RF waveform over frequencies from baseband to ~41 GHz with time aperture of ~6.8 ns, corresponding to a TBWP of ~280. (a-c) Waveforms from conventional frequency-to-time mapping. Generated RF waveform is badly distorted and certain frequencies are strongly attenuated. (d-f) Waveforms from near-field frequency-to-time mapping. A beautiful chirp is obtained and the RF spectrum extends smoothly out to ~41 GHz with less than 5 dB roll-off in respect to the 4 GHz frequency components.

Removing constraints imposed by the far-field criterion, a TBWP of ~280, near the maximum possible using this pulse shaper, is now achieved. The RF spectrum, Fig. 6.5(f), extends smoothly out to ~41 GHz with less than 5 dB roll-off with respect to the 4 GHz frequency components. This is more than a factor of two beyond the highest bandwidth available from commercial electronic arbitrary waveform generators. This combination of high RF bandwidth and large TBWP, while maintaining excellent waveform fidelity, is unprecedented in photonic RF-AWG.

### 6.5.3. Verification of the Experiment

To evaluate the experimental accuracy of the synthesized waveforms via our proposed NF-FTM method, we compare the generated chirp waveform shown in Fig. 6.5(e) with a numerical simulation result. For the simulations in this section, a pulse shaper with 5025 pixels, optical spectral resolution of 10 GHz, and total optical bandwidth of 5.025 THz (corresponds to the lightwave C band) is modeled, which is the same as the parameters of the commercial pulse shaper (Finisar WaveShaper 1000s) used in our experiments. The output waveform from the pulse shaper is stretched through a dispersive medium with total group delay dispersion of ~170 ps/nm and dispersion slope of ~0.57 ps/nm$^2$ to yield a time aperture of ~6.8 ns. Although the group delay dispersion contribution is dominant, the third order dispersion shifts the frequency components slightly compared to the ideal mapping, and should be included in the simulation to most closely model the experiment.
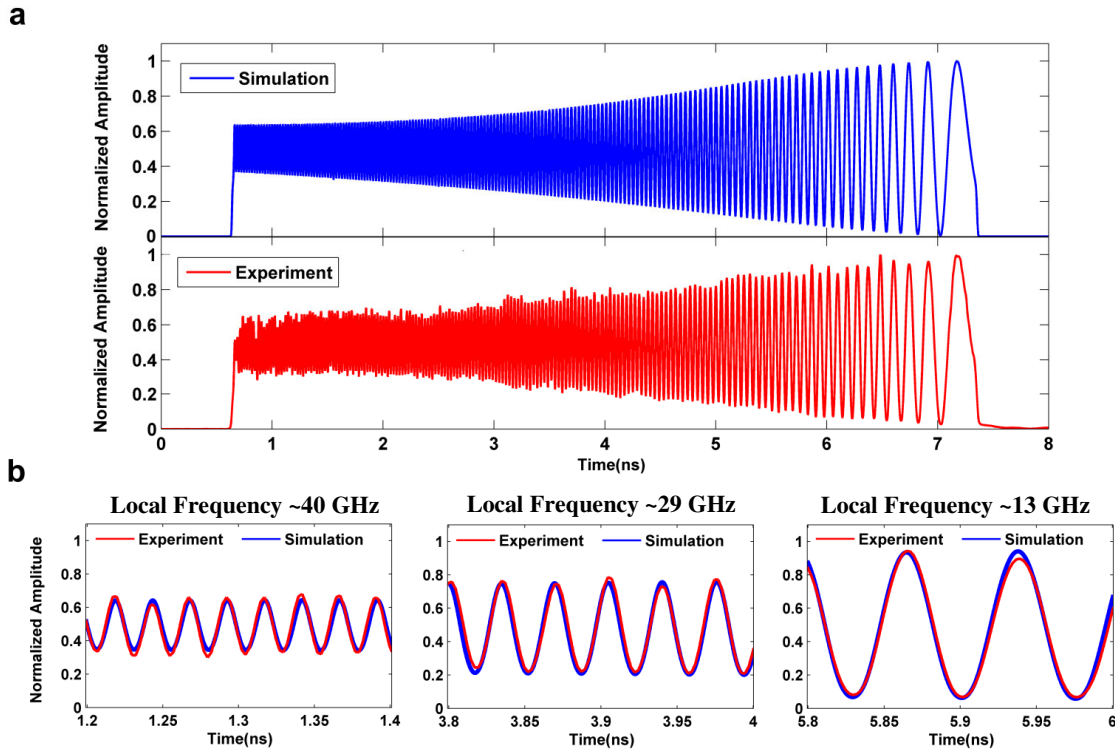


Fig 6.6: (a) Experimental result versus simulation for the generated chirp waveform with time aperture of ~6.8 ns and bandwidth of ~41 GHz. (b) we overlay these curves on top of each other and zoom in on different parts of the waveform to show details. The agreement between the simulation and experimental results is excellent.

Figure 6.6 compares the experimental result with simulation. The agreement between the two curves is excellent. In Fig. 6.6(b), we overlay these curves on top of each other and zoom in on different parts of the waveform to show details. We can see the simulation and the experiment match peak for peak and there are at most a few percent differences between them. The correlation coefficient between these two curves is on the order of 99.2%, which shows an extremely good match between simulation and experimental results.

## 6.6. Near-Field versus Conventional Frequency-to-Time Mapping

In Fig. 6.7, we show upper bound estimations of the RF bandwidth and time aperture achievable from the conventional FTM and NF-FTM techniques for two shapers with assumed spectral resolutions of 1 GHz and 10 GHz. In both cases we have assumed 5 THz optical bandwidth, corresponding to the lightwave C band. Conventional FTM is restricted to the space below the far-field limit (equation (6.5)) for which good waveform fidelity is maintained, whereas NF-FTM is bounded only by the optical bandwidth (equation (6.12) and (6.13)) and pulse shaper resolution (equation (6.14)) limits. In NF-FTM the maximum achievable TBWP, which is directly proportional to the number of pulse shaping pixels resolved within the optical bandwidth, can be maintained over a wide RF bandwidth range. However, in conventional FTM a coarser spectral resolution is required for higher RF bandwidths, which reduces the maximum possible TBWP. The impact of our approach is especially clear for shapers operating at high spectral resolutions. For example, for a shaper with assumed 1GHz resolution, a time aperture of 125 ns should be possible for frequencies up to 20 GHz (TBWP of ~2,500), while the time aperture would be limited to 1.56 ns (TBWP < 31) for the conventional technique (see section 6.4). The gray shaded rectangle shows the region of interest for compensation of multipath dispersion in ultrabroadband wireless communications. While NF-FTM can generate appropriate waveforms for this application, the conventional FTM technique is far away from this region.
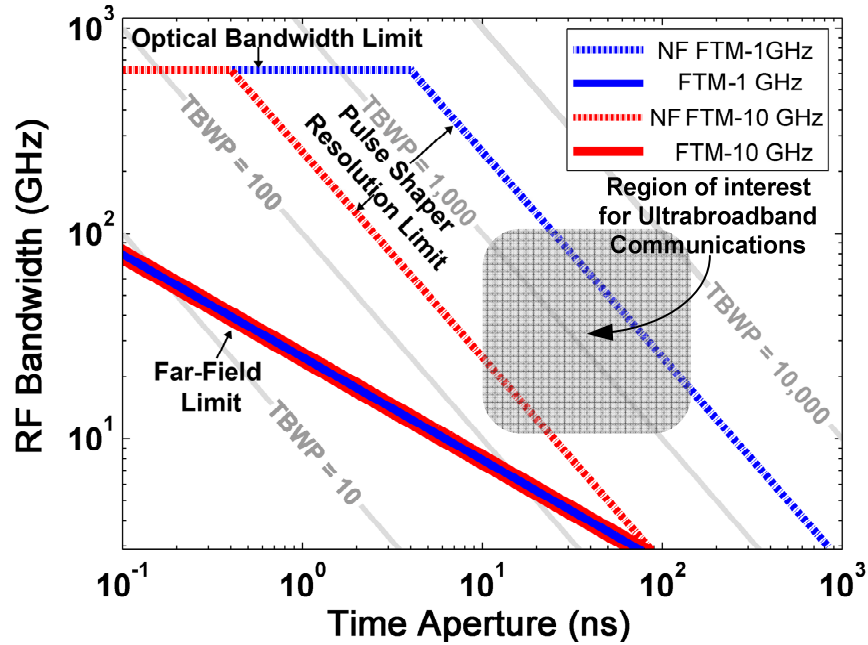
Fig 6.7: Upper bounds of the achievable waveforms based on conventional FTM and NF-FTM for two shapers with assumed spectral resolutions of 1 GHz and 10 GHz and optical bandwidth of 5THz. Conventional FTM is restricted to the space below the "far-field limit" for which good waveform fidelity is maintained, whereas NF-FTM is bounded only by the "optical bandwidth" and "pulse shaper resolution" limits. The gray shaded rectangle shows the region of interest for compensation of multipath dispersion in ultrabroadband wireless communications. While NF-FTM can generate appropriate waveforms for this application, the conventional FTM technique is far away from this region.

## 6.7. Near-Field Frequency-to-Time Mapping for Suppression of Antenna Distortion and Multipath Dispersion

The unprecedented instantaneous RF bandwidth available from NF-FTM offers potentials for new horizons in areas such as chirped radar, high-speed covert wireless, and RF sensing. Here we employ this method to generate precompensated waveforms that self-compress through the ultrabroadband channels. We use the same microwave photonic AWG setup introduced in Fig. 6.4 with ~3.37 km of dispersion compensating fiber (total dispersion of ~-404 ps/nm) to stretch the shaped pulses from the pulse shaper over the time aperture of ~16.2 ns. The detected RF signals by a ~50 GHz photodetctor propagate through the wireless channel by a transmit antenna (Tx).

Experiments were carried out to compensate the frequency-dependent delay characteristic of two directional spiral antennas which are placed in a LOS environment. In a different scenario, we use microwave photonics to demonstrate spatio-temporal focusing of ultrabroadband signals through the multipath channels. We use a pair of horn antennas (Rx1-Rx2) to receive transmitted signals from a biconical antenna in a non-line-of-sight environment. In both cases, we use *spread spectrum channel sounding* with deconvolution as described in chapter 2 to measure impulse response of the wireless channels. Here, we program our photonic AWG based on the near-field frequency-to-time mapping method [88] to synthesis a quadratic up-chirp signal with time aperture of ~16.2 ns and frequency range of ~DC-18 GHz. The instantaneous frequency is designed to increase monotonically from DC to ~18 GHz according to a concave-down quadratic function of time.

First, we perform a calibration measurement, in which the sounding chirp waveform is recorded without wireless transmission ($x_{Trans}(t)$) (the photodiode output is directly connected to the oscilloscope), Fig. 6.8(a). The amplitude roll-off (loss of contrast) at the high frequency modulations of the generated chirp signal compared to the low frequency components arises because the rapidity of spectral modulation in NF-FTM technique is approaching the pulse shaper spectral resolution [88].

The RF spectrum of this waveform extends smoothly out to ~18 GHz with less than 7 dB roll-off with respect to the 2 GHz frequency components, Fig. 6.8(b). Here, the dramatically increased time aperture available through NF-FTM by circumventing the far-field condition is necessary to provide an increased transmit energy without sacrificing bandwidth. If one uses the conventional frequency-to-time mapping technique, as a result of violating the far-field condition, the generated waveform is badly distorted (Fig. 6.8(c)), and certain groups of frequencies are strongly attenuated (Fig. 6.8 (d)) [88].

After the calibration measurement, this waveform propagates through the wireless channel, and the received response is recorded on the receiver side. To extract impulse responses accounting for the effects of both the antennas and the propagation channel

**Near Field
Frequency to Time Mapping**

**a**  Generated RF Waveform

**b**  Power Spectrum

**Conventional
Frequency to Time Mapping**

**c**  Generated RF Waveform

**d**  Power Spectrum
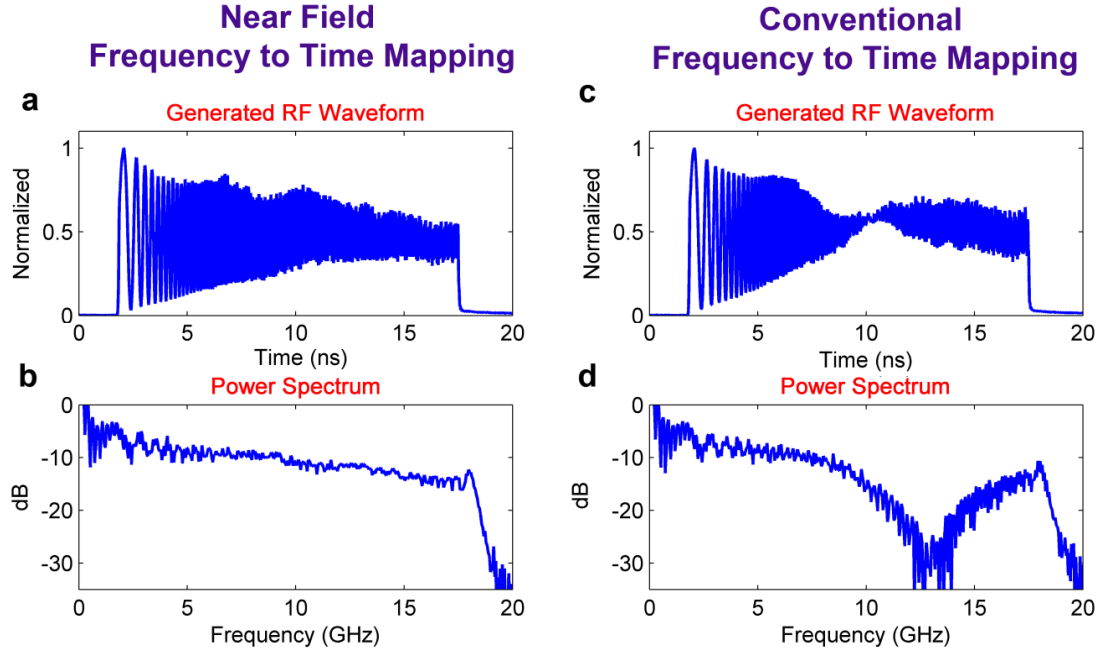
Fig 6.8: Photonically generated RF waveform over frequencies from baseband to ~18 GHz with time aperture of ~16.2 ns. (a-b) The sounding waveform generated via NF-FTM technique. A beautiful chirp is obtained and the RF spectrum extends smoothly out to ~18 GHz. (c-d) When the conventional FTM technique is employed the synthesized waveform is badly distorted and certain frequencies are strongly attenuated.

($h_{Sys}(t)$), deconvolution is applied between the transmitted and received waveforms in the frequency domain. By implementing deconvolution, modulations of the transmitted power spectrum due to system imperfections (e.g. the roll-off at high frequency components) are taken out which ideally results in a perfect estimation of the system impulse response.

### 6.7.1. Microwave Photonics for Antenna Distortion Compensation

We employ the spread spectrum channel sounding to measure impulse response of the spiral antennas in a LOS environment with propagation distance of ~3m. As explained in chapters 2 and 3, spiral antennas are highly directional and their channel responses are dominated by the antennas' dispersion (frequency dependent delay). Figure 6.9 shows the impulse response and the power spectrum over a three octave frequency

range of 2 to 18 GHz. Our measured impulse response extends mainly over ~10 ns and shows a down-chirp characteristic.

The conventional FTM technique has been employed in [40] to partially compensate dispersion of spiral antennas. Due to their limited TBWP of ~25, they have generated the pre-compensation waveforms with bandwidths less than 10 GHz over ~2.5 ns time apertures. Here we program our photonic AWG based on NF-FTM to generate the time reversal signals with ~16.2 ns time aperture, well beyond the maximum delay dispersion
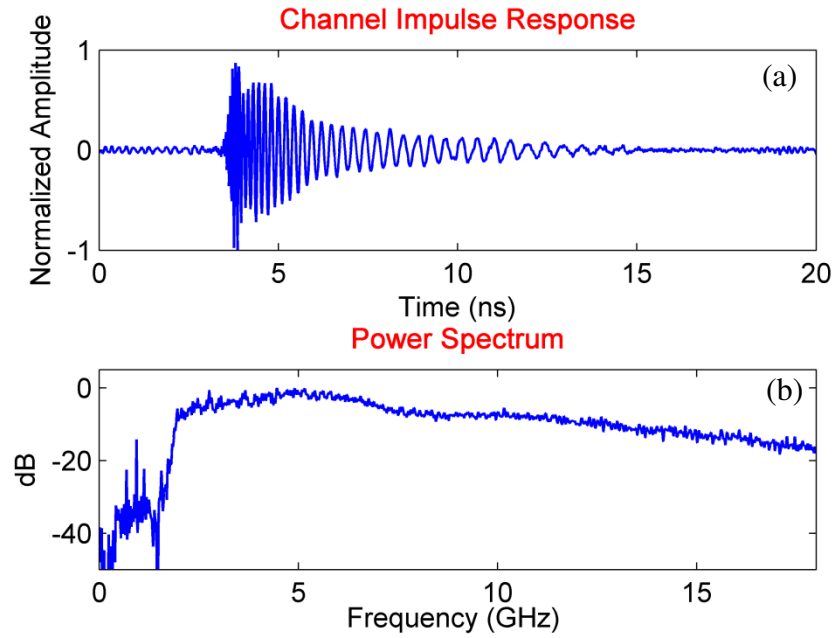


Fig. 6.9: (a) Impulse response of LOS spiral antennas with propagation distance of ~3m. (b) Power spectrum of the measured impulse response.
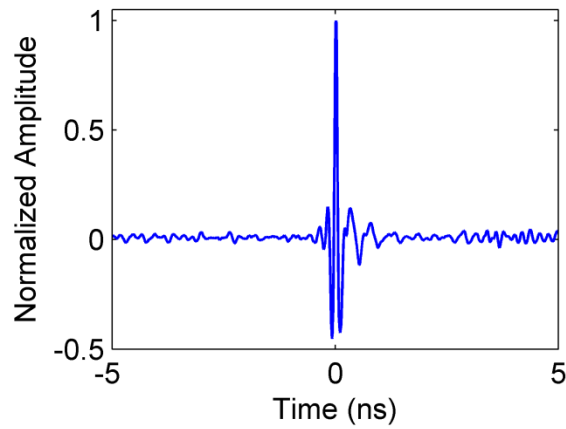


Fig. 6.10: Received response from time reversal excitation with FWHM of ~50 ps.

of spiral antennas, over the frequency bandwidth of ~18 GHz. In our experiments, the maximum frequency range is limited by the spiral antenna's bandwidth rather than by the photonic AWG technique. Fig 6.10 shows the received response from time reversal excitation. The full width half maximum of the received response is ~50 ps which shows the considerable temporal focusing achieved via TR compared to the original channel impulse response, Fig. 6.9(a).

### 6.7.2. Microwave Photonics for Spatio-Temporal Compression through Multipath Environments

To demonstrate spatio-temporal compression through multipath environments, we use a pair of horn antennas (Rx1-Rx2) to receive transmitted signals from a biconical antenna in a NLOS environment with ~10m propagation distance. Receive antennas are separated from each other by 50 cm. Figures 6.11 (a,b) show the measured impulse responses. In the small subfigures, we zoom in on the dashed rectangles to better show
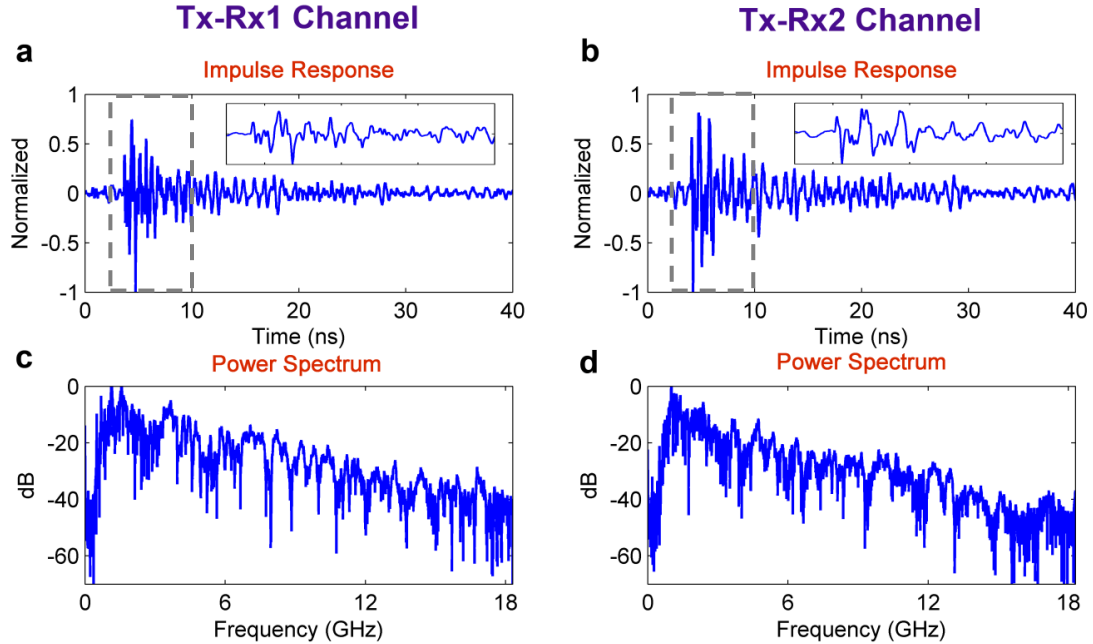


Fig. 6.11: (a-b) Impulse responses of Tx-Rx1 and Tx-Rx2 channels. In the small subfigures, we zoom in on the dotted rectangles to better show details. (c-d) Corresponding power spectra of the Tx-Rx1 and Tx-Rx2 links.

details. Both responses exhibit strong multipath dispersion up to ~30 ns, more than 1000 times larger than the ~20 ps fundamental time resolution corresponding to the 2-18 GHz frequency range. Due to the strong multipath scattering, the impulse responses are nearly uncorrelated although the delay spreads are similar. The power spectra of these responses are shown in Fig. 6.11 (c,d). Both spectra are significantly frequency selective, which is the direct consequence of the channel multipath effects.

With knowledge of the channel responses, we can compress the received RF response in time and space via phase (pre)compensation (PC) of the transmit waveforms [59]. We synthesize the PC waveform over an ~16.2 ns time aperture (which covers the major components of the multipath delay spread) for channel excitation using the near-field frequency-to-time mapping method. Here photonic RF-AWG and NF-FTM are crucial to realize precompensation waveforms with the desired bandwidth and time aperture. When the waveform is precompensated for Tx-Rx1, a clear peaking results at
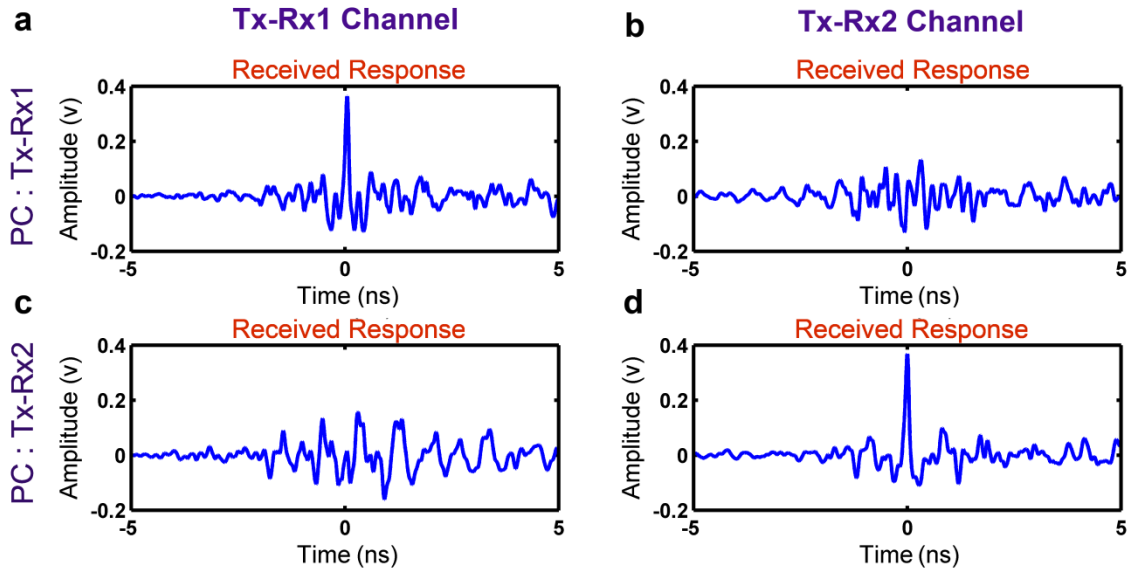


Fig 6.12: (a-b) When the phase compensated (PC) transmit waveform is designed based on the Tx-Rx1 response, a significant peaking results at the target receiver. Receiver Rx2 located just a couple of wavelength away from the target receiver gets only a noise like interference. (c-d) When the Tx transmits a waveform designed to achieve peaking at Rx2, the received signal by Rx1 now remains noise-like.

the target receiver (temporal focusing), Fig. 6.12(a). The full width half maximum (FWHM) of the received signal is less than 70 ps  which shows the considerable achieved temporal focusing via PC compared to the original channel impulse response, Fig. 6.11(a). The interesting point is that although the precompensated waveform is transmitted omni-directionally, Rx2 which is located a few wavelengths away from the intended receiver (Rx1) gets a noise-like waveform, Fig. 6.12(b) (spatial focusing). In a similar way, when the Tx is driven with a waveform selected to achieve peaking at Rx2 (Fig. 6.12(d)), the signal received by Rx1 remains noise-like (Fig. 6.12(c)).

In summary, we have introduced a new RF photonic AWG method which removes restrictions imposed by the far-field criterion and achieves high fidelity waveforms with radically increased TBWP. The unique generated waveforms with unprecedented instantaneous RF bandwidth offer potential for new horizons in areas such as chirped radar, high-speed covert wireless, and RF sensing. As two intriguing examples of how our technique impacts new applications, we have demonstrated compensation of the frequency-dependent delay characteristic of directional spiral antennas and spatio-temporal compression of RF signals with three octave bandwidth in strong multipath channels.

# 7.  SUMMARY AND FUTURE RESEARCH DIRECTIONS

## 7.1.  Summary

In this work, we experimentally investigated three main aspects of UWB systems including waveform generation, propagation estimation, and distortion compensation. In chapter 1, we summarized unique advantages of UWB technology and pointed out some of the current practical challenges. In chapter 2, we investigated accuracy of spread spectrum channel sounding based on deconvolution in typical LOS and NLOS indoor environments, in the later case up to 15 m propagation distance. Wideband probing waveforms provide higher levels of total transmitted power compared to ultrashort pulses, which results in a higher dynamic range. We studied the accuracy of calculated impulse responses by comparing channel measurements obtained for PN sequence and chirp waveform excitation. Different experiments including LOS spiral and NLOS omni-directional antennas show more than 99 percent agreement between the chirp and PN excitation results. In another route to test the accuracy, time reversal has been carried out experimentally. Correlation coefficients between experimental and theoretical time reversal traces are on the order of 0.98. Our experiments clearly show that spread spectrum channel sounding can provide high accuracy measurements of the channel impulse response over the full UWB band.

In chapter 3, we used the spread spectrum sounding technique to investigate impulse response and time reversal characteristics of omni-directional and spiral antennas in LOS and NLOS environments, over the frequency range up to 12 GHz. As we expected, impulse responses of NLOS environments exhibit greater multipath effects, hence more time dispersion, compared to the corresponding LOS experiments. These channel dispersions are particularly significant in omni-directional antennas which transmit and receive signals in all directions. Time Reversal technique was applied to all channels measured, and excellent accuracy of our experiments is proved by comparing the results

with TR simulations. "RMS delay spread" and "peak-to-average power ratio" are calculated as two basic parameters for impulse response and TR performance evaluations. In our experiments time reversal shows most impressive compression results, as characterized through reduced RMS delay spread and increased peak-to-average power ratio, for spiral antennas in a LOS configuration, for which effects associated with spectral phase variation dominate. Compression is negligible for omni-directional antennas in a LOS configuration, for which interference structure in the power spectrum dominates. The compression performance of time reversal is modest for the NLOS configuration studied and is similar for both antenna types; in these cases both spectral phase variations and variations in the power spectra are important. Thus, the effectiveness of time reversal in SISO experiments is subject to a trade-off between competing effects – namely, compensation of spectral phase variation (which leads to compression) and aggravation of spectral amplitude structure (which opposes compression).

Chapter 4 introduced the phase compensation (PC) prefilter as a solution to suppress intersymbol interference in UWB systems. We investigated its performance in LOS and NLOS environments over the frequency range up to 12 GHz via experiments and simulations. We compared the effectiveness of PC versus TR in terms of multipath suppression, sensitivity to the noisy estimated responses, channel hardening, and data transmission over communication channels. We compare the "temporal compression" and "PAPR" gains of these prefilters both based on experimentally measured responses over actual indoor channels as well as simulated channels using IEEE 802.15.4(a). Our study suggested that PC has superior performance in compressing UWB multipath dispersions, a point which is proved theoretically in terms of the PAPR in the Appendix (A). The BERs of the measured channels are presented for different data rates (125 Mbps - 4Gbps) as a function of the received SNR. Our results show PC prefiltering considerably outperforms TR in mitigating ISI due to UWB channel dispersion. We investigated the spatial focusing performance of PC versus TR. Such spatial focusing is critically important for covert communications and multiuser systems. All in all, our results suggest that the PC prefilter has the potential to be used in high-speed covert

UWB communication channels as an effective way to combat channel multipath dispersions, provide channel hardening and spatio-temporal focusing.

In chapter 5, we extended our work to multiple antenna systems and introduced an experimental setup to study transmit beamforming over MISO-UWB configurations. Due to the practical difficulties of providing direct electrical delays, our implementation was based on photonics by taking advantage of low loss optical fibers to apply different appropriate time shifts to the output of an electrical AWG. Time-domain spread spectrum channel sounding (which has short acquisition time and high dynamic range) was used to simultaneously characterize system impulse responses. By exploiting the high quality impulse response data, we applied MISO-TR beamforming and proved our capability to carry out high accuracy measurements (correlation coefficients on the order of 98%). To the best of our knowledge, this was the first experimental report of multi-antenna beamforming over the full UWB band.

In chapter 6, in contrast to the previous chapters in which electronic devices were used to synthesize arbitrary RF waveforms, here we generate the required UWB signals using photonic approaches. Photonic AWG provides several unique opportunities such as ultra-broad bandwidth and cost-efficiency compared to the electronic devices. We introduced a new RF photonic AWG method which removes previous restrictions and achieves high fidelity waveforms with radically increased TBWP. The unprecedented instantaneous RF bandwidth available from our technique offers potentials for new horizons in areas such as chirped radar, high-speed covert wireless, and RF sensing. We employed our photonically generated RF waveforms to investigate space-time focusing of wireless pulses that encounter strong scattering and distortion during indoor, through-wall propagation. The large bandwidth available from our photonic waveform generator permits us to operate over a bandwidth nearly an order of magnitude larger bandwidth (leading to potentially much higher data rates) than what has been reported in previous experiments on space-time focusing of wireless signals which relied on electronic waveform generators. Furthermore, the TBWP needed to achieve the space-time focusing is far beyond the limits of conventional FTM explained above, but is now enabled for the first time via our NF-FTM method. Our work for the first time showed that photonics can go beyond RF distribution to provide also precompensation of important distortions in the wireless channels. Most

previous works on this subject focus on generation and fiber distribution of ultrabroadband impulses, but do not consider multipath distortion which is a dominating effect in most real wireless channels.

## 7.2. Future Research Directions

To perform, all the transmit beamforming techniques require the channel state information (CSI) on the transmitter side. Typically, the CSI is estimated on the receiver by exciting the channel with a training signal. The obtained information is then fedback to the transmitter through a reverse link as overhead. In UWB channels with a large number of resolvable components, this implies a large amount of feedback load which can become a practical hurdle in time varying environments in which the CSI should be updated at a rate much faster than the channel coherence time. To leverage this problem, one scheme is to quantize the CSI so that a smaller number of bits to be fedback to the transmitter side.

One interesting research direction is to assess the performance of PC compared to TR under the limited rate feedback in real wireless channels. Although the effect of quantization error on the UWB transmit beamforming has been investigated by several authors for UWB channels, but they particularly study time reversal performance when only the temporal phase information of the channel impulse response is provided on the transmitter side, a technique known as one-bit time reversal (OBTR) [50, 57, 100-102]. The majority of these works are theoretical studies based on the simplified models which do not take into account important propagation effects of real wireless environments like distance dependence, random variation of the path loss exponent, and frequency dependence of the path gain [50, 102-104]. A few who have studied the OBTR beamforming based on the measured channel responses either cover a small portion of the UWB or are completely out of the 3.1-10.6 GHz band [57, 105]. We believe studying the transmit beamforming performance under the limited rate feedback channels based on the measured impulse responses over the full UWB band would be an important contribution compared to the previous published works on this topic.

Another interesting research direction would be employing the introduced experimental test-bed in chapter 5 to investigate the effects of practical challenges like imperfect channel estimation, coherency between the multiple transmitters, or unwanted antenna couplings on the spatio-temporal focusing of UWB multiple antennas. As we explained, much of the previous research in multiple antenna systems for UWB is theoretical and based on simplified models which do not address experimental challenges such as imperfect channel estimation or transmitter synchronization. One important contribution would be employing polarization multiplexing [106] (antennas with difference polarizations) in addition to the spatial multiplexing to have approximately uncorrelated channels which is necessary in a multiple antenna system to get spatio-temporal focusing gains together with the power gain. As we showed spatially separated antennas have uncorrelated impulse responses in multipath channels. Polarization diversity can be employed to provide uncorrelated impulse responses without the strict antenna spacing requirements.

Finally, another interesting enhancement to our current work would be employing the introduced photonic RF arbitrary waveform generator to transmit actual data information through strongly multipath channels. As discussed, photonic AWG provides several advantages such as ultra-broad bandwidth, cost-efficiency and immunity to electromagnetic interference compared to the electronic devices. In this way, the radio-over-fiber technology also provides the opportunity to centralize the transmission equipment in a shared unit which is important in a practical system.

REFERENCES

LIST OF REFERENCES

[1]     M.-G. Benedetto, T. Kaiser, A. F. Molisch, I. Oppermann, C. Politano, and D. Porcino, "UWB communication systems A comprehensive overview," *Hindawi Publishing Corporation*, 2006.

[2]     Federal Communications Commission (FCC), "First report and order in the matter of revision of part 15 of the commission's rule regarding ultrawideband transmission systems," FCC 02-48, 2002.

[3]     A. Goldsmith, "Wireless Communications," Cambridge Univ. Press, 2005.

[4]     A. F. Molisch, J. R. Foerster, and M. Pendergrass, "Channel models for ultrawideband personal area networks," *IEEE Wireless Communications,* vol. 10, pp. 14-21, 2003.

[5]     D. Jourdan, D. Dardari, and M. Z. Win, "Position error bound for UWB localization in dense cluttered environments," *IEEE Transactions on Aerospace and Electronic Systems,* vol. 44, pp. 613-628, 2008.

[6]     N. Guo, B. M. Sadler, and R. C. Qiu, "Reduced-complexity UWB time-reversal techniques and experimental results," *IEEE Transactions on Wireless Communications,* vol. 6, pp. 4221-4226, 2007.

[7]     N. Guo, J. Q. Zhang, Z. Peng, H. Zhen, S. Yu, and R. C. Qiu, "UWB real-time testbed with waveform-based precoding," in *IEEE Military Communications Conference, MILCOM* pp. 1-7, 2008.

[8]     A. Khaleghi, G. E. Zein, and I. H. Naqvi, "Demonstration of Time-Reversal in indoor Ultra-Wideband communication: time domain measurement," in *4th International Symposium on Wireless Communication Systems ISWCS*, pp. 465-468, 2007.

[9]     I. H. Naqvi, G. E. Zein, G. Lerosey, J. d. Rosny, P. Besnier, A. Tourin*, et al.*, "Experimental validation of time reversal ultra wide-band communication system for high data rates," *IET Microwaves, Antennas & Propagation,* vol. 4, pp. 643-650, 2010.

[10]    A. F. Molisch, "Ultra-Wide-Band Propagation Channels," *Proceedings of the IEEE,* vol. 97, pp. 353-371, Feb 2009.

[11]    J. Romme, and B. Kull, "On the relation between bandwidth and robustness of indoor UWB communication," *IEEE Conference on Ultra Wideband Systems and Technologies,* pp. 255-259, 2003.

[12]    I. I. Immoreev and P. G. S. D. V. Fedotov, "Ultra wideband radar systems: advantages and disadvantages," in *IEEE Conference on Ultra Wideband Systems and Technologies*, pp. 201-205, 2002.

[13] J. Karedal, S. Wyne, P. Almers, F. Tufvesson, and A. F. Molisch, "A measurement-based statistical model for industrial ultra-wideband channels," *IEEE Transactions on Wireless Communications,* vol. 6, pp. 3028-3037, 2007.

[14] D. Cassioli, A. Durantini, W. Ciccognani, "The role of path loss on the selection of the operating bands of UWB systems," *IEEE 15th International Symposium on Personal, Indoor and Mobile Radio Communications,* vols 1-4, pp. 2787-2791, 2004.

[15] P. Pagani and P. Pajusco, "Experimental analysis of the Ultra Wideband propagation channel over the 3.1 GHz - 10.6 GHz frequency band," in *IEEE 17th International Symposium on Personal, Indoor and Mobile Radio Communications*, pp. 1-5, 2006.

[16] J. Keignart and N. Daniele, "Subnanosecond UWB channel sounding in frequency and temporal domain," in *IEEE Conference on Ultra Wideband Systems and Technologies*, pp. 25-30, 2002.

[17] W. Q. Malik, "Spatial correlation in ultrawideband channels," *IEEE Transactions on Wireless Communications,* vol. 7, pp. 604-610, 2008.

[18] R. J. M. Cramer, R. A. Scholtz, and M. Z. Win, "Evaluation of an ultra-wide-band propagation channel," *IEEE Transactions on Antennas and Propagation ,* vol. 50, pp. 561-570, 2002.

[19] T. C. K. Liu, D. I. Kim, and R. G. Vaughan, "A high-resolution, multi-template deconvolution algorithm for time-domain UWB channel characterization," *Canadian Journal of Electrical and Computer Engineering,* vol. 32, pp. 207-213, 2007.

[20] N. A. Alsindi, D. Birru, and W. Dong, "Ultra-Wideband Channel Measurement Characterization for Wireless Magnetic Resonance Imaging Applications," in *41st Annual Conference on Information Sciences and Systems CISS '07 ,* pp. 135-140, 2007.

[21] Z. Irahhauten, J. Dacuna, G. J. M. Janssen, and H. Nikookar, "UWB channel measurements and results for wireless personal area networks applications," in *The European Conference on Wireless Technology*, pp. 189-192, 2005.

[22] A. Muqaibel, A. Safaai-Jazi, A. Attiya, B. Woerner, and S. Riad, "Path-loss and time dispersion parameters for indoor UWB propagation," *IEEE Transactions on Wireless Communications,* vol. 5, pp. 550-559, 2006.

[23] J. R. Klauder, A. C. Price, S. Darlington, and W. J. Albersheim, " The theory and design of chirp radars," *Bell System Technical Journal,* vol. 39, pp. 745-808, 1960.

[24] R. Zetik, J. Sachs, and R. S. Thoma, "UWB short-range radar sensing - The architecture of a baseband, pseudo-noise UWB radar sensor," *IEEE Instrumentation & Measurement Magazine,* vol. 10, pp. 39-45, 2007.

[25] S. L. Zhou, G. B. Giannakis, and A. Swami, "Digital multi-carrier spread spectrum versus direct sequence spread spectrum for resistance to jamming and multipath," *IEEE Transactions on Communications,* vol. 50, pp. 643-655, 2002.

[26] J. Schoukens and R. Pintelon, "Identification of linear systems - A practical guideline to accurate modeling" *Pergamon Press*, 1991.

[27]    A. Richter, "Estimation of radio channel parameters: models and algorithms," ed. Technical University Ilmenau, Germany: Ph. D. dissertation, 2005.

[28]    D. V. Sarwate and M. B. Pursley, "Crosscorrelation properties of pseudorandom and related sequences," *Proceedings of the IEEE,* vol. 68, pp. 593-619, 1980.

[29]    A. Hein, "Processing of SAR data: fundamentals, signal processing, interferometry," Berlin: Springer, 2004.

[30]    G. J. M. Janssen and J. A. M. Vriens, "High resolution coherent radio channel measurements using direct sequence spread spectrum modulation," in *6th Mediterranean Electrotechnical Conference*, vol.1, pp. 720-727, 1991.

[31]    D. Cassioli and A. Durantini, "Measurements, modeling and simulations of the UWB propagation channel based on direct-sequence channel sounding," *Wireless Communications & Mobile Computing,* vol. 5, pp. 513-523, 2005.

[32]    A. Durantini, W. Ciccognani, and D. Cassioli, "UWB propagation measurements by PN-sequence channel sounding," in *IEEE International Conference on Communications*, vol.6, pp. 3414-3418, 2004.

[33]    R. Zetik, and R. Thoma, "Ultra-wideband real-time channel sounder - design, construction and selected applications," in 20th Telecommunications Forum (TELFOR), pp. 975-978, 2012.

[34]    Available: http://www.channelsounder.de

[35]    M. Kowatsch and J. Lafferl, "A spread-spectrum concept combining chirp modulation and pseudonoise coding," *IEEE Transactions on Communications,* vol. 31, pp. 1133-1142, 1983.

[36]    M. Fink, "Time reversal of ultrasonic fields. I. Basic principles," *IEEE Transactions on Ultrasonics, Ferroelectrics and Frequency Control,* vol. 39, pp. 555-566, 1992.

[37]    G. Tesserault, N. Malhouroux, and P. Pajusco, "Determination of material characteristics for optimizing WLAN radio," in *European Conference on Wireless Technologies*, pp. 225-228, *2007.*

[38]    G. L. Li and P. K. L. Yu, "Optical intensity modulators for digital and analog applications," *Journal of Lightwave Technology,* vol. 21, pp. 2010-2030, 2003.

[39]    M. K. Tsatsanis and G. B. Giannakis, "Blind estimation of direct sequence spread spectrum signals in multipath," *IEEE Transactions on Signal Processing ,* vol. 45, pp. 1241-1252, 1997.

[40]    J. D. McKinney, D. Peroulis, and A. M. Weiner, "Dispersion limitations of Ultra-Wideband wireless links and their compensation via photonically enabled arbitrary waveform generation," *IEEE Transactions on Microwave Theory and Techniques ,* vol. 56, pp. 710-719, 2008.

[41]    J. D. McKinney, D. Peroulis, and A. M. Weiner, "Time-domain measurement of the frequency-dependent delay of broadband antennas," *IEEE Transactions on Antennas and Propagation,* vol. 56, pp. 39-47, 2008.

[42]    Y. Ishiyama and T. Ohtsuki, "Performance comparison of UWB-IR using RAKE receivers in UWB channel models," in *International Workshop on Ultra Wideband Systems Joint with Conference on Ultrawideband Systems and Technologies (UWBST & IWUWBS),* pp. 226-230, 2004.

[43]    M. Fink, C. Prada, F. Wu, and D. Cassereau, "Self focusing in inhomogeneous media with time reversal acoustic mirrors," in *IEEE Ultrasonics Symposium*, pp. 681-686 vol.2, 1989.

[44]    K. Popovski, B. J. Wysocki, and T. A. Wysocki, "Modelling and comparative performance analysis of a time-reversed UWB system," *EURASIP Journal on Wireless Communications and Networking,* 2007.

[45]    K. Witrisal and M. Pausini, "Statistical Analysis of UWB Channel Correlation Functions," *IEEE Transactions on Vehicular Technology ,* vol. 57, pp. 1359-1373, 2008.

[46]    C. Oestges, J. Hansen, S. Emami, A. Kim, G. Papanicolaou, and A. Paulraj, "Time reversal technique for broadband wireless communication systems," *In the European Microwave Conference*, 2004.

[47]    D. Abbasi-Moghadam and V. T. Vakili, "Characterization of indoor time reversal UWB communication systems: Spatial, temporal and frequency properties," *International Journal of Communication Systems,* vol. 24, pp. 277-294, 2011.

[48]    A. Dezfooliyan and A. M. Weiner, "Evaluation of time domain prorogation measurements of UWB systems using spread spectrum channel sounding," *IEEE Transcations on Anetnnas and Propagation*, Vol. 60, pp. 4855-4865, 2012.

[49]    A. Dezfooliyan and A. M. Weiner, "UWB propagation measurement using spread spectrum channel sounding," in *IEEE International Symposium on Antennas and Propagation (APSURSI),* pp. 2805-2808, 2011.

[50]    P. Kyritsi and G. Papanicolaou, "One-bit Time Reversal for WLAN applications," in *IEEE 16th International Symposium on Personal, Indoor and Mobile Radio Communications PIMRC*, pp. 532-536, 2005.

[51]    F. Monsef, A. Cozza, and L. Abboud, "Effectiveness of Time-Reversal technique for UWB wireless communications in standard indoor environments," in *Conference Proceedings ICECom*, pp. 1-4, 2010.

[52]    C. Zhou, N. Guo, and R. C. Qiu, "Experimental results on multiple-input single-output (MISO) time reversal for UWB systems in an office environment," in *IEEE Military Communications Conference*, pp. 1-6, 2006.

[53]    A. F. Molisch, D. Cassioli, C. Chia-Chin, S. Emami, A. Fort, B. Kannan*, et al.*, "A Comprehensive Standardized Model for Ultrawideband Propagation Channels," *IEEE Transactions on Antennas and Propagation,* vol. 54, pp. 3151-3166, 2006.

[54]    C. Oestges, A. D. Kim, G. Papanicolaou, and A. J. Paulraj, "Characterization of space-time focusing in time-reversed random fields," *IEEE Transactions on Antennas and Propagation,*  vol. 53, pp. 283-293, 2005.

[55]    T. Wang and T. Lv, "Canceling interferences for high data rate time reversal MIMO UWB system: a precoding approach," *EURASIP Journal on Wireless Communications and Networking,* vol. 2011, p. 959478, 2011.

[56]    H. Nguyen, Z. Zhao, F. Zheng, and T. Kaiser, "Preequalizer design for spatial multiplexing SIMO-UWB TR Systems," *IEEE Transactions on Vehicular Technology,* vol. 59, pp. 3798-3805, 2010.

[57]  H. T. Nguyen, "Optimal one bit time reversal for UWB impulse radio in multi-user wireless communications," *Proceedings of World Academy of Science: Engineering & Technology,* vol. 48, pp. 298, 2008.

[58]  A. Dezfooliyan and A. M. Weiner, "Experimental test-bed for studying multiple antenna beamforming over Ultrawideband channels up to 12 GHz," *IEEE Wireless Communications Letters,* vol. 1, pp. 520-523, 2012.

[59]  A. Dezfooliyan and A. M. Weiner, "Phase Compensation communication technique versus Time Reversal for Ultrawideband channels," *Accepted for publication in IET Communications,* 2013.

[60]  J. P. Heritage and A. M. Weiner, "Advances in spectral optical code-division multiple-access communications," *IEEE Journal of Selected Topics in Quantum Electronics,* vol. 13, pp. 1351-1369, 2007.

[61]  A. M. Weiner, "*Ultrafast Optics*," Wiley, 2009.

[62]  A. V. Oppenheim, R. W. Schafer, and J. R. Buck, "*Discrete-time signal processing*," Prentice-Hall, 1999.

[63]  D. J. Love and R. W. Heath, Jr., "Equal gain transmission in multiple-input multiple-output wireless systems," *IEEE Transactions on Communications,* vol. 51, pp. 1102-1110, 2003.

[64]  P. Kyritsi, P. Stoica, G. Papanicolaou, P. Eggers, and A. Oprea, "Time Reversal and Zero-Forcing equalization for fixed wireless access channels," in *the 39th Asilomar Conference on Signals, Systems and Computers*, pp. 1297-1301, 2005.

[65]  F. Adachi, H. Tomeba, and K. Takeda, "Introduction of frequency-domain signal processing to broadband single-carrier transmissions in a wireless channel," *IEICE Transactions on Communications,* vol. E92B, pp. 2789-2808, 2009.

[66]  R. K. Martin, K. Vanbleu, D. Ming, G. Ysebaert, M. Milosevic, B. L. Evans*, et al.*, "Implementation complexity and communication performance tradeoffs in discrete multitone modulation equalizers," *IEEE Transactions on Signal Processing ,* vol. 54, pp. 3216-3230, 2006.

[67]  P. Blomgren, P. Kyritsi, A. D. Kim, and G. Papanicolaou, "Spatial focusing and intersymbol interference in Multiple-Input Single-Output Time Reversal communication systems," *IEEE Journal of Oceanic Engineering,* vol. 33, pp. 341-355, 2008.

[68]  H. T. Nguyen, I. Z. Kovacs, and P. C. F. Eggers, "A Time Reversal transmission approach for multiuser UWB communications," *IEEE Transactions on Antennas and Propagation,* vol. 54, pp. 3216-3224, 2006.

[69]  Y. Jin, Y. Jiang, and J. M. F. Moura, "Multiple antenna Time Reversal transmission in Ultrawideband communications," in *IEEE Global Telecommunications Conference*, pp. 3029-3033, 2007.

[70]  C. Zhou, N. Guo, and R. C. Qiu, "Time-Reversed Ultra-wideband (UWB) Multiple Input Multiple Output (MIMO) Based on Measured Spatial Channels," *IEEE Transactions on Vehicular Technology ,* vol. 58, pp. 2884-2898, 2009.

[71]  Y. Song, Z. Hu, N. Guo, and R. C. Qiu, "Real-time MISO UWB radio testbed and waveform design," in *IEEE Proceedings of the SoutheastCon (SouutheastCon),* pp. 204-209, 2010.

[72]  Y. Song, N. Guo, Z. Hu, and R. C. Qiu, "FPGA based UWB MISO time-reversal system design and implementation," in *IEEE International Conference on Ultra-Wideband (ICUWB),* pp. 1-4, 2010.

[73]  I. H. Naqvi and G. E. Zein, "Time reversal technique for ultra wide-band and MIMO communication systems," Wireless Communication, INTECH publishers.

[74]  E. Udvary and T. Berceli, "Tunable optical delay line feed for phased array antennas," in *16th European Conference on Networks and Optical Communications (NOC)*, pp. 40-43, 2011.

[75]  A. Dezfooliyan and A. M. Weiner, "Experimental investigation of UWB impulse response and time reversal technique up to 12 GHz : omni-directional and directional antennas," *IEEE Transactions on Antennas & Propagagation,* vol 60, pp. 3407-3415,  2011.

[76]  A. Dezfooliyan and A. M. Weiner, "Experimental Study of UWB Impulse Response and Time Reversal Communication Technique up to 12 GHz," in *IEEE Vehicular Technology Conference (VTC Fall)*, pp. 1-5, 2011.

[77]  J. Yao "Photonics for ultrawideband communications," *IEEE Microwave Magazine,*  vol. 10, pp. 82-95, 2009.

[78]  J. D. McKinney, D. E. Leaird, and A. M. Weiner, "Millimeter-wave arbitrary waveform generation with a direct space-to-time pulse shaper," *Opt. Lett.,* vol. 27, pp. 1345-1347, 2002.

[79]  J. Chou, Y. Han, and B. Jalali, "Adaptive RF-photonic arbitrary waveform generator," *IEEE Photonics Technology Letters,* vol. 15, pp. 581-583, 2003.

[80]  I. S. Lin, J. D. McKinney, and A. M. Weiner, "Photonic synthesis of broadband microwave arbitrary waveforms applicable to ultra-wideband communication," *IEEE Microwave and Wireless Components Letters,* vol. 15, pp. 226-228, 2005.

[81]  V. Torres-Company, J. Lancis, and P. Andres, "Arbitrary waveform generator based on all-incoherent pulse shaping," *IEEE Photonics Technology Letters,* vol. 18, pp. 2626-2628, 2006.

[82]  J. Capmany and D. Novak, "Microwave photonics combines two worlds," *Nature Photonics,* vol. 1, pp. 319-330, 2007.

[83]  C. Wang  and J. Yao "Photonic Generation of Chirped Millimeter-Wave Pulses Based on Nonlinear Frequency-to-Time Mapping in a Nonlinearly Chirped Fiber Bragg Grating," *IEEE Transactions on Microwave Theory and Techniques,* vol. 56, pp. 542-553, 2008.

[84]  M. H. Khan, H. Shen, Y. Xuan, L. Zhao, S. Xiao, D. E. Leaird*, et al.*, "Ultrabroad-bandwidth arbitrary radiofrequency waveform generation with a silicon photonic chip-based spectral shaper," *Nat Photon,* vol. 4, pp. 117-122, 2010.

[85]  Q. Wang and J. Yao, "Switchable optical UWB monocycle anddoublet generation using a reconfigurablephotonic microwave delay-line filter," *Opt. Express,* vol. 15, pp. 14667-14672, 2007.

[86]  F. Zeng and J. Yao, "Ultrawideband impulse radio signal generation using a high-speed electrooptic phase modulator and a fiber-bragg-grating-based frequency discriminator," *IEEE Photonics Technology Letters,* vol. 18, pp. 2062-2064, 2006.

[87]     J. D. McKinney and A. M. Weiner, "Compensation of the effects of antenna dispersion on UWB waveforms via optical pulse-shaping techniques," *IEEE Transactions on Microwave Theory and Techniques,* vol. 54, pp. 1681-1686, 2006.

[88]     A. Dezfooliyan and A. M. Weiner, "Photonic synthesis of high fidelity microwave arbitrary waveforms using near field frequency to time mapping," *Submitted,* 2013.

[89]     I. H. Naqvi, P. Besnier, and G. E. Zein, "Robustness of a time-reversal ultra-wideband system in non-stationary channel environments," *IET Microwaves, Antennas & Propagation,* vol. 5, pp. 468-475, 2011.

[90]     A. M. Weiner, "Femtosecond pulse shaping using spatial light modulators," *Review of Scientific Instruments,* vol. 71, pp. 1929-1960, 2000.

[91]     J. Azana and M. A. Muriel, "Real-time optical spectrum analysis based on the time-space duality in chirped fiber gratings," *IEEE Journal of Quantum Electronics,* vol. 36, pp. 517-526, 2000.

[92]     V. Torres-Company, D. E. Leaird, and A. M. Weiner, "Dispersion requirements in coherent frequency-to-time mapping," *Optics Express,* vol. 19, pp. 24718-24729, 2011.

[93]     C. Wang and J. Yao, "Chirped microwave pulse generation based on optical spectral shaping and wavelength-to-time mapping using a sagnac loop mirror incorporating a chirped fiber bragg grating," *Journal of Lightwave Technology,* vol. 27, pp. 3336-3341, 2009.

[94]     B. H. Kolner, "Space-time duality and the theory of temporal imaging," *IEEE Journal of Quantum Electronics,* vol. 30, pp. 1951-1963, 1994.

[95]     M. T. Kauffman, A. A. Godil, B. A. Auld, W. C. Banyai, and D. M. Bloom, "Applications of time lens optical-systems," *Electronics Letters,* vol. 29, pp. 268-269, 1993.

[96]     A. M. Weiner, D. E. Leaird, J. S. Patel, and J. R. Wullert, "Programmable shaping of femtosecond optical pulses by use of 128-element liquid-crystal phase modulator," *IEEE Journal of Quantum Electronics,* vol. 28, pp. 908-920, 1992.

[97]     J. T. Willits, A. M. Weiner, and S. T. Cundiff, "Line-by-line pulse shaping with spectral resolution below 890 MHz," *Optics Express,* vol. 20, pp. 3110-3117, 2012.

[98]     S. Xiao and A. M. Weiner, "Coherent photonic processing of microwave signals using spatial light modulators: programmable amplitude filters," *Journal of Lightwave Technology,* vol. 24, pp. 2523-2529, 2006.

[99]     A. J. Metcalf, V. Torres-Company, V. R. Supradeepa, D. E. Leaird, and A. M. Weiner, "Fully programmable ultra-complex 2-D pulse shaping," *Conference of Lasers and Electro-Optics (CLEO),* 2012.

[100]   A. Derode, A. Tourin, and M. Fink, "Ultrasonic pulse compression with one-bit time reversal through multiple scattering," *Journal of Applied Physics,* vol. 85, pp. 6343-6352, 1999.

[101]   H. T. Nguyen, "Partial one bit time reversal for UWB impulse radio multi-user communications," in *2$^{nd}$ International Conference on Communications and Electronics ICCE*, pp. 246-251, 2008.

[102]  D. Abbasi-Moghadam and V. T. Vakili, "A SIMO one-bit time reversal for UWB communication systems," *EURASIP Journal on Wireless Communications and Networking,* p. 9, 2012.

[103]  Y. H. Chang, S. H. Tsai, X. Yu, and C. C. J. Kuo, "Ultrawideband transceiver design using channel phase precoding," *IEEE Transactions on Signal Processing,* vol. 55, pp. 3807-3822, 2007.

[104]  Y. H. Chang, S. H. Tsai, X. Yu, and C. C. J. Kuo, "Design and analysis of channel-phase-precoded ultra wideband (CPPUWB) systems," in *IEEE Wireless Communications and Networking Conference*, pp. 866-871, 2006.

[105]  H. T. Nguyen, "On the performance of one bit time reversal for multi-user wireless communications," in *4th International Symposium on Wireless Communication Systems ISWCS*, pp. 672-676, 2007.

[106]  S. H. Chang and R. A. Scholtz, "Polarization measurements in a UWB multipath channel," in *IEEE Military Communications Conference* , Vol. 1, pp. 192-196, 2004.

APPENDICES

# A. THEORETICAL COMPARISON OF THE PEAK TO AVERAGE POWER RATIO FOR PC VERSUS TR

In this appendix, we show that the temporal peak to average power ratio (PAPR) for PC always exceeds that for TR (equality only happens when we have a phase-only channel for which PC and TR become formally identical). We assume the system impulse response, $h_{Sys}(t)$, is assumed to be confined to a time aperture of $T$. We define the peak to average energy ratio $(\eta)$ parameter as follow:

$$\eta_{TR/PC} = \frac{\left|Max\{y_{TR/PC}(t)\}\right|^2}{\frac{1}{2T}\int\limits_{-T}^{T}\left|y_{TR/PC}(\tau)\right|^2 d\tau} \tag{A1}$$

Note that the received responses from TR and PC are limited to *2T* which is twice the aperture of the system response (due to the involved convolution operation). Based on the Parseval's theorem and equation (3.2) and (4.2), we have:

$$\frac{1}{2T}\int\limits_{-T}^{T}\left|y_{TR}(\tau)\right|^2 d\tau \overset{Parseval}{=} \frac{1}{2T}\int\limits_{-\infty}^{\infty}\left|Y_{TR}(f)\right|^2 df \overset{(3.2)}{=} \frac{1}{2T}\int\limits_{-\infty}^{\infty}\left|H_{Sys}(f)\right|^4 df \tag{A2}$$

$$\frac{1}{2T}\int\limits_{-T}^{T}\left|y_{PC}(\tau)\right|^2 d\tau \overset{Parseval}{=} \frac{1}{2T}\int\limits_{-\infty}^{\infty}\left|Y_{PC}(f)\right|^2 df \overset{(4.2)}{=} \frac{1}{2T}\int\limits_{-\infty}^{\infty}\left|H_{Sys}(f)\right|^2 df \tag{A3}$$

Considering the fact that the received responses from TR and PC have non-negative real frequency transfer functions (as defined in equations (3.2) and (4.2)), the peaks of the received responses happen at zero time delay where all the frequency components add up coherently to each other. Mathematically:

$$\left|y_{TR}(t)\right|^2 = \left|\int_{-\infty}^{\infty} Y_{TR}(f)e^{j2\pi ft}df\right|^2 \overset{(3.2)}{=} \left|\int_{-\infty}^{\infty}\left|H_{sys}(f)\right|^2 e^{j2\pi ft}df\right|^2 \le \left|\int_{-\infty}^{\infty}\left|H_{sys}(f)\right|^2\left|e^{j2\pi ft}\right|df\right|^2 \tag{A4}$$

$$\xrightarrow{\left|\exp(j2\pi ft)\right|\le 1}\left|Max\{y_{TR}(t)\}\right|^2 = \left|y_{TR}(0)\right|^2 = \left|\int_{-\infty}^{\infty}\left|H_{Sys}(f)\right|^2 df\right|^2$$

$$\left|y_{PC}(t)\right|^2 = \left|\int_{-\infty}^{\infty} Y_{PC}(f)e^{j2\pi ft}df\right|^2 \overset{(4.2)}{=} \left|\int_{-\infty}^{\infty}\left|H_{sys}(f)\right|e^{j2\pi ft}df\right|^2 \le \left|\int_{-\infty}^{\infty}\left|H_{sys}(f)\right|\left|e^{j2\pi ft}\right|df\right|^2 \tag{A5}$$

$$\xrightarrow{\left|\exp(j2\pi ft)\right|\le 1}\left|Max\{y_{PC}(t)\}\right|^2 = \left|y_{PC}(0)\right|^2 = \left|\int_{-\infty}^{\infty}\left|H_{Sys}(f)\right|df\right|^2$$

Using equations (A2)-(A5), we have the following expressions for the peak to average power ratios of TR and PC:

$$\eta_{TR} = \frac{\left|\int_{-\infty}^{\infty}\left|H_{Sys}(f)\right|^2 df\right|^2}{\dfrac{1}{2T}\int_{-\infty}^{\infty}\left|H_{Sys}(f)\right|^4 df} \tag{A6}$$

$$\eta_{PC} = \frac{\left|\int_{-\infty}^{\infty}\left|H_{Sys}(f)\right|df\right|^2}{\dfrac{1}{2T}\int_{-\infty}^{\infty}\left|H_{Sys}(f)\right|^2 df} \tag{A7}$$

As a result, to show the PAPR of PC always exceeds that of TR we should prove the following inequality holds:

$$\eta_{TR} \le \eta_{PC} \Leftrightarrow \left|\int_{-\infty}^{\infty}\left|H_{Sys}(f)\right|^2 df\right|^3 \le \left|\int_{-\infty}^{\infty}\left|H_{Sys}(f)\right|df\right|^2\left|\int_{-\infty}^{\infty}\left|H_{Sys}(f)\right|^4 df\right| \tag{A8}$$

To do this, we use the following theorem which is known as Holder's Inequality:

*Theorem (Holder's Inequality): Let f(x), g(x) X→R be two measurable*

*functions, and let $p,q \in (0,1)$ so that $p+q=1$.*

*Then:*

$$\left| \int_X f(x).g(x)\,dx \right| \le \left( \int_X |f(x)|^{1/p}\,dx \right)^p \left( \int_X |g(x)|^{1/q}\,dx \right)^q$$

*An equality holds if and only if $|f(x)|^{1/p}$ and $|g(x)|^{1/q}$ are linearly dependent.*

To use Holder's Inequality, we write equation (A8) as follow:

$$\left| \int_{-\infty}^{\infty} |H_{Sys}(f)|^2\,df \right| \le \left| \int_{-\infty}^{\infty} |H_{Sys}(f)|\,df \right|^{2/3} \left| \int_{-\infty}^{\infty} |H_{Sys}(f)|^4\,df \right|^{1/3}$$

$$\Leftrightarrow \left| \int_{-\infty}^{\infty} |H_{Sys}(f)|^2\,df \right| \le \left| \int_{-\infty}^{\infty} \left| |H_{Sys}(f)|^{2/3} \right|^{3/2}\,df \right|^{2/3} \left| \int_{-\infty}^{\infty} \left| |H_{Sys}(f)|^{4/3} \right|^3\,df \right|^{1/3}$$

(A9)

Equation (A9) is exactly Holder's Inequality in which $p=2/3$, $q=1/3$, $f=|H|^{2/3}$ and $g=|H|^{4/3}$. In this case, $f$ and $g$ become linearly dependent (or the equality holds) only when we have a phase-only channel for which PC and TR become formally identical. As a result, equation (A9) is always correct and the temporal peak to average power ratio (PAPR) for PC always exceeds that for TR.

# B. ANALOGY BETWEEN OUTPUT INTENSITY PROFILE OF FTM AND POWER SPECTRUM OF NF-FTM

Simulations and experiments presented in Figs. 6.3 and 6.5, respectively, showed that output intensity profiles obtained after dispersive propagation under conventional FTM were equal to scaled versions of optical power spectra shaped as prescribed under NF-FTM. Here we show that this scaling relationship always applies when $A_{FTM}(\omega)$, the Fourier transform of $a_{FTM}(t)$, is real.

We start with the power spectrum of the NF-FTM technique:

$$\left|A_{NF-FTM}(\omega)\right|^2 \propto \left|\int_{-\infty}^{+\infty} a_{NF-FTM}(t')\exp(-j\omega t')dt'\right|^2 \tag{B.1}$$

$$\overset{equation\ (6.7)}{=} \left|\int_{-\infty}^{+\infty} a_{FTM}(t')\exp\left(j\frac{t'^2}{2\psi_2}\right)\exp(-j\omega t')dt'\right|^2 \tag{B.2}$$

$$= \left|\left[\int_{-\infty}^{+\infty} a_{FTM}(t')\exp\left(j\frac{t'^2}{2\psi_2}\right)\exp(-j\omega t')dt'\right]^*\right|^2 \tag{B.3}$$

$$\overset{t'\to-t'}{=} \left|\int_{-\infty}^{+\infty} a_{FTM}^*(-t')\exp\left(-j\frac{t'^2}{2\psi_2}\right)\exp(-j\omega t')dt'\right|^2 \tag{B.4}$$

$$\overset{a_{FTM}^*(-t')=a_{FTM}(t')}{=} \left|\int_{-\infty}^{+\infty} a_{FTM}(t')\exp\left(-j\frac{t'^2}{2\psi_2}\right)\exp(-j\omega t')dt'\right|^2 \tag{B.5}$$

where the relation $a_{FTM}^*(-t) = a_{FTM}(t)$ holds based on the assumption that $a_{FTM}(t)$ has a real Fourier transform.

On the other hand, according to equation (6.1), the output intensity profile of the conventional FTM technique after dispersive propagation can be expressed as:

$$\left| a_{out}\left(t\right) \right|^2 \propto \left| \int_{-\infty}^{+\infty} a_{FTM}\left(t'\right) \exp\left(-j\frac{t'^2}{2\psi_2}\right) \exp\left(j\frac{tt'}{\psi_2}\right) dt' \right|^2 \qquad (B.6)$$

Equations (B.5) and (B.6) are scaled replicas of each other if we make the identification $\omega = -t/\psi_2$.

VITA

VITA

Amir Dezfooliyan received his B. Sc. degree in Electrical Engineering from Sharif University of Technology, Tehran, Iran in 2009. Amir is currently a Ph.D. candidate in the School of Electrical and Computer Engineering at Purdue University, West Lafayette, IN, USA. Since 2009, he has been a Graduate Research Assistant with the Ultrafast Optics and Optical Fiber Communications Laboratory at Purdue University. His research interests include Optical-Wireless Communications, Radio Frequency Propagation Measurement, Multipath Interference Management, Microwave Photonics and Ultrafast Optics.

During the course of his graduate study, Amir has authored/co-authored over 15 publications in peer reviewed journals and international conferences. He received the Honorable Mention award of the 2011 IEEE International Symposium on Antennas and Propagation. Amir has served as a reviewer for IEEE Transactions on Antennas and Propagation, IEEE Transactions on Wireless Communications, IET Communications, International Journal of Electronics, and Journal of Electromagnetic Waves and Applications.